

Investigation of Fibre Bragg Grating Sensing Technology based Thermal Monitoring of IGBT Power Module

A thesis submitted to The University of Manchester for the degree of

Doctor of Philosophy

in the Faculty of Science and Engineering

2023

Shiying Chen

Department of Electrical and Electronic Engineering

Power and Energy Division

Blank page

Table of Contents

Table of Contents	3
List of Figures	6
List of Tables	11
Nomenclature	13
Abstract	15
Declaration	16
Copyright Statement	17
Acknowledgements	18
Chapter 1 : Introduction	19
1.1 Introduction	19
1.2 Thermal issues of IGBT power modules	21
1.3 Junction temperature acquisition issues	22
1.4 Problem statement	25
1.5 Aims and objectives	27
1.6 Contribution of the research	27
1.7 Structure of the thesis	28
1.8 List of publications	30
Chapter 2 : Literature Review	32
2.1 IGBT power modules package structure and failure mechanism	32
2.1.1 IGBT power module package structure	32
2.1.2 Wire-bond IGBT power modules package-related ageing mechanism.	33
2.2 Junction temperature acquisition technologies	35
2.2.1 Method based on TSEPs	36
2.2.2 Method based on the thermal circuits and FEA models	37
2.2.3 Optical methods and sensor-based technologies	41
2.3 FBG sensors' structure, mechanism, and applications in power electronic devices	43
2.3.1 The structure of FBG sensors	43
2.3.2 Interrogation methods of FBG sensors	44
2.3.3 The principle of the FBG sensor	45
2.3.4 The application of the FBG sensors in power electronics	46
2.4 Summary	47

Chapter 3 : Simulation Model	49
3.1 The structure and dimensions of the IGBT power module.....	49
3.2 Literature review based determination of material properties	52
3.3 Thermal circuit based modification of material properties.....	55
3.4 Simplification of IGBT FEA model and the mesh detail	61
3.5 Electro-thermal performance simulation	63
3.5.1 Electrical boundary setting	63
3.5.2 Thermal boundary setting and simulation results	64
3.6 Summary.....	67
Chapter 4 : Test Rig.....	69
4.1 FBG thermal sensing system	69
4.1.1 FBG temperature sensor design and packaging.....	69
4.1.2 Interrogation	70
4.1.3 SmartSoft.....	72
4.2 FBG sensor thermal calibration test-rig.....	75
4.3 Main test rig and components.....	76
4.4 $V_{CE} - T_j - I_C$ calibration test rig.....	80
4.5 Summary.....	82
Chapter 5 : FBG Sensor Installation and Interfacing Technologies	83
5.1 Test interface materials and their properties.....	83
5.2 Calibration of the Free FBG Sensors.....	85
5.3 FBG Sensor Installation.....	87
5.4 Simulation of interface thermal conductivity effect on sensing performance	89
5.4.1 Transient response	91
5.4.2 Stationary response.....	92
5.5 Influence from the interface materials on the sensors	95
5.5.1 ‘Air-interface’ case and ‘paste-interface’ case	95
5.5.2 Glue 8329TCM based ‘Glue-interface’ case	96
5.5.3 Glue ES578 based ‘Glue-interface’ case	98
5.5.4 Glue TCOR75S based ‘Glue-interface’ case.....	101
5.5.4 Summary of glue-induced effects	102
5.6 Temperature measurement analysis of ‘Air-interface’ case and ‘paste-interface’ case.....	103

5.7 Summary	109
Chapter 6 : FBG Head Size Influence on Localized On-chip Thermal Measurement in IGBT Power Modules	111
6.1 FEA thermal analysis	111
6.2 Test IGBT surface temperature distribution characterisation	113
6.3 Different head size FBG sensor performance analysis - experimental study	115
6.3.1 IGBT-FBG cases at location 1	115
6.3.2 Location 1 thermal excitation profiles and test results.....	116
6.3.3 IGBT-FBG cases at location 2	119
6.3.4 Location 2 thermal excitation profiles and test results.....	120
6.4 Experimental results discussion	122
6.5 FBG reflected spectrum distortion	123
6.6 Summary	125
Chapter 7 : Comparison of V_{CE} and FBG based Junction Temperature Acquisition Technologies	126
7.1 $V_{CE} - T_j - I_C$ and $\Delta V_{CE} - T_j - I_C$ relationships calibration	126
7.1.1 Simulation of temperature rise caused by current impulses.....	126
7.1.2 $V_{CE} - T_j - I_C$ calibration test.....	128
7.1.3 $V_{CE} - T_j - I_C$ relationship	130
7.1.4 $\Delta V_{CE} - T_j - I_C$ relationship.....	132
7.2 Comparison of junction temperatures acquired based on V_{CE} , FBG sensor, and thermal camera.....	133
7.2.1 Test rig	133
7.2.2 Junction temperature measured by the FBG sensor and thermal camera.....	134
7.2.3 $V_{CE}-T_j-I_C$ relationship based junction temperature evaluation.....	136
7.2.4 $\Delta V_{CE}-T_j-I_C$ relationship based junction temperature evaluation	137
7.3 Summary	138
Chapter 8 : Conclusion and Future Work	140
8.1 Conclusion	140
8.2 Future work.....	141
References.....	144
Appendix A. MSP430 PWM Signal Program	153

List of Figures

Fig. 2.1. IGBT package structure [7]. (a) Wire-bond modules; (b) Press-pack modules. .	32
Fig. 2.2. Typical crack propagation process in bonding line [13].	35
Fig. 2.3. Fibre Bragg grating sensor structure.	43
Fig. 2.4. The circuit schematic of the test rig (redrawn from [110])	46
Fig. 3.1. Bare Semikron SKM50GB12T4 IGBT module used in this study	49
Fig. 3.2. The layered structure of the IGBT power module.....	49
Fig. 3.3. The cutting section picture of the IGBT power module	51
Fig. 3.4. The front section picture of the IGBT power module.	51
Fig. 3.5. The conduction of the heat between two layers	56
Fig. 3.6. The initial Cauer thermal circuit.....	57
Fig. 3.7. The transient thermal impedance.....	57
Fig. 3.8. The improved transient thermal impedance	59
Fig. 3.9. Final transient thermal impedance.....	59
Fig. 3.10. The final Cauer thermal circuit.....	60
Fig. 3.11. The FEA model of IGBT power module. (a) Detail structure of the chip and the bond wires. (b) Detail structure of the ceramic layer and the copper layers. (c) Detail structure of the baseplate and the heat sink	62
Fig. 3.12. The IGBT FEA model geometry. (a) The FEA model without heat sink. (b) The IGBT half module.	63
Fig. 3.13. The mesh detail of the IGBT half model.....	63
Fig. 3.14. The thermal distribution of the full FEA model with a heat sink model.....	66
Fig. 3.15. The thermal distribution of the full FEA model without heat sink.....	66
Fig. 3.16. The thermal distribution of the half FEA model.....	67
Fig. 3.17. The thermal distribution of the IGBT chip.....	67
Fig. 4.1. Typical structure of the FBG sensor	69
Fig. 4.2. Sketch of a single FBG probe.....	70
Fig. 4.3. Photograph of FBG packaged temperature sensor [125]	70
Fig. 4.4. System diagram of FBG sensor interrogation. (a) Photography of the SmartScan interrogator. (b) SmartScan interrogator system diagram.....	71

Fig. 4.5. SmartSoft instrumentation window interface	73
Fig. 4.6. Enhanced acquisition – Sensors’ tab.....	74
Fig. 4.7. The thermal chamber	75
Fig. 4.8. Test rig. (a) electric circuit diagram, (b) Test rig top view.....	77
Fig. 4.9. Control timing diagram of the two IGBTs.....	77
Fig. 4.10. The DC power source.	78
Fig. 4.11. Forced air cooling heatsink.	78
Fig. 4.12. Driver board circuit.....	78
Fig. 4.13. Driver board PCB	79
Fig. 4.14. Circuit diagram of the $V_{CE} - T_j - I_C$ relationship calibration test rig	81
Fig. 4.15. Control timing diagram of the three IGBTs.....	81
Fig. 5.1. Schematic representation of the used FBG sensors.	85
Fig. 5.2. Wavelength-temperature characteristic for the free FBG sensor. with an inset showing the typical deviation of the measured wavelength λ_B of the four thermal cycles at 120 °C.	86
Fig. 5.3. The IGBT chip and the bond wires.....	87
Fig. 5.4. Schematic representation of the installed FBG for the three interface options assessed: (a) ‘air-interface’, (b) ‘paste-interface’, (c) ‘glue-interface’.	89
Fig. 5.5. Instrumented IGBT module FE model geometry. (a) Top view. (b) Cross-section view.	90
Fig. 5.6. FBG average sensing head temperature, transient response to a 50A, 0.5s pulse for a 75 μ m gap.....	91
Fig. 5.7. FBG average sensing head temperature, transient response to a 50A, 0.5s pulse for a 5 μ m gap.....	92
Fig. 5.8. FBG average sensing head temperature for a 75 μ m gap, 50A at 1Hz (top), 10Hz (middle) and 100Hz (bottom) switching frequencies.....	93
Fig. 5.9. FBG average sensing head temperature for different interface gaps at 100Hz, 50A.	94
Fig. 5.10. Gapless FBG average sensing head temperature for different thermal interface thermal conductivities at 100Hz, 50A.....	94

Fig. 5.11. The calibration results of FBG sensor 1 before and after the installation. (a) The 8 iterations of calibration results across the whole temperature range. (b) Detailed calibration results at 120°C.....	96
Fig. 5.12. The average and standard deviation of the second to the seventh calibration results of FBG sensor 1. (a) The average calibration curve. (b) The standard deviation of the average calibration curve.	97
Fig. 5.13. The changes in the calibration results compared with the free FBG sensor.....	97
Fig. 5.14. The calibration results of FBG sensor 2 before and after the installation	99
Fig. 5.15. The average and standard deviation of the first to the fourth calibration results of FBG sensor 3	99
Fig. 5.16. The calibration results of FBG sensor 3 with temperature higher than the T_g 100	
Fig. 5.17. Calibration results of FBG 5 sensor for rated temperature range.....	101
Fig. 5.18. Measurement of the ‘air-interface’ FBG sensor and the reference thermal image at 1 kHz. (a) The temperature measured by the ‘air-interface’ FBG sensor. (b) The thermal image taken by the thermal camera.	104
Fig. 5.19. Measurement of the ‘solid-interface’ FBG sensor and the reference thermal image at 1 kHz. (a) The temperature measured by the ‘solid-interface’ FBG sensor. (b)The thermal image taken by the thermal camera.	105
Fig. 5.20. Temperature measured by the ‘air-interface’ case and the ‘solid-interface’ case at 100 Hz.....	106
Fig. 5.21. Temperature measured by the ‘air-interface’ case and the ‘solid-interface’ case at 10 Hz.....	106
Fig. 5.22. Temperature measured by the ‘air-interface’ case and the ‘solid-interface’ case at 1 Hz.....	106
Fig. 5.23. Step responses for the ‘air-interface’ and ‘solid-interface’ FBG installations.	109
Fig. 6.1. The power module FEA model and IGBT mesh detail	112
Fig. 6.2. FEA simulated thermal distribution of the IGBT chip. (a) IGBT chip with bond wires. (b) IGBT chip without bond wires.	112
Fig. 6.3. FEA simulated temperature distribution along: (a) Line 1. (b) Line 2 in Fig. 6.2(b)	113

Fig. 6.4. IGBT surface thermal image at 50 A DC current	114
Fig. 6.5. Surface temperature distribution along line 1 (Fig. 6.2b) for thermal camera measurement.	114
Fig. 6.6. FBG positions for location 1. (a) 1 mm FBG sensor, (b) 3 mm FBG sensor, (c) 5 mm FBG sensor.....	116
Fig. 6.7. FEA simulated thermal excitation profile at location 1 for: (a) 1 mm FBG sensor, (b) 3 mm FBG sensor, (c) 5 mm FBG sensor.....	117
Fig. 6.8. Measurements of location 1 at 1 kHz switching frequency.....	118
Fig. 6.9. Measurements of location 1 at 100 Hz switching frequency.....	118
Fig. 6.10. Measurements of location 1 at 10 Hz switching frequency.....	119
Fig. 6.11. The 3 mm IGBT-FBG case for location 2. (a) 1 mm FBG sensor, (b) 3 mm FBG sensor, (c) 5 mm FBG sensor.	119
Fig. 6.12. FEA simulated FBG sensors thermal excitation profiles at location 2 for: (a) 1 mm FBG sensor. (b) 3 mm FBG sensor. (c) 5 mm FBG sensor.....	120
Fig. 6.13. Measurements of location 2 at 1 kHz switching frequency.....	120
Fig. 6.14. Measurements of location 2 at 100 Hz switching frequency.....	121
Fig. 6.15. Measurements of location 2 at 10 Hz switching frequency.....	121
Fig. 6.16. Measured spectra of the 1 mm FBG sensor.....	124
Fig. 6.17. Measured spectra of the 3 mm FBG sensor.....	124
Fig. 6.18. Measured spectra of the 5 mm FBG sensor.....	125
Fig. 7.1. The mesh detail of the IGBT half model	127
Fig. 7.2. Thermal response of the IGBT chip in 1 ms.....	128
Fig. 7.3. Circuit diagram of the $V_{CE} - T_j - I_C$ relationship calibration test rig	128
Fig. 7.4. An example of recorded $V_{CE, DUT}$ and I_{DUT} under a certain condition	129
Fig. 7.5. Exponential curve fitting of the I_{DUT}	129
Fig. 7.6. 3-D $V_{CE} - T_j - I_C$ relationship under 15 V $V_{G, DUT}$	130
Fig. 7.7. $V_{CE} - T_j - I_C$ relationship curves under 15 V $V_{G, DUT}$	131
Fig. 7.8. $V_{CE} - I_C$ relationship curves in large current ranges	131
Fig. 7.9. $V_{CE} - T_j$ relationship curves in large current ranges	131
Fig. 7.10. $\Delta V_{CE1218} - T_j$ relationship curves in large current ranges	133

Fig. 7.11. Test rig electric circuit diagram.	133
Fig. 7.12. Thermal image of the IGBT chip	135

List of Tables

Table 2.1. CTE of different materials. [7]	34
Table 2.2. Typical response times and temperature ranges of the sensors	42
Table 3.1. The name and general material of each layer [5]	50
Table 3.2. The directly measurable dimensions of each layer	51
Table 3.3. The dimensions of the model	52
Table 3.4. Reports on Thermal Conductivities [111][112].....	53
Table 3.5. Reports on Thermal Parameters [113].....	53
Table 3.6. Reports on Thermal Parameters [114].....	53
Table 3.7. Reports on Thermal Conductivities [115]	53
Table 3.8. The thermal parameters reported in [116]	54
Table 3.9. The thermal parameters reported in [116]	54
Table 3.10. Constant thermal parameters [120]	54
Table 3.11. Non-constant thermal parameters [120]	55
Table 3.12. Key values for the thermal parameters.....	55
Table 3.13. Initial thermal parameters of the materials.....	55
Table 3.14. The thermal parameters of each layer	57
Table 3.15. Thermal parameters of each layer	59
Table 3.16. Thermal parameters of the materials	60
Table 3.17. Dimensions of the model.....	60
Table 3.18. Thermal parameters of the materials	64
Table 4.1. Dimensions and properties of the FBG sensor.....	70
Table 4.2 SmartScan interrogator specifications [107]	71
Table 4.3. SmartScan multiple scan rate [107]	73
Table 4.4. Key Specification of the Equipment used for Experiments.	80
Table 5.1. Interfacing materials and their properties.....	84
Table 5.2. Dimensions and properties of Teflon capillary	88
Table 5.3. Temperature measurements for the two FBG cases at 50A	108
Table 5.4. Temperature measurements for the two FBG cases at 30A.	108

Table 6.1. Measurements at location 1, 1 kHz, 100 Hz and 10 Hz (°C)	118
Table 6.2. $T_j - T_a$ at location 1, 1 kHz, 100 Hz and 10Hz (°C)	118
Table 6.3. Measurements at location 2, 1 kHz, 100 Hz and 10 Hz (°C)	121
Table 6.4. $T_j - T_a$ at location 2, 1 kHz, 100 Hz and 10 Hz (°C)	121
Table 7.1. FBG Sensor and Camera Measured I_C and T_j	135
Table 7.2. Measured V_{CE} , I_C , and V_{CE} based Calculated T_j	136
Table 7.3. ΔV_{CE} based Calculated T_j	137

Nomenclature

List of Acronyms

FBG	Fibre Bragg grating
IGBT	Insulated gate bipolar transistors
FEA	Finite element analysis
CTE	Coefficient of thermal expansion
TSEP	Temperature sensitive electrical parameter
EMI	Electromagnetically immune
SOA	Safe operating area
IR	Infrared
CFD	Computational fluid dynamics
RC	Resistor-capacitor
PWM	Pulse-Width Modulation
MOR	Model Order Reduction
RTDs	Resistance temperature detectors
SMF	Single-mode optical fibre
WDM	Wavelength-division multiplexing
SPWM	Sinusoidal pulse width modulation
TBD	To be determined
RMS	Root mean square
DUT	Device under test
SD	Standard deviation

List of Symbols

<i>Symbol</i>	<i>Definition</i>	<i>S.I. Units</i>
V_{CE}	On-state voltage drop	V
$V_{CE (low)}$	On-state voltage at low current	V
$V_{CE (high)}$	On-state voltage at high current	V
$V_{CE(sat)}$	Saturated on-state voltage	V
I_{SC}	Short-circuit current	A
t_{doff}	Turn off delay time	s

R	Resistance	Ω
C	Capacitance	F
V_{GE}	Gate-emitter voltage	V
T_j	Junction temperature	$^{\circ}\text{C}$
I_C	Collector current	A
Λ	Grating period	g/mm
ε	Strain	mm/mm
$\Delta\varepsilon$	Strain change	mm/mm
T	Temperature	$^{\circ}\text{C}$
ΔT	Temperature change	$^{\circ}\text{C}$
λ	Thermal conductivity / Wavelength	$\text{W}/\text{m}\cdot\text{K}$ / m
$\Delta\lambda$	Change of central wavelength	m
P_{eff}	Photo-elastic parameter	B
α	Thermal expansion coefficient	K^{-1}
ξ	Thermal-optic coefficient of fibre core	$^{\circ}\text{C}^{-1}$
$R_{th,TIM}$	Thermal resistance	$^{\circ}\text{C}/\text{W}$
c_p	Heat capacity	J/K
ρ	Density	kg/m^3
σ_{Si}	Electrical conductivity	S/m
d_{IGBT}	IGBT chip thickness	m
A_{IGBT}	IGBT chip top surface area	m^2
h	Heat transfer coefficient	$\text{W}/(\text{m}^2\cdot\text{K})$
$V_{CE,DUT}$	Collector-to-emitter voltage of the IGBT_DUT	V
I_{DUT}	Collector current of the IGBT_DUT	A
T_g	Glass transition temperature	$^{\circ}\text{C}$
T_a	Ambient temperature	$^{\circ}\text{C}$
τ	Time constant	s

Abstract

This thesis explores the use of Fibre Bragg Grating (FBG) sensors for direct on-chip thermal sensing of Insulated Gate Bipolar Transistors (IGBTs). The research focuses on three main aspects: (1) investigating FBG sensor bonding technologies on IGBT chip surfaces and the impact of various interface materials on thermal measurement performance, (2) analyzing the influence of FBG head length on IGBT thermal sensing accuracy, and (3) evaluating FBG sensor performance for in-situ IGBT junction temperature sensing compared to voltage-based methods.

A Finite Element Analysis (FEA) model of the IGBT power module was developed to understand thermal distribution on the chip and assess FBG sensor performance. Various FBG sensor bonding techniques were explored, with the FEA model used to study thermal conductivity of interface materials. Performance of glue-bonded FBG sensors during thermal expansion and contraction was examined, revealing potential strain due to coefficient of thermal expansion (CTE) mismatches and adhesive forces. Effective sensing performance was achieved by operating FBG sensors within the glue's linear working range.

Additionally, the impact of FBG head length on direct on-chip thermal sensing of IGBTs was investigated through thermal simulations and experimental characterizations. Challenges arising from significant thermal gradients in IGBT applications with longer head lengths were identified. Analysis of reflected spectrum distortion of FBG sensors provided insights into the limitation of accurately measuring IGBT junction temperature.

Comparisons were made between FBG-based contact temperature measurement and voltage-based approaches, assessing strengths, limitations, and potential errors associated with each method.

Overall, this research provides valuable insights into the application of FBG sensors for direct thermal sensing of IGBTs. The findings contribute to the understanding of the thermal behaviour of IGBT power modules and offer guidance on optimizing FBG sensor performance in terms of bonding techniques, head length selection, and accurate junction temperature measurement. The study confirms the suitability of FBG sensors for in-situ sensing of IGBT junction temperature, enabling reliable and effective thermal monitoring in various operational conditions.

Declaration

No portion of the work referred to in this thesis has been submitted in support of an application for another degree or qualification of this or any other university or other institute or learning.

Copyright Statement

- i. The author of this thesis (including any appendices and/or schedules to this thesis) owns any copyright in it (the “copyright”) and he has given The University of Manchester the right to use such Copyright for any administrative, promotional, educational and/or teaching purposes.
- ii.* Copies of this thesis, either in full or in extracts, may be made **only** in accordance with the regulations of the John Rylands University Library of Manchester. Details of these regulations may be obtained from the Librarian. This page must form part of any such copies made.
- iii.* The ownership of any patents, designs, trade marks and any and all other intellectual property rights except for the Copyright (the “Intellectual Property Rights”) and any reproductions of copyright works, for example graphs and tables (“Reproductions”), which may be described in this thesis, may not be owned by the author and may be owned by third parties. Such Intellectual Property Rights and Reproductions cannot and must not be made available for use without the prior written permission of the owner(s) of relevant Intellectual Property Rights and/or Reproductions.
- iv.* Further information on the conditions under which disclosure, publication and exploitation of this thesis, the Copyright and any Intellectual Property Rights and/or Reproductions described in it may take place is available from the Head of School or Electrical and Electronic Engineering (or the Vice-President) and the Dean of the Faculty of Life Sciences, for Faculty of Life Sciences’ candidates.

Acknowledgements

I stand at the culmination of a remarkable journey, one that has shaped me both professionally and personally. As I prepare to complete my PhD degree, I am filled with gratitude for all those who have been instrumental in making this achievement possible.

First and foremost, I express my deepest appreciation to my supervisors, Prof. Mike Barnes and Dr. Sinisa Durovic. Your unwavering support, guidance, and encouragement throughout these four years have been invaluable. Your expertise and mentorship have not only shaped the direction of my research but also inspired me to constantly push the boundaries of knowledge. I am truly fortunate to have had the opportunity to work under your mentorship.

I am also grateful to my colleagues, Damian Vilchis-rodriguez, Asep Suryandi, Yingzhao Wang, Youhong Chen, Shuai Wang, Arsim Ahmedi, Jack Andrews, Aras Ghafoor, and Christian Kukura, whose camaraderie and collaboration have made this journey all the more enriching. Your friendship and support have made the challenges more manageable and the victories more meaningful. I cherish the memories of our time together and will always remember the laughter and camaraderie that filled our lab.

I extend my heartfelt gratitude to my family and friends for their unwavering love and support. Your encouragement, understanding, and belief in my abilities have been a constant source of strength throughout this journey.

As I reflect on these past four years, I am filled with mixed emotions. The time has flown by so quickly, and yet the memories of the challenges overcome and the accomplishments achieved are etched in my heart. I also acknowledge that there have been moments of difficulty and setbacks, especially during the unprecedented times of the pandemic and the laboratory relocation. The impact of isolation on mental health took a toll on my research progress, resulting in delays and challenges. Despite these obstacles, I am grateful for the resilience and determination that enabled me to persevere and overcome these hurdles. This journey has been a rollercoaster of learning, growth, and self-discovery, and I am grateful for every moment of it.

Chapter 1: Introduction

1.1 Introduction

In response to the urgent need to address climate change and achieve Net Zero emissions, there is a global push towards sustainable energy solutions [1]. Renewable energy generation technologies, such as solar and wind power, have gained significant tendency in this transition [2]. To effectively integrate these energy sources into the power grid, efficient power electronics systems are essential. Advancements in power electronics devices, such as Insulated Gate Bipolar Transistor (IGBT), Metal-Oxide-Semiconductor Field-Effect Transistors (MOSFETs), Thyristors, Silicon Carbide (SiC) devices, and Gallium Nitride (GaN) devices, have revolutionized the power electronics landscape. Among these power electronic devices, IGBT power modules play a crucial role in current industry to enable the conversion, distribution, and management of renewable energy, ensuring its effective utilization and grid connectivity [3]. Additionally, as the transportation sector undergoes a shift towards electrification, IGBT power modules are instrumental in powering electric vehicles and facilitating efficient energy conversion between the battery and the motor, further contributing to the reduction of greenhouse gas emissions and the promotion of sustainable transportation solutions [2][4]. Overall, the increasing demand for clean energy and the electrification of various sectors underscore the significance of power electronics, specifically IGBT power modules, in driving the transition towards a low-carbon future [3].

The reliable operation of IGBT modules is crucial for ensuring the performance, efficiency, and longevity of these systems [5]. However, the thermal management of IGBT modules poses significant challenges due to the inherent power dissipation associated with their operation [6][7].

The accurate measurement of the junction temperature in IGBT power modules is of vital importance in understanding the thermal behaviour of these devices [8]. The junction temperature directly affects the performance, reliability, and lifespan of the IGBT modules [6][9]. Excessive temperature fluctuations can lead to accelerated aging, altered electrical characteristics, and impaired switching behaviour, ultimately resulting in reduced lifespan and potential catastrophic failures [5][9].

Currently, the available methods for on-line measurement of IGBT junction temperature have certain limitations, which hinder their effectiveness and applicability

[8][9]. Temperature sensitive electrical parameter (TSEP) based evaluation techniques provide quasi-average temperature estimations but fail to capture the spatial temperature distribution within the module [10][11]. Additionally, their accuracy can be affected by module ageing and the precision of calibration and electrical parameter measurement processes [12][13]. On the other hand, thermal circuit and Finite Element Analysis (FEA) models offer a detailed understanding of thermal behaviour but require accurate input parameters and may have uncertainties in material properties and boundary conditions [14] - [17].

To overcome these limitations, this thesis focuses on the development and application of fibre Bragg grating (FBG) sensors for accurate and real-time direct junction temperature measurement in IGBT power modules. FBG sensors, based on optical fibre technology and fully electromagnetically immune (EMI), have recently been shown to have potential to facilitate localized temperature measurements and valuable insights into the thermal behaviour of IGBTs, however direct on-chip sensing applications in IGBTs have not been assessed [18]-[21]. FBGs have been shown to work well in applications such as electrical machines, buildings, bridges, oil and gas pipelines, biomedical imaging, in-body monitoring, etc., to realize temperature or strain measurement.

The research firstly develops of an electro-thermal FEA model to understand the thermal distribution and behaviour within the module, facilitating the selection of optimal installation positions for FBG sensors. Furthermore, an experimental test-rig is constructed to explore the electro-thermal behaviour of IGBT power modules and evaluate the in-situ FBG thermal sensing system's performance in real operating conditions of IGBTs. The installation methods and interfacing technologies for FBG sensors on the IGBT chip surface are investigated to enhance temperature measurement accuracy and reliability. One important part is tests of different interface materials and their influences on the sensors' performance. Additionally, the sensor performance with different FBG head size is examined through thermal mapping simulations and experiment. The intense thermal gradient of the IGBT chip imposes high requirement on the selection of FBG sensor head length. An extensive comparison is made between FBG sensor-based junction temperature measurement and V_{CE} -based evaluation techniques, analyzing the advantages, limitations, and validating the effectiveness of FBG sensors through experimental studies.

The findings of this research contribute to advancing the field of junction temperature measurement in IGBT power modules. The research aims to optimize thermal management strategies, enhance the reliability and performance of IGBT modules, and ensure safe and

efficient operation in various industrial applications.

1.2 Thermal issues of IGBT power modules

Thermal issues in IGBT power modules arise from the significant power dissipation inherent in their operation [5]. During switching or conduction, the IGBT experiences power losses, resulting in the generation of heat. These losses primarily manifest as conduction losses through the on-state voltage drop (V_{CE}) and switching losses during the transition between on and off states [6][22]. The IGBT package and the external heat sink are designed to dissipate heat effectively, which prevents the chip temperature from exceeding the rated upper limit [23]. But the effective heat dissipation also leads to quick temperature drop during the IGBT off-state [23][24]. Thus, temperature fluctuations appear during IGBTs' switching. The external power change can also lead to temperature fluctuations, especially in the wind power generation and electric vehicles [3][9].

The accumulation of heat can lead to the formation of localized hotspots, temperature gradients, and thermal stress, ultimately impacting the overall performance and reliability of the IGBT module [25][26]. Excessive temperature fluctuations can accelerate aging and degradation of critical components within the module, especially the solder layers and bond wires joints, leading to a reduced lifespan and potential catastrophic failures [5][9]. Therefore, it is crucial to implement effective thermal management strategies to mitigate these thermal stresses and ensure long-term reliability of the IGBT power module [6].

In addition, temperature directly affects the electrical characteristics and performance of IGBTs. The on-state voltage drop and conduction losses are temperature-dependent, meaning that changes in junction temperature alter the device's electrical behaviour **Error! Reference source not found..** Elevated temperatures can increase the on-state voltage drop and conduction losses, negatively impacting the IGBT's efficiency and power dissipation capabilities [28]. It is crucial to accurately monitor and control the junction temperature to optimize the device's performance and ensure safe operation.

Moreover, the thermal behaviour of IGBTs significantly affects their switching characteristics [29]. As temperature rises, the carrier mobility and conductivity of the semiconductor materials change, leading to increased switching losses, reduced switching speed, and compromised reliability [30][31]. Understanding the thermal behaviour is vital for proper design, control, and optimization of IGBT-based power electronic systems.

Furthermore, the thermal performance of IGBTs directly affects their power handling capabilities and efficiency. Higher operating temperatures can limit the maximum current

rating of the device, reduce the safe operating area (SOA), and impose derating constraints [32]. Thermal issues can also affect the IGBT's dynamic behaviour, such as the ability to sustain high-frequency switching and handle short-circuit conditions [9][33]. Understanding the thermal limitations and optimizing the thermal design are crucial for achieving the desired power handling capacity and efficiency of IGBT power modules.

In conclusion, thermal issues in IGBT power modules have a profound impact on their performance, reliability, and efficiency. The accumulation of heat during operation leads to temperature non-uniformities, hotspots, altered electrical characteristics, and compromised switching behaviour. The temperature fluctuations can cause accelerated aging and degradation of critical components, reducing the module's lifespan and posing potential catastrophic failures. Effective on-line thermal measurement enables accurate characterization of device performance, which can help engineers understand thermal limitations and optimize operating parameters and cooling strategies for safe and efficient operation. Continuous on-line monitoring of junction temperature allows for prompt detection of abnormal temperature rises, which facilitates the implementation of circuit protective measures.

1.3 Junction temperature acquisition issues

Various junction temperature acquisition technologies have been developed to enable effective monitoring of IGBT temperatures, which are generally classified into three categories: TSEPs based junction temperature estimation, thermal circuits and FEA model based junction temperature estimation, and optical technologies based contact and non-contact measurement [9][34].

One of the widely used approaches for junction temperature evaluation in wire-bond IGBT power modules is based on TSEPs. This method leverages the inherent temperature dependencies exhibited by certain electrical characteristics of the IGBT module, such as on-state voltage at low current ($V_{CE (low)}$) [12], on-state voltage at high current ($V_{CE (high)}$) [35][36], short-circuit current (I_{SC}) [37][38], turn off delay time (t_{doff}) of the gate-emitter voltage (V_{GE}) [39]-[42].

To estimate the junction temperature using TSEPs, an accurate calibration process is necessary. This involves establishing a correlation between the measured electrical parameter and the corresponding junction temperature under various operating conditions. Calibration can be performed using a reference measurement technique, such as thermal sensors or thermal camera placed near the IGBT chip [35][43]. Once the calibration is

complete, the TESP can be monitored during normal operation, and the junction temperature can be estimated based on the established calibration curve or mathematical model.

The advantage of this approach is that it does not require additional sensing elements or modifications to the IGBT module, making it relatively straightforward to implement. However, it does have certain limitations. This approach provides an average temperature estimation rather than spatial temperature distribution within the module [10]. It assumes uniform temperature across the entire device, which may be inaccurate in scenarios where localized hotspots or thermal gradients exist [11]. Furthermore, changes in the electrical characteristics due to module ageing can affect the accuracy of the temperature estimation [13]. Additionally, the accuracy can be influenced by the quality and precision of the calibration process, the correlation with the temperature, and the measurement accuracy of the electrical parameters during operation.

Another approach for junction temperature evaluation in IGBT power modules is based on thermal circuit and FEA models. This method involves creating a thermal model of the IGBT module, which takes into account the heat generation, dissipation, and flow within the device. By simulating the thermal behaviour using computational techniques, the junction temperature can be estimated.

The thermal circuit model represents the thermal paths and resistances within the IGBT module [17][34]. It includes components such as thermal resistors, thermal capacitors, and heat sources that mimic the thermal behaviour of different parts of the device [44]. To create an accurate thermal circuit model, various factors need to be considered, such as module geometries, material properties, thermal interface characteristics, and thermal boundaries of the IGBT module. These parameters are often obtained from datasheets, manufacturer specifications, or experimental characterization. Once the thermal circuit model is constructed, it can be solved using numerical techniques to simulate the temperature distribution within the module. This simulation helps identify the areas of high temperature gradients and provides an estimation of the junction temperature.

FEA models offer a more detailed and complex approach for junction temperature evaluation. FEA involves dividing the IGBT module into numerous small elements or mesh cells and solving the heat transfer equations for each element [45]. FEA models require precise information about the geometry, material properties, boundary conditions, and heat generation sources within the IGBT module[46]. The accuracy of the model depends on the

quality of these inputs and the mesh resolution used in the simulation. By running the FEA model, the temperature distribution throughout the IGBT module can be obtained, allowing for an estimation of the junction temperature. The FEA approach provides a more detailed understanding of the thermal behaviour, accounting for localized variations, thermal gradients, and hotspots within the device.

Both the thermal circuit and FEA models require accurate input parameters and validation against experimental measurements to ensure their reliability. Calibration of the models can be performed by comparing the simulated results with actual temperature measurements obtained using thermal sensors or thermal cameras.

The advantage of using thermal circuit and FEA models for junction temperature evaluation is the ability to capture the spatial temperature distribution within the device [47]. This allows for the identification of potential hotspots and areas of high thermal stress, which can aid in design optimization and reliability improvement. However, it is important to note that these modelling approaches have their limitations. The accuracy of the models heavily relies on the quality of the input parameters and assumptions made during the modelling process. Uncertainties in material properties, thermal interfaces, and boundary conditions can introduce errors in the temperature estimation. Additionally, the computational cost and complexity of FEA models may pose challenges in real-time applications or large-scale simulations.

Optical methods have gained significance due to their ability to provide valuable insights into the thermal behaviour of IGBTs. This introduction explores optical-based acquisition technologies, specifically focusing on contact and non-contact methods.

Physical contact technologies require the installation of temperature sensors on chip surfaces, such as thermocouples, thermistors, and fibre sensors [9]. They can in principle provide precise and localized temperature measurements and some can provide good spatial resolution. The response time of physical contact methods is lower than 5ms due to the thermal capacitance of thermo-couples and thermistors [48]-[50]. However, the installation of sensors inside module requires careful bonding techniques and considerations for the material properties of the adhesive to ensure accurate temperature measurement. In addition, the inherent physical bulk, required wiring and conductivity of more conventional sensors (e.g. thermocouples, thermistors) can impose considerable challenges on their effective implementation in this application: this is where the fibre sensors have good potential to provide significant functional advantages in in-situ sensing in this area.

Non-contact optical technologies utilize infrared (IR) cameras to capture the thermal distribution of the IGBT chip surface without physical contact [43]. IR cameras detect and convert the infrared radiation emitted by objects into a visible image that represents the temperature distribution [51][52]. This method allows for real-time and non-intrusive measurement of the junction temperature. The cameras enable thermal monitoring without the need for direct contact with the IGBT, minimizing any potential interference or alteration of the temperature profile. IR cameras provide a holistic view of the thermal behaviour, allowing for the identification of hotspots, thermal gradients, and potential reliability issues. However, the accuracy of non-contact methods can be influenced by factors such as the emissivity of the IGBT chip surface and the presence of any obstructions that may affect the line of sight between the camera and the target measurement location, which in practical applications and chip designs can be considerable [43].

Optical technologies offer valuable acquisition methods for monitoring the junction temperature of IGBT power modules, which contribute to a better understanding of the thermal behaviour of IGBTs, facilitating the development of more efficient and reliable power electronic systems.

1.4 Problem statement

Currently, there are limited technologies available for acquiring real-time junction temperature of IGBTs online.

The junction temperature evaluation on the TSEPs of the IGBT module, provides only an quasi-average temperature estimation and assumes uniform temperature distribution throughout the device. It cannot reflect scenarios with localized hotspots or thermal gradients. Additionally, changes in electrical characteristics due to module aging can impact the accuracy of temperature estimation. Calibration precision and measurement accuracy of electrical parameters during thermal evaluation also affect the temperature accuracy. Furthermore, the use of $V_{CE (low)}$ and I_{SC} is limited to offline applications, while measuring t_{doff} requires precise nano-second measurements, and using $V_{CE (high)}$ has shown errors up to ± 30 °C due to terminal resistance effects [8] [36].

The junction temperature estimation based on thermal circuit and FEA simulation relies on thermal models that involve components geometries, material properties, thermal interfaces, and boundary conditions of the IGBT module. By simulating the thermal behaviour using computational techniques, the junction temperature can be estimated. However, these modeling approaches have limitations. The accuracy of the models heavily

relies on input parameters and assumptions made during the modeling process. Uncertainties in material properties, thermal interfaces, and boundary conditions can introduce errors in temperature estimation. Moreover, the thermal circuit method can only estimate an average temperature and assume uniform temperature distribution throughout the device, while the computational complexity and cost of FEA models pose challenges for real-time applications or large-scale simulations.

Non-contact optical techniques using IR cameras, have gained popularity for their non-intrusive nature and ability to capture thermal distributions of the IGBT chip surface. However, the accuracy of non-contact methods can be affected by factors such as the emissivity of the chip surface and the presence of obstructions, like the IGBT power module's package case, which can obstruct the camera's line of sight. This limitation restricts their application in online junction temperature measurement, making them unsuitable for industrial real-time use.

With the advancement of optical fibre sensing technologies, contact-based optical methods have emerged as one of the best options for achieving online and real-time junction temperature sensing. These methods offer precise and localized temperature measurements, enabling online in-situ temperature monitoring [20][21]. Additionally, they can withstand the high-temperature, high-voltage, and high EMI environment of IGBT modules. The FBG sensor is a promising solution for on-line, direct measurement of the IGBT junction temperature, due to its electrical/EMI immunity, small size, multiplexing, flexibility, inherent robustness, and long lifetime [53][54]. However, the installation of FBG sensors requires careful bonding techniques and consideration of adhesive material properties to ensure accurate temperature measurement. The intense thermal gradient of the IGBT chip also imposes high requirements on the FBG sensors used.

In summary, the current methods for IGBT junction temperature measurement face various challenges and limitations. The existing electrical parameter-based and thermal modeling approaches provide average temperature estimations and have accuracy limitations. Non-contact optical methods using IR cameras face challenges related to accuracy and line-of-sight obstructions. Contact-based optical methods utilizing FBG sensors offer precise and localized temperature measurements but require careful installation and consideration of thermal gradients. Despite these limitations, advancements in optical fibre sensing technologies provide promising opportunities for accurate online junction temperature measurement of IGBTs.

1.5 Aims and objectives

The aim of this thesis is to develop the technology of utilizing FBG sensors for accurate and real-time junction temperature measurement in IGBT power modules. In order to achieve this aim, the following objectives have been identified:

- 1) Develop an accurate FEA model of the IGBT power module to gain a comprehensive understanding of the thermal distribution and thermal behaviour within the module.
- 2) Design and develop laboratory test-rig facilities that enable the investigation of the electro-thermal behaviour of IGBT power modules. These facilities will provide a platform for a thorough evaluation of the performance of the in-situ FBG thermal sensing system.
- 3) Explore innovative installation approaches for FBG sensors on the surface of the IGBT chip in the power module, ensuring that they are securely and stably fixed. This will involve optimizing interface materials and sensor placement to enhance the reliability and accuracy of temperature measurements.
- 4) Investigate the impact of factors such as thermal gradients, localized hotspots, and thermal stress on the accuracy and reliability of FBG sensor based junction temperature measurement. Evaluate the performance and limitations of different FBG sensor configurations, particularly with regard to head length, to achieve reliable and precise temperature measurements.
- 5) Compare and analyze the advantages and limitations of FBG sensor-based junction temperature measurement in comparison to other existing methods, such as TSEPs-based evaluation and thermal circuit/FEA models. Validate the effectiveness of FBG sensor-based measurements through comprehensive experimental studies and comparisons with established temperature measurement techniques.

1.6 Contribution of the research

The main contributions of this research are summarized as follows:

- 1) A highly accurate FEA model of the IGBT power module is developed and presented. This model enables a thorough analysis of the thermal distribution and electro-thermal behavior of the IGBT chip under both transient and steady-state operation conditions.
- 2) Innovative installation approaches for FBG sensors on the IGBT chip surface are investigated and documented. The research explores the use of interface materials with

high viscosity, which ensures secure and stable fixation of the sensors while minimizing mechanical stress. This contributes to improved reliability and accuracy in junction temperature measurements.

- 3) The research evaluates and reports on the impact of thermal gradients and thermal stress on the accuracy and reliability of FBG sensor-based temperature measurements. The performance and limitations of FBG sensors with different head lengths are extensively assessed. It is discovered that FBG sensors with long head lengths may experience distortion in the reflected spectrum when subjected to intense thermal gradients on the IGBT chip.
- 4) A comprehensive comparative analysis is conducted to compare FBG sensor-based junction temperature measurement with V_{CE} -based evaluation techniques and thermal circuit/FEA models. This analysis validates the effectiveness of FBG sensor-based measurements and establishes their advantages and limitations. By providing a comprehensive understanding of temperature measurement techniques, this research contributes to the overall knowledge and applicability of these techniques in IGBT power modules.

1.7 Structure of the thesis

An overview and summary of each chapter is provided here in order to more easily navigate the thesis.

Chapter 2: Literature Review

This literature review includes three sections: 1) a review on the package structure and package-related ageing mechanism of IGBT power modules, and the role of the junction temperature acting in the ageing process; 2) a review on the junction temperature acquisition technologies of IGBT power modules, including TSEPs based junction temperature evaluation, thermal circuit and FEA model based temperature estimation, and thermal sensors and thermal camera based junction temperature measurement; 3) a review on FBG sensing technology and its reported applications for thermal measurement of power electronic devices.

Chapter 3: Simulation model

An electro-thermal FEA model of the IGBT power module SKM50GB12T4 is constructed in COMSOL 5.5 to investigate its thermal behaviour. Firstly, the layer structure of the IGBT power module is introduced. The dimensions of each layer are then determined

by employing both direct measurements using callipers and indirect calculation based on cross-section photos. Further, the IGBT model's thermal properties are analysed using a thermal circuit to ensure that they align with the performance outlined in the datasheet. Subsequently, the FEM model of the IGBT power module is constructed and meshed. Appropriate electrical and thermal boundaries are then assigned to the model. The thermal characteristics of the IGBT power module are subsequently simulated to identify feasible positions for the installation of FBG sensors.

Chapter 4: Test Rig

This chapter outlines the experimental test-rig used in the research; it aims to provide details of the built test-rig and the associated tools for the experimental work conducted throughout the research. This chapter includes four parts: section one focuses on the FBG thermal sensing system used in the study; section two describes the FBG sensor thermal calibration test-rig; section three introduces the main test rig built to provide DC current to heat the commercial IGBT test module; section four reports a test rig to calibrate the correlation of on-state voltage (V_{CE}), junction temperature (T_j) and collector current (I_C), which is in service for the investigating of V_{CE} based junction temperature evaluation in Chapter 7.

Chapter 5: FBG Sensor Installation and Interfacing Technologies

This chapter explores the installation methods and associated sensing performance features for direct on-chip surface temperature sensing in IGBTs using FBG technology. To this end one thermal paste and three glues with different properties are chosen as interfacing materials for comparison. The feasibility investigation of the interfacing materials includes two steps. Step 1 is to calibrate the performance of the installed FBG sensors under different interfacing materials, to check the interference induced during the installation process. Step 2 is to test the measurement accuracy and response rate of the FBG sensors fixed using different interfacing materials. Corresponding to the two steps, the in-situ calibration requirements of the IGBT installed FBG sensors are examined as a precursor to in-service thermal measurement. A range of experiments are performed to characterize the measurement performance of the studied interfacing options in a variety of IGBT operating conditions. A control group of installed FBG sensors without additive interfacing material is also built for comparison.

Chapter 6: FBG Head Size Influence on Localized On-chip Thermal Measurement in IGBT Power Modules

The thermal map of the examined IGBT power module is first simulated based on the FEA model. The chip surface heat distribution is characterized, which identifies the sensor locations of interest. Next, the in-situ thermal monitoring performance of FBG sensors with three different sizes is evaluated on two installation positions, separately. The two installation positions along with the corresponding surface temperature distribution gradients are analyzed. The impact of the thermal gradients on individual sensor performance and in-situ applicability is assessed.

Chapter 7: Comparison of FBG based and VCE based IGBT junction temperature acquisition technologies

This chapter presents an analysis of different methods for junction temperature evaluation in IGBT power modules, focusing on voltage-based approaches (V_{CE} and ΔV_{CE}) and contact temperature measurement techniques using FBG sensors. The calibration processes and results of the $V_{CE} - T_j - I_C$ and $\Delta V_{CE} - T_j - I_C$ relationships are illustrated firstly, followed by the junction temperature evaluation based on V_{CE} and ΔV_{CE} . The chip temperature is measured by the FBG sensor and a thermal camera at the same time. Comparison has been conducted to demonstrate the effectiveness of the evaluation based on V_{CE} and ΔV_{CE} , and the measurement based on thermal camera and FBG sensors.

1.8 List of publications

The following research publications were produced from this research:

Journals:

1. S. Chen, D. Vilchis-Rodriguez, S. Djurović, M. Barnes, P. McKeever and C. Jia, "Direct on Chip Thermal Measurement in IGBT Modules using FBG Technology - Sensing Head Interfacing," in *IEEE Sensors Journal*, vol. 22, no. 2, pp. 1309-1320, 15 Jan.15, 2022.
2. S. Chen, D. Vilchis-Rodriguez, S. Djurović, M. Barnes, P. McKeever and C. Jia, "FBG Head Size Influence on Localized On-Chip Thermal Measurement in IGBT Power Modules," in *IEEE Sensors Journal*, vol. 22, no. 22, pp. 21684-21693, 15 Nov.15, 2022.
3. S. Chen, D. Vilchis-Rodriguez, M. Barnes, S. Djurović, "Features of direct on-chip IGBT thermal sensing using adhesive bonded FBG sensors," in *IEEE Sensors Journal*, (in press, DOI: 10.1109/JSEN.2023.3301070).

Conferences:

1. D. S. Vilchis-Rodriguez, S. Chen, S. Djurović, M. Barnes, P. McKeever and C. Jia,

- "IGBT finite element model for fibre bragg grating sensor installation analysis," *11th International Conference on Power Electronics, Machines and Drives (PEMD 2022)*, Hybrid Conference, Newcastle, UK, 2022, pp. 184-188.
2. S. Chen, D. S. Vilchis-Rodriguez, M. Barnes, S. Djurović, " Direct Sensing of IGBT Junction Temperature using Silicone Gel bonded Fibre Bragg Grating Sensors", *12th Int. Conf. on Power Electronics Machines and Drives (PEMD 2023)*, Belgium, October 2023, (in press).

Chapter 2: Literature Review

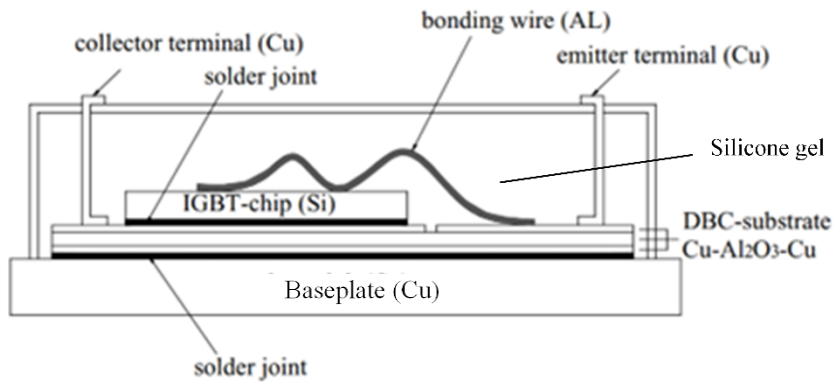
This literature review includes three sections:

- 1) a review on the package structure and package-related ageing mechanism of IGBT power modules, and the role of the junction temperature acting in the ageing process;
- 2) a review on the junction temperature acquisition technologies of IGBT power modules, including TSEP based junction temperature evaluation, thermal circuit and FEA model based temperature estimation, and thermal sensors and thermal camera based junction temperature measurement;
- 3) a review on FBG sensing technology and its reported applications for thermal measurement of power electronic devices.

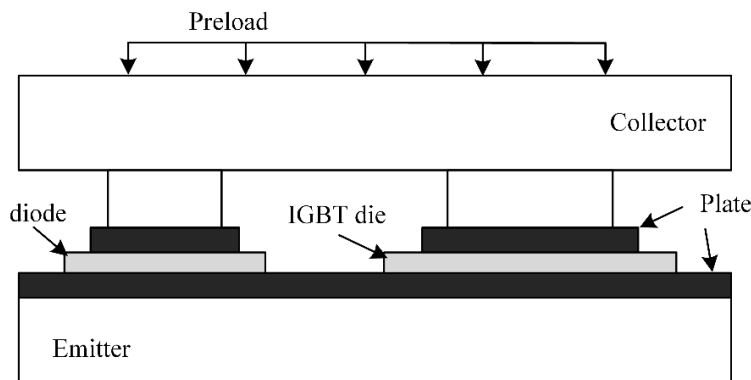
2.1 IGBT power modules package structure and failure mechanism

2.1.1 IGBT power module package structure

IGBT power modules have two primary packaging techniques: wire-bond modules and press-pack modules [5][7]. Fig. 2.1 provides cross-sectional views of these two modules [7].



(a) Wire-bond module package structure



(b) Press-pack module package structure

Fig. 2.1. IGBT package structure [7]. (a) Wire-bond modules; (b) Press-pack modules.

Wire-bond modules are the most widely used packaging technology for IGBTs. These modules utilize established and cost-effective aluminum wire bonding methods to establish electrical connections between the pads on top of the die and the output terminals [55].

The IGBT chip and bond wires are commonly covered by silicone gel. The silicone gel provides mechanical support and protection for the delicate wire bonds and other internal components within the module. It also serves to enhance the overall reliability of the module by preventing the ingress of moisture and other contaminants that could potentially cause electrical failures or corrosion over time. Moreover, acting as a thermal conductor, the silicone gel improves thermal conductivity and facilitates the efficient dissipation of heat generated during the operation of the IGBT power module. This helps maintain a more uniform temperature distribution within the power module and prevents the formation of localized hotspots that can lead to thermal stress and device degradation. Additionally, the silicone gel aids in maintaining the thermal stability of the components within the module, absorbing thermal shocks and fluctuations, and stabilizing the temperature during dynamic operational conditions.

The IGBT chip die is mounted on a Direct Bonded Copper (DBC) substrate, which typically comprises of three layers of Cu-Al₂O₃-Cu, as depicted in Fig. 2.1 (a) [7]. Alumina exhibits good insulation properties and high-temperature resistance, making it an ideal choice for packaging material. Additionally, in some specialized applications, other ceramic materials such as boron nitride (BN) or aluminum nitride (AlN) might be used, which offer higher thermal conductivity and corrosion resistance for more demanding operating environments. The DBC substrate serves several functions, including mechanical support, electrical conduction (top copper layer), electrical insulation (middle ceramic layer), and effective heat dissipation path [56], [57].

In contrast, press-pack modules rely on a pressure contact between the chip and the base plate [58], [59]. Under pressure, the IGBT chip is clamped by two metal conductors, resulting in a secure connection between the layers with excellent thermal and electrical contact [60]. The metal plates in press-pack modules are typically composed of copper or aluminum, providing electrical and mechanical connections between the chip and the power terminals [59], [60].

2.1.2 Wire-bond IGBT power modules package-related ageing mechanism.

The main ageing mechanism of IGBT power modules can be divided into chip-related ageing and package-related ageing [5], [9]. In this literature review, the focus is the

package-related ageing mechanisms of wire-bond IGBT power modules. By exploring the factors and mechanisms associated with the packaging materials and structures, we aim to highlight the role of junction temperature in the ageing process and emphasize the importance of acquiring the accurate junction temperature.

During operation, the primary sources of power loss in IGBT devices are conduction loss and switching loss, which tend to result in a temperature rise of the IGBT chip. Meanwhile, the packaging structure of the power module plays a significant role in dissipating heat. The interplay of the heat generation and the heat dissipation influences the temperature variations within the IGBT package.

In the case of wire-bond IGBT power modules, the bond wire is soldered to the IGBT chip surface, while the materials of the bond wire and chip are Al and Si, respectively. The IGBT chip is soldered on the top copper layer surface. Table 2.1 shows the coefficients of thermal expansion of relevant materials [61].

Table 2.1. CTE of different materials. [7]

Material	CTE (ppm / °C)
Aluminum	23.5
Silicon	2.49
Copper	16.4
Solder	12

Differences in the CTE between the materials used for the chip and package result in varying degrees of expansion and contraction when exposed to temperature changes. Consequently, mechanical stress is induced on the joint surface during temperature fluctuations [62]. This stress has the potential to disrupt the structure of the joint surface and is a major contributing factor to the ageing of IGBTs. Ageing of the package often manifests as bond wire lift-off and solder fatigue, which are commonly observed phenomena [9].

2.1.2.1 Bond wire lift-off

Failure of a bond wire occurs mainly due to the propagation of cracks at the interface between the bonding wire and the chip [62]. During device operation, changes in temperature and the distinct CTE between silicon and aluminium induce stress at the material interface, with the level of stress proportional to the amplitude of temperature changes [13], [63]. As temperature changes occur continuously during operation, stress cycles drive the generation and deepening of cracks. A typical crack propagation process is

shown in Fig. 2.2, where a thermal fatigue test with a sufficiently high junction temperature circle causes the crack to spread from both ends to the centre along the connection interface until the bonding wire separates [13] [64].

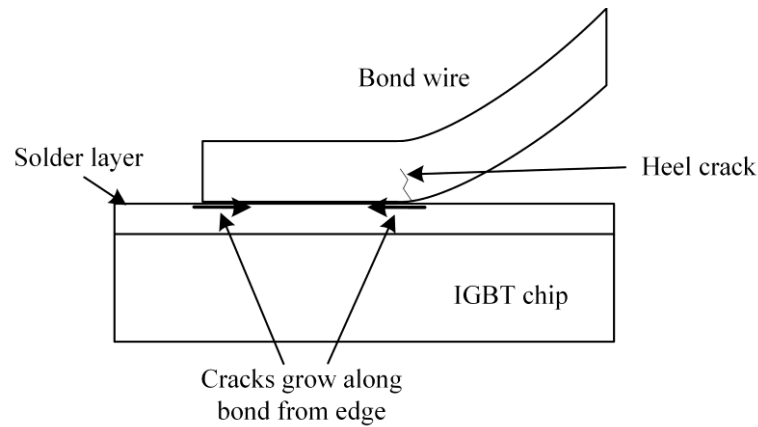


Fig. 2.2. Typical crack propagation process in bonding line [13]

2.1.2.2 Solder fatigue

Another major failure mode of wire-bond IGBT power modules is the fatigue of the solder layer between the device chip and the substrate or between the DBC and the baseplate [65]. The ageing of the solder layer is related to the initial solder microstructure and substrate metallisation [66]. This mechanism occurs because the silicon chip and the copper substrate have different CTEs, which generate shear stress in the solder layer and eventually form cracks. These cracks reduce the effective area for heat conduction from the chip to the outside. Therefore, the die becomes hotter on average, and the process accelerates as the voids grow [67]. The ageing process will accelerate as the crack grows and the gap expands. At the same time, severe local heating due to increased thermal resistance of the connection may damage the chip [68], [69].

In the case of cyclic loading, due to the power cycling, the material undergoes thermal cycling, which leads to solder strain cycling and triggers stress cycling [70]. As the number of cycles increases, the crack length in the solder increases. After a large number of cycles, the crack generation speeds up, the IGBT power module will quickly approach failure at the end of solder life.

2.2 Junction temperature acquisition technologies

There are three primary methods for obtaining the junction temperature in power devices. The first method involves establishing a correlation between the junction temperature and a particular TSEP. By measuring or calculating the TSEP, the junction temperature can be determined. The second method involves the use of thermal circuit

models and FEA simulation models to calculate the junction temperature based on the measurement of the case temperature. The third method involves the use of sensor-based technology to directly measure the junction temperature. While this method may provide more accurate measurements in the future, it requires modifications to the IGBT power module as well as electrical isolation and signal protection and presents several challenges. This review will discuss each of these three methods in detail.

2.2.1 Method based on TSEPs

Some IGBT operating electrical parameters have a strongly correlated relationship with junction temperature. By measuring or calculating the TSEP, the junction temperature can be determined. This method can measure the junction temperature without damaging the IGBT package structure.

2.2.1.1 On-state voltage at low current ($V_{CE(low)}$).

One commonly used TSEP is the on-state saturation voltage at low current ($V_{CE(low)}$), which reflects the temperature sensitive characteristics of the PN junction on-state voltage drop [28][71]. The on-state saturation voltage drop has a negative temperature coefficient when the collector current is less than a certain value [72]. [12] presented to inject a constant current of 100 mA into the IGBT collector. The IGBT $V_{CE(low)}$ was recorded with step increased junction temperature T_j , then the correlation between $V_{CE(low)}$ and T_j was determined. In silicon devices, this parameter $V_{CE(low)}$ usually exhibits a negative temperature dependence of about -2 mV/°C [12][71]. However, this parameter can only be measured when the IGBT module is in an off-work state and is not suitable for online detection.

2.2.1.2 On-state voltage at high current ($V_{CE(high)}$).

Another TSEP is the on-state voltage at high current ($V_{CE(high)}$). The saturation voltage drop has a positive temperature coefficient when the collector current is larger than a certain current [8][73]. This method measures the collector current at on-line condition and uses an offline database to calculate the junction temperature.

To estimate junction temperature this method requires information forward voltage ($V_{CEon(high)}$) and current (I_C). Several researchers have proposed various measurement circuits to estimate the forward voltage ($V_{CEon(high)}$) of the power device **Error! Reference source not found.**[36]. This method offers advantages in measuring the junction temperature in each switching cycle and in an online mode. However, a drawback is that the ohmic voltage drop of power module packaging materials becomes significant at higher

currents, leading to a large error in temperature measurement ($\pm 30^\circ\text{C}$) [8][36]. Ghimire *et al.* proposed a correction factor to mitigate this temperature error, but it requires knowledge of the power module's layout and specific measurements to formulate the corrections [35]. Another method, presented in, utilizes ΔV_{CE_AVGE} , which represents the difference in V_{CE} at two different gate voltages (15V and 13V), to evaluate the junction temperature [71]. This approach demonstrates a significant improvement in temperature evaluation accuracy, with maximum errors typically below 10°C . However, this method lacks the capability for online junction temperature monitoring. Moreover, it should be noted that the ageing of the power module can affect the on-state voltage of the device, requiring periodic updates or calibration of the correction factor as the device ages.

2.2.1.3 Short-circuit current (I_{sc}).

Short-circuit current can be used as a thermally sensitive electrical parameter [37]. The method proposed in [38] measures junction temperature using the negative temperature characteristic of short-circuit current ($-0.345 \text{ A}/^\circ\text{C}$). However, this method requires ensuring that the short circuit can be cut off in time to prevent the device from being overstressed.

2.2.1.4. Turn off delay time (t_{doff})

Some authors used the turn off delay time (t_{doff}) [39]-[42] information for junction temperature measurement.

The turn-off delay time t_{doff} is defined as a time interval when the drive voltage V_{GE} drops by 10% and the collector voltage V_{CE} rises to 90% of the bus voltage [39]. Its temperature-sensitive characteristic is actually the temperature-sensitive characteristic of the gate voltage during the Miller plateau time [40]. An increase in junction temperature will cause an increase in the IGBT turn-off delay ($1\text{-}2 \text{ ns}/^\circ\text{C}$) [39], [41].

This approach based on t_{doff} is constrained and requires high bandwidth sensor and sampling system for temperature measurement. It also requires external circuit to trigger a time-to-digital converter for extraction of turn on and turn off delay time to estimate device junction temperature.

2.2.2 Method based on the thermal circuits and FEA models

Electro-thermal analysis is a promising approach for predicting heat generation in IGBTs, particularly through dynamic electro-thermal models that offer in-situ evaluation of electric potential changes, including resistivity, dielectric constant, dissipation factor,

material properties, and geometry. In these analyses, thermal models play a vital role in calculating the junction temperature under specific power dissipation, utilizing the input of thermal power of the IGBTs.

The first and most widely used method is the thermal circuit model, also known as the compact thermal model, which is derived from a resistor-capacitor (RC) thermal network. This model provides an accurate and computationally efficient representation that can be easily incorporated into circuit simulators to estimate the instantaneous junction temperature during long-term dynamic simulations. The thermal network model discretizes the entire IGBT structure into a network of heat diffusion elements and convection heat transfer elements. By employing heat diffusion and convection equations, it calculates the temperatures of network nodes and enables accurate estimation of junction temperature.

The second method involves numerical models, predominantly computational fluid dynamics (CFD) and FEA method, for steady and transient thermal analysis. These numerical models simulate thermal performance with boundary conditions and heat resources using a large number of finite elements, offering higher accuracy by considering detailed material properties and exact physical dimensions. However, these models require significantly more time and are impractical for evaluating junction temperature variations under arbitrary load profiles or real duty cycles in operating conditions, which are critical for reliability analysis.

2.2.2.1. Thermal circuit models

The thermal network model was widely used for steady state and dynamic thermal analysis for power electronics with the basic elements of thermal resistors and thermal capacitors.

[14] proposed a methodology aimed at developing physics-based models for power electronics. They derived the thermal network of IGBTs based on the physical structure and extracted parameters that were highly influenced by temperature through experiments. [15] successfully created an accurate thermal network model for the IGBT chip. They decomposed the silicon drift region into slices and modeled each slice as an individual R-C stage, achieving optimized results with a total of 16 stages. To accurately predict power loss density in IGBTs, the electrical model must account for temperature variations. [16] used their developed thermal network models to predict temperature variations within 3 °C under transient conditions. [17], [74] presented a novel distributed electro-thermal model for analyzing the electrical and thermal characteristics of power electronics during critical

operations. Their thermal model employed a nodal method with a three-dimensional RC thermal network, discretizing material layers into volume elements characterized by thermal capacitance and resistances in 3D.

[75] introduced the Foster RC network for thermal modeling, integrating it with electrical modeling through the interaction between power loss and junction temperatures. Static and dynamic models were formulated through curve fitting based on measurements and parameter extraction from datasheets. [44] proposed a thermal network model considering substrate solder cracks within the IGBTs. They used an effective heat propagation path to adapt the RC parameters of the thermal network and assess the impact of substrate solder cracks. [76] developed a loss model for the three-level neutral point clamped rectifier to accurately calculate conduction losses and switching losses in IGBTs. The temperature distribution of the IGBTs and diodes was determined using RC equivalent equations that represented the temperature differences between the device junctions and the liquid-cooled heat sink. [77] constructed a lumped three-dimensional thermal network consisting of RC cells to precisely assess temperature fluctuations in diodes and transistors during time-dependent operations and subsequent power losses.

[78] devised a technique for in-situ junction temperature measurement of an IGBT device. Based on the online measurements of junction temperatures, they proposed a dynamic compact thermal model to calculate time-dependent thermal impedance curves of the IGBT. This model, as a real-time processing method, can be further utilized for online health monitoring of IGBTs. However, establishing thermal network models relied on the physical properties of the internal components of the IGBTs, which made it impossible to disassemble the devices and analyze thermal resistance and capacitance directly.

To construct non-destructive thermal network models, there are primarily two approaches: experimental methods and numerical simulations. [79]-[81] introduced a novel thermal network model for IGBT modules in automotive applications. They employed a parameter model for power electronics based on thermal impedance and calculated thermal resistance and capacitance using transient heat FEA method. [82] proposed an extraction method that utilized transient thermal impedance from junction to case and from case to ambient to determine thermal network parameters. [83]-[87] experimentally analyzed the thermal aspects in electro-thermal modeling. They characterized IGBT components or systems using junction-to-ambient thermal impedance and developed thermal equivalent network models.

Thermal networks based on FEA model were widely employed due to the high accuracy of FEA and the low computational time of RC networks. [88] developed two-dimensional thermal networks that discretized the heat equations using FEA and coupled them with electric models to create an adequate IGBT model. [89] analyzed static and dynamic thermal behaviours of IGBTs mounted on water-cooled heat sinks. They extracted thermal resistances and time constants for a thermal network from FEA results. The dynamic behaviour predicted by the thermal network was found to be equivalent to numerical solutions obtained from FEA, and the RC network provided valuable insight into the physical layers of the components within minutes. [90] presented a thermal modeling method applied to a multichip module used as a power converter. By conducting 3D thermal simulations and validating them through direct chip temperature measurements, they developed analytical functions for thermal impedances. [91] proposed a new approach to extract accurate thermal network models from FEA of the converter, including the module and the heat sink, for fast electro-thermal simulations of IGBTs in hybrid electric vehicles. They calibrated the FEA model using static experiments and used transient 3D FEA simulations to extract thermal impedance. These methods offered advantages in terms of increased reliability, cost reduction, and shorter design cycles by effectively addressing thermal systems with significant lateral heat spreading.

2.2.2.2. FEA Models

The FEA method has gained increasing popularity in recent years for thermal modeling of IGBTs, integrating with electrical and even mechanical field models. This is primarily due to advancements in computer capabilities, which allow for highly accurate predictions of temperature distribution based on detailed structural and material properties.

[92] employed partially coupled approaches to estimate the power loss and operational temperature of IGBT Pulse-Width Modulation (PWM) under dynamic conditions. Their aim was to accurately determine the peak junction temperature. [93] presented a 3D FEA model of a 3300V/1200A HiPak IGBT power module and analyzed the sensitivity of model parameters on simulation results. [46] utilized ANSYS Workbench to develop a precise 3D FEA thermal model, which was later simplified using Model Order Reduction (MOR). This enabled electro-thermal simulations in the CASPOC circuit simulator.

[45] [47] conducted a series of research studies on IGBTs using a coupled system approach. They combined a three-dimensional thermal simulator with a one-dimensional temperature-dependent electrical-physical model of a single IGBT cell. These studies

focused on electro-thermal simulations under unclamped inductive switching conditions of high-power trench IGBTs. [94] presented a 3D simulation strategy for unclamped inductive switching analysis of multicellular power transistors. They utilized FEA and smart mesh-refinement strategies to achieve fast and accurate simulations.

[95] integrated ANSYS/Icepak FEA with a physics-based PSpice model to achieve fast electro-thermal simulations of IGBTs. Their approach claims to surpass traditional physics simulations in terms of computational speed and accuracy. [96] investigated an electro-thermal model for voltage and temperature retrieval using a PSpice-like simulator. They synthesized the thermal layer through a PSpice-like circuit generated using an electronic design automation tool. [97] proposed a two-step thermal analysis method involving analytical calculations of power losses in key IGBT components. This information was then imported into a FEA model to conduct accurate thermal simulations.

2.2.3 Optical methods and sensor-based technologies

In optical techniques, a focused optical beam is directed towards the central region of a semiconductor chip, leading to reflection or scattering of the beam from the chip's surface due to the interaction with the chip. The amount of energy reflected or scattered, which corresponds to lattice phonons, is dependent on the local temperature of the chip. These energy changes are measured and utilized to determine the temperature of the semiconductor chip or object being studied. Various optical methods, including IR sensors [98], IR microscopes [99], optical fibres **Error! Reference source not found.**, and infrared cameras [43], have been utilized to map the temperature distribution patterns of power modules. [51] employed an optical fibre sensor to measure chip temperature during high-voltage operation, aiming to estimate the thermal impedance of the power module. However, this method has a relatively slow response time of approximately 25ms. [43] utilized an IR camera to generate a temperature distribution map across the chip surface. This non-contact temperature measurement technique provides high spatial resolution, making temperature changes easily observable. However, it requires the removal of the ceramic case and the dielectric insulating gel. Additionally, for accurate measurements, both the die and bond wires need to be coated to ensure uniform emissivity across the region. Moreover, the cost of equipment associated with this method limits its use in real-time applications. Nevertheless, these approaches are widely employed for offline thermal characterisation of power modules.

If direct access to the semiconductor chip is possible, physical contact methods can be

used to measure the junction temperature of power semiconductor devices. The spatial resolution of these physical methods depends on the size of the thermal probes used for measurement, and the response time is determined by the thermal capacitance of the probes. While physical contact methods offer high accuracy and good spatial resolution, the inclusion of embedded sensors imposes strict requirements on the electrical insulation and mechanical stability of the packaging system, and it may also alter the thermal distribution within the module. Traditional sensing techniques like thermocouples or resistance temperature detectors (RTDs) can have limitations in terms of safety, mainly due to the use of electrically conductive materials in their sensor structure [49][100]. Moreover, signals obtained from these traditional sensors are susceptible to interference from electromagnetic fields and harsh environmental (e.g. electromagnetic) conditions, compromising their accuracy. [100] compared the characteristics of a thermocouple and a thermal camera in measuring the case temperature of an IGBT module. The thermocouple exhibited a limited time constant of 200 ms compared to the thermal camera with a 19.5 Hz sampling frequency. An optical fibre operates using Semi-Conductor Band Gap (SCBG) fibre optic temperature sensing technology is proposed to measure the IGBT chip temperature [27]. The sensor is made of a miniature GaAs crystal attached to the end of an optical fibre. Light is injected into the fibre and delivered to the GaAs crystal, where light with specific wavelengths is reflected depending on the temperature. The reflected light is analysed using an optical spectrum analyser, and the resulting spectral intensity distribution is used to determine the temperature. The optical fibre is secured vertically on the chip surface through a specific point connection held in place by a small polyimide tube, which is considered delicate due to its limited contact area.

The typical response times and temperature ranges of the sensors are listed in table 2.2. It is noteworthy that the capabilities of various sensors depend on the specific type and design, or the specific configuration and setup. The FBG sensor is a promising technology suitable for the physical contact measurement, which will be introduced in Chapter 2.3.

Table 2.2. Typical response times and temperature ranges of the sensors

	response time	temperature range
IR Sensors	milliseconds to a few seconds	-50°C to 1000°C
IR Microscopes	instantaneous observation and real-time imaging	-50°C to 1000°C
FBG Sensors	microseconds to milliseconds	-200°C to 1000°C
Infrared Cameras	instantaneous observation and real-time imaging	-20°C to 2000°C
Thermocouples	a second to a few seconds	-200°C to 2500°C

2.3 FBG sensors' structure, mechanism, and applications in power electronic devices

FBG sensing technology is a promising candidate for embedded thermal monitoring of the IGBT junction because of its inherent robustness, flexibility, long lifetime, electrical/EMI immunity, multiplexing and small size [101]. Its application in IGBT junction thermal monitoring is feasible and attractive.

2.3.1 The structure of FBG sensors

An FBG sensor is a short segment imprinted into the core of a single-mode optical fibre (SMF) [102]. It is formed longitudinally on the core of the SMF by exposing it to an interference pattern of ultraviolet light, resulting in a modulated periodic refractive index [101].

Fig. 2.3 depicts the structure of an FBG imprinted in an SMF. A typical SMF consists of a cylindrical glass core with a diameter ranging between 4 to 9 μm . Surrounding the core is a cladding glass layer with a diameter of 125 μm . Because of the lower refractive index of the cladding layer compared with the core, the light is constrained to propagate within the fibre core [101]. The top layer of the SMF is the coating layer, usually made of acrylate or polyimide, which provides physical protection to the fibre.

The length of the FBG sensor, which defines the sensing area on the SMF core, typically varies between 1 to 20 mm [102]. This length is determined by the number of grating fringes and the distance between them, known as the grating period (Λ), as shown in Fig. 2.3. The number of grating fringes can reach several thousand, with the grating period in the hundreds of nanometres. The grating area has a higher refractive index compared to the core due to the fabrication process.

There are different types of FBG structures, including uniform grating, chirped grating, and superstructure grating FBGs [53]. However, in this research, only the uniform FBG structure type is used. This choice is based on its simple structure and fabrication process, making it straightforward to implement in sensing applications [103]. More specifications of the FBG sensor used in this research are introduced in Section 4.1.1 and summarized in Table 4.1.

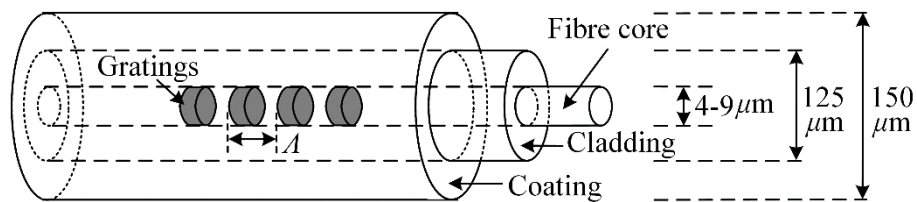


Fig. 2.3. Fibre Bragg grating sensor structure.

2.3.2 Interrogation methods of FBG sensors

In order to utilize an FBG head imprinted in an SMF as a sensor, an essential component is an interrogation mechanism that can send light to the grating head, receive the reflected Bragg wavelength, and monitor any minor shifts in the wavelength. These shifts correspond to small changes in mechanical and thermal excitation, making such an interrogation mechanism highly necessary for sensing applications [103]. One direct method for interrogating an FBG head is through the use of an optical spectrum analyzer. This technique involves illuminating the fibre with an external broadband optical source and directing the reflected light to an optical power analyzer for monitoring. However, optical analyzers are relatively expensive and large in size, which limits their suitability to laboratory-based settings rather than industrial environments.

Various interrogation schemes have been described in the literature [102] [104]. However, these techniques tend to be complex, costly, and lack multiplexing capability. As a result, they have not been successfully commercialized for real-time applications [105] [106]. A desired interrogator should possess several specifications, including high resolution, accuracy within the pico-meter range, multiplexing sensing capability, and competitive cost compared to instrument systems used for conventional electric sensors [102].

The research described in this context relies on the wavelength-division multiplexing (WDM) technique as the basis for the interrogator unit. With this technique, multiple FBG sensors combined in an SMF or distributed across several SMFs can be simultaneously monitored [106]. This interrogation technique employs a broadband light source to illuminate the FBG sensor under interrogation. Typically, the bandwidth of the broadband light source ranges from approximately 40 to 80 nm.

A scan generator is utilized to adjust the bandwidth of the broadband light source using a light filter. This enables the injected light bandwidth into the fibres to be narrowed and swept back and forth across the broadband light source window. By narrowing the light bandwidth when only a small number of FBG sensors are being interrogated, the light scan rate performed by the photodetector and the processor can be accelerated, resulting in a faster acquisition [107]. However, reducing the light source bandwidth leads to a decrease in the number of FBG sensors that can be interrogated. To address this, a coupler network is employed to inject the light bandwidth into multiple fibre channels. This coupler network allows for the interrogation of FBG with same λ_B connected to different channels. Besides,

the total number of FBG sensors that can be interrogated by one channel can be multiplied by the total number of channels.

The reflected light from the FBG sensors is detected using a photodetector, and the reflected light spectra are then transmitted to the processor. The processor processes these spectra and performs calculations to identify the peaks corresponding to the Bragg wavelengths in each spectrum.

2.3.3 The principle of the FBG sensor

FBG sensor operation consists of a periodic modulation of refraction index, where only central light wavelength matching the local modulation period can be reflected. This reflected central light wavelength will shift accordingly with strain or temperature changes. Considering a standard single mode fibre, relationship between the reflected central Bragg wavelength and strain change $\Delta\epsilon$ or temperature change ΔT is [18]:

$$\frac{\Delta\lambda}{\lambda} = (1 - p_{eff})\Delta\epsilon + (\alpha + \xi)\Delta T \quad (2.1)$$

where $\Delta\lambda$ is the change of central wavelength, p_{eff} is the photo-elastic parameter related to the fibre property, α and ξ are thermal expansion coefficient and thermo-optic coefficient of fibre core. p_{eff} , α and ξ are constants for a specified fibre.

The thermo-optic coefficient indicates the degree to which the refractive index of a material changes with variations in temperature. This coefficient is essential in understanding the impact of temperature fluctuations on the behavior of light passing through or interacting with the material. A higher thermal-optic coefficient suggests a greater susceptibility of the material's refractive index to temperature changes, influencing the material's optical characteristics.

Assuming constant strain, the reflected wavelength shift variation due to temperature change can be expressed in terms of the fibre thermal characteristics as [21][48]:

$$\frac{\Delta\lambda}{\lambda} = \left(\frac{1}{\lambda} \frac{d\lambda}{dT} + \frac{1}{n_{eff}} \frac{dn_{eff}}{dT} \right) \Delta T \quad (2.2)$$

The first part of Eq. 2.2 represents the change in λ due to the fibre thermal expansion coefficient effect α and the second part of Eq. 2.2 represents the change in due to the fibre thermo-optic coefficient effect ξ .

When broad band incident light is injected into the fibre core, the light with specific central light wavelengths will be reflected back and detected by interrogator. The reflected light wavelength is linearly proportional to temperature or strain [108]. Hence, the

temperature and strain changes can be obtained according to the wavelength change. In FBG arrays, it is noted that different wavelength values should be adopted for the FBG heads because the same wavelength may cause signal overlap received by interrogator, so that the sensor locations cannot be identified according to the received wavelength values [48][109].

2.3.4 The application of the FBG sensors in power electronics

As an advanced sensor, the FBG sensor has been used to perform localized thermal measurements within IGBT modules [20] [21] [110].

In [110], the DUT used is an IGBT module SK45GB063 manufactured by SEMIKRON. The top lid of the module case was removed, and the sensor was securely placed on the surface of the IGBT chip using mineral oil. The circuit schematic of the test setup is illustrated in Fig. 2.4. Two types of experiments were conducted. Firstly, the V_{CC} was set to a constant value of 50 V for a duration of 20 seconds, during which a constant current of 1.3 A flowed through the IGBT. The power dissipation was measured as 1.98 W, and the change in junction temperature was recorded as 1.26°C. Secondly, the V_{CC} was set to 100 V with a pulse sequence of 500 ms. The experimental results were compared with the simulation results obtained using a second-order Foster thermal model. It was concluded that a discrepancy of approximately 0.3% was achieved. However, it should be noted that the accuracy of the RC thermal model was not satisfactory, which necessitates reconsideration of the comparison process and the conclusions drawn. Furthermore, the current flowing through the DUT was close to negligible, resulting in insufficient verification. Furthermore, the FBG sensor to chip surface thermal interface was established using mineral oil which is inadequate to facilitate effective sensor to chip heat transfer elevated temperatures characteristic of standard FBG operation.

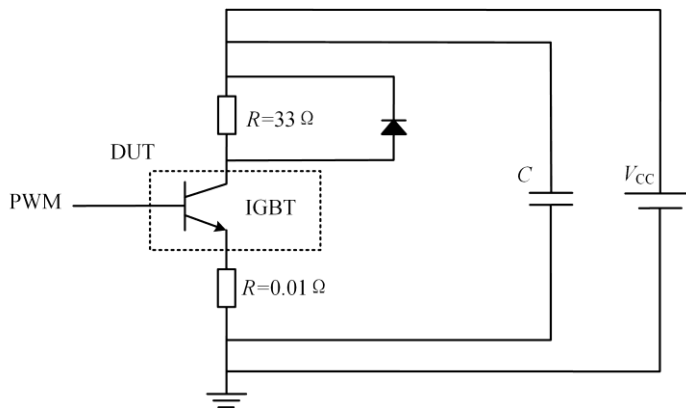


Fig. 2.4. The circuit schematic of the test rig (redrawn from [110])

In another study [21], FBG sensors are proposed for measuring the baseplate temperature of power electronic modules in wind turbine converters. The FBG sensors are embedded on the surface of the baseplate, positioned vertically beneath the target chips. The IGBT power module is installed in a single-phase full bridge inverter, controlled by a sinusoidal pulse width modulation (SPWM) signal with a switching frequency of 2550 Hz and a fundamental frequency of 50 Hz. To validate the accuracy of the FBG array sensor temperature measurements, a simple thermal resistance circuit was constructed auxiliary with case temperature measurement using type K thermocouples. The analytically calculated thermal resistance ($R_{th,TIM}$) matches its nominal value, confirming the correctness of the FBG array sensor temperature measurements.

In conclusion, the application of FBG sensors for the direct measurement of IGBT chip temperature is still in its nascent stages. Proposed embedding locations for the FBG sensors include inside the silicone gel [20] and the baseplate [21], with further evaluation of the junction temperature required using thermal circuit models or other methodologies. While one proposal suggests affixing the FBG sensor to the chip surface [110], the practicality and reliability of the suggested interface material (mineral oil) demand further consideration. The verification process presented in [110], conducted under a test with a few amperes of current, lacks persuasiveness. Additionally, available literature fails to account for the influences stemming from thermal gradients and thermal stress on the installation location and sensing performance of the FBG sensor.

2.4 Summary

In conclusion, this chapter has provided background context by reviewing important aspects related to the failure modes and temperature effects in wire-bond IGBT power modules. The review has emphasized the association between temperature and package-related failure modes.

Furthermore, the chapter has discussed primary methods for obtaining the junction temperature in IGBT power modules. These methods include establishing correlations between the junction temperature and temperature-sensitive electrical parameters, utilizing thermal circuit models and finite element analysis simulations, and employing sensor-based technology for direct temperature measurement. While the sensor-based method shows potential for accurate measurements, it presents challenges and requires modifications to the module and signal protection.

A significant portion of the background research focused on FBG sensing technology,

which is the driving force behind this PhD research. The key aspects of FBG sensing including structure, interrogation, and sensing principles, were covered. Additionally, a literature survey highlighted recent applications of FBG sensing technology in IGBT power modules.

In summary, the package-rated failure of IGBT power modules is highly related with the thermal stresses caused by temperature fluctuations and material CTE mismatches. Monitoring the thermal status of these modules is crucial for their performance, reliability, and longevity. Existing thermal monitoring techniques have limitations, particularly in hotspot monitoring. Therefore, the development of effective thermal monitoring techniques that enable improved thermal management, reliable condition monitoring and effective fault diagnosis is essential.

FBG sensing technology offers several advantages over conventional sensors, including its compact size, non-conductivity, immunity to electromagnetic interference, multiplexing capabilities, and high sensing response and stability. These features make FBG sensing an attractive solution for acquiring IGBT junction temperature and overcoming the limitations of existing thermal monitoring techniques. Commonly, temperature accuracy requirements for IGBT junction temperature measurements often fall within a range of $\pm 1^{\circ}\text{C}$ to $\pm 5^{\circ}\text{C}$, while the sampling rate of at least 1 kHz is necessary to ensure the capture of transient thermal events and temperature variations.

However, the application of FBG sensing in IGBT power modules has challenges. Thermal-mechanical cross-sensitivity in FBG sensors requires careful sensor design to account for simultaneous thermal and mechanical excitations. Additionally, the fragility of FBG sensors necessitates appropriate packaging, installation techniques, and calibration. Existing literature on embedded FBG sensing for IGBT power modules shows general feasibility but also highlights limitations in terms of sensor positioning and installation away from critical thermal hot spots.

To address these challenges, this research aims to develop a direct on-chip embedded FBG sensing system for monitoring the thermal behaviour of IGBT chips within their rated operating current range. The research will tackle the mentioned challenges to enable effective on-line thermal monitoring of IGBT power module junction temperature.

Chapter 3: Simulation Model

The SKM50GB12T4 IGBT power module produced by Semikron is utilized as the basis of the study in this chapter, in which an electro-thermal FEA model of the IGBT power module is constructed in a commercial multiphysics FEA software (COMSOL 5.5) to investigate its thermal behaviour.

Firstly, the structure of the studied IGBT power module is introduced. The dimensions of each layer are then determined by employing both direct geometric measurements using callipers and indirect calculation based on the chip's cross-sectional digital image analysis. The exact material properties are unavailable and are part of manufacturer's intellectual property, however for each modelled material layer, properties were assigned to align with those widely available in relevant literature. Further, the IGBT model's thermal properties are analysed using a thermal circuit to ensure that they align with the performance outlined in the datasheet. Subsequently, the FEM model of the IGBT power module was constructed and meshed. Appropriate electrical and thermal boundaries were then assigned to the model. The thermal characteristics of the IGBT power module were subsequently simulated to identify feasible positions for the installation of FBG sensors.

3.1 The structure and dimensions of the IGBT power module

An opened IGBT module SKM50GB12T4 is shown in Fig. 3.1. It has a layer structure as shown in Fig. 3.2. Each layer corresponds to a material as shown in Table 3.1 [5].

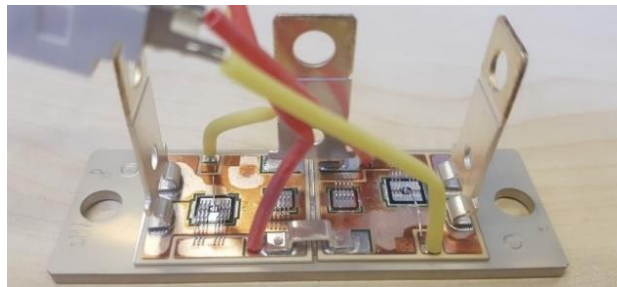


Fig. 3.1. Bare Semikron SKM50GB12T4 IGBT module used in this study

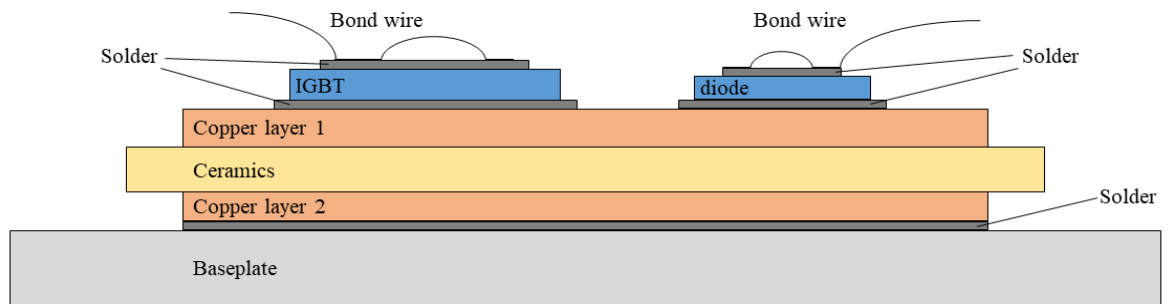


Fig. 3.2. The layered structure of the IGBT power module

Table 3.1. The name and general material of each layer [5]

Name	Material
Bond wire	Al
IGBT die	Si
Diode die	Si
Solder	SnAgCu
Copper layer 1	Cu
Ceramic	Al ₂ O ₃
Copper layer 2	Cu
Baseplate	Cu

Some dimensions of these layers were determined in this PhD research by measuring an opened commercial IGBT power module using a calliper with a resolution of 0.01 mm and an accuracy of ± 0.02 mm. Table 3.2 lists the directly measurable dimensions obtained. The dimensions that were too fine to be measured by callipers and still need to be determined (TBD) are also signed in the table.

The thickness of the IGBT chip, the diode chip, the copper layer 1, the ceramic layer, the copper layer 2 and the solder layers were estimated using a proportion method based on microscopic images, as shown in Fig. 3.3 and Fig. 3.4.

According to the Fig. 3.3, the thickness proportions of the copper layer 1, the ceramic layer, the copper layer 2 and the solder layer were determined to be 5.2: 6: 4.5: 1. The sum of the thickness of the abovementioned layers was 1.0 mm, which was measured using the calliper. Therefore, the thickness of these layers could be calculated.

In the Fig. 3.4, the thickness proportion of the copper layer 1 and the ceramic layer was 3.1: 3.6, which matched the proportion shown in Fig. 3.3. The equivalence confirmed the correctness of this method and the results. Furthermore, the thickness proportions of the copper layer 1, the ceramic layer and the IGBT die were determined to be 3.1: 3.6: 1.9, thereby enabling the calculation of the thickness of the IGBT die. The same method was used to determine the thickness of the diode die. However, the thickness of the solder layers adjacent to the IGBT die could neither be measured nor calculated, and thus, it was assumed that the thickness of all solder layers was equal. Consequently, all dimensions were determined, and Table 3.3 presents the complete set of results.

Table 3.2. The directly measurable dimensions of each layer

Name	Length, l, mm	Width, w, Mm	Height, d, mm
IGBT die	7.20	6.80	TBD
Solder1_I	5.40	5.00	TBD
Solder2_I	7.80	7.40	TBD
Diode die	5.40	5.40	TBD
Solder1_D	4.00	4.00	TBD
Solder2_D	6.00	6.00	TBD
Copper layer 1	/	/	TBD
Ceramics	30.50	28.00	TBD
Copper layer 2	28.50	26.00	TBD
Solder	28.50	26.00	TBD
Baseplate	91.00	31.00	3.00
Thermal grease	TBD	TBD	TBD
Heat sink	100.00	50.00	/

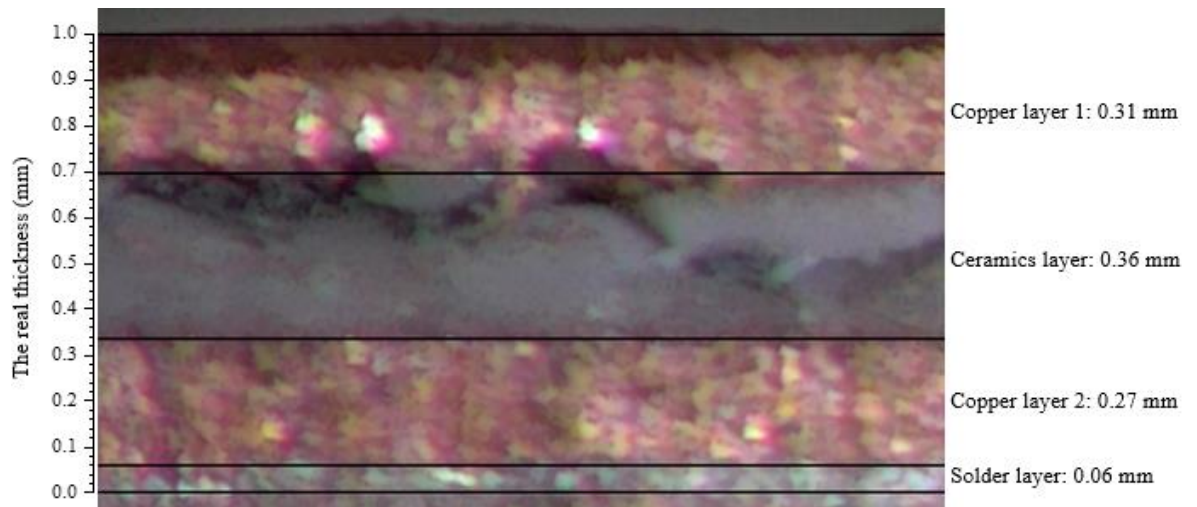


Fig. 3.3. The cutting section picture of the IGBT power module

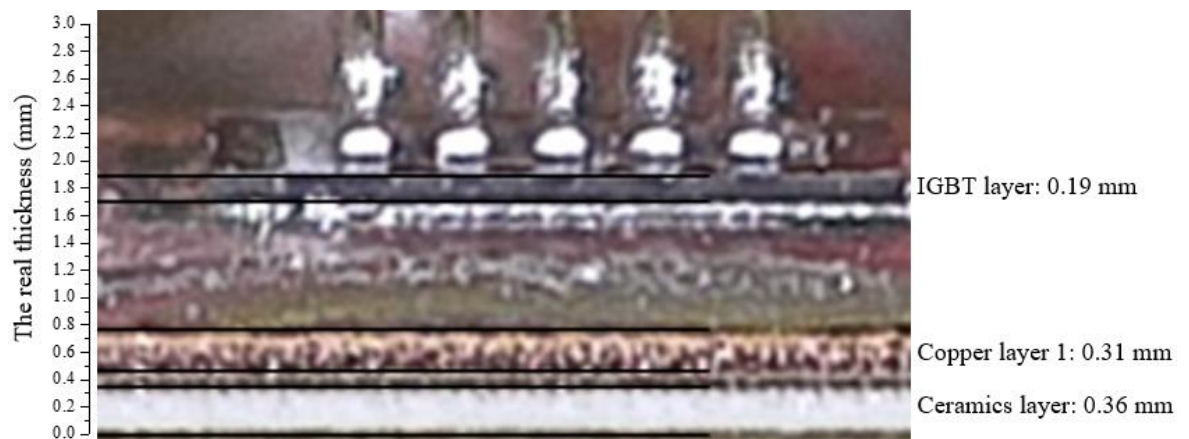


Fig. 3.4. The front section picture of the IGBT power module.

Table 3.3. The dimensions of the model

Name	Length, l, mm	Width, w, mm	Height, d, mm	Diameter, D, mm
Bond wire	/	/	/	0.20
IGBT die	7.20	6.80	0.19	/
Solder1_I	5.40	5.00	0.06	/
Solder2_I	7.80	7.40	0.06	/
Diode die	5.40	5.40	0.19	/
Solder1_D	4.00	4.00	0.06	/
Solder2_D	6.00	6.00	0.06	/
Copper layer 1	/	/	0.31	/
Ceramics	30.50	28.00	0.36	/
Copper layer 2	28.50	26.00	0.27	/
Solder	28.50	26.00	0.06	/
Baseplate	91.00	31.00	3.00	/
Thermal grease	91.00	31.00	0.2	/
Heat sink	100.00	50.00	/	/

3.2 Literature review based determination of material properties

Some available publications have provided some typical details of the layered structure of IGBT, together with the material of each layer and the thermal properties of each material. The thermal properties mainly include the thermal conductivity, the heat capacity, and the density. In the first stage of the FEM model building, only the thermal conduction is considered. The electrical physics related parameters like electrical conductivity is discussed in Chapter 3.5.

To be precise, the thermal conductivity, the heat capacity and the density all change with the temperature. However, in order to simplify the calculation and the analysis under acceptable error conditions, these thermal parameters are regarded as constants in some publications. For example, the same thermal conductivities as shown in Table 3.4 were reported in [111] and [112] in 1998 and 2003 respectively. In contrast, different thermal parameters are also reported as shown in Table 3.5 [113], Table 3.6 [114] and Table 3.7 [115] respectively in 2008, 2011 and 2016.

Table 3.4. Reports on Thermal Conductivities [111][112]

Material	Thermal conductivity, λ , W/(m*K)
Si	150
Al	240
Cu	390
Solder (Au97Si3)	27
Solder (Pb63Sn37)	50
Al ₂ O ₃	30

Table 3.5. Reports on Thermal Parameters [113]

Material	Thermal conductivity, λ , W/(m*K)	Heat capacity, c_p , J/(kg*K)	Density, ρ , kg/m ³
Si	146	750	2330
Al	220	880	2700
Cu	398	380	8850

Table 3.6. Reports on Thermal Parameters [114]

Material	Thermal conductivity, λ , W/(m*K)	Heat capacity, c_p , J/(kg*K)
Si	100	741
Al	220	896
Cu	380	381
Al ₂ O ₃	25	850-1000
Solder	28	/

Table 3.7. Reports on Thermal Conductivities [115]

Material	Thermal conductivity, λ , W/(m*K)
Si	139
Cu	386
Solder (SnAgCu)	78
Al ₂ O ₃	18

In order to ensure precision, the condition that the thermal conductivity and the heat capacity would change with the temperature is considered in some papers. In [116], the thermal conductivities of Si and Cu are piecewise linearized with the temperature while other parameters are set to constants, as shown in Table 3.8. Moreover, Wu piecewise linearized the thermal conductivity and heat capacity of Al, Si and Cu as shown in Table 3.9 [117].

In addition, some research gave the precise relationship between thermal parameters and temperature because they focused on accuracy improvement. For example, An used the least squares method to fit the data given in [118] to precisely describe the relationships [119]. [120] compared the junction temperature estimated from two thermal models respectively with 1) constant thermal conductivity and specific heat capacity and 2) non-constant thermal conductivity and specific heat capacity, in which comparatively large differences can be seen. The constant thermal parameters are shown in Table 3.10 while the non-constant thermal parameters are shown in Table 3.11.

Based on the abovementioned literature review, key values for the thermal parameters of different materials are summarized as shown in Table 3.12.

Table 3.8. The thermal parameters reported in [116]

Material	Thermal conductivity, λ , W/(m*K)			Heat capacity at constant pressure, c_p , J/(kg*K)	Density, ρ , kg/m ³
	0°C	100°C	200°C		
Si	168	112	82	705	2330
Cu	401	391	389	384	8954
Solder (SnAgCu)	57			220	7370
Al ₂ O ₃	35			880	3890

Table 3.9. The thermal parameters reported in [116]

Material	Thermal conductivity, λ , W/(m*K)			Heat capacity at constant pressure, c_p , J/(kg*K)			Density, ρ , kg/m ³
	25°C	75°C	125°C	25°C	75°C	125°C	
Si	148	119	98.9	705	757.7	788.3	2329
Al	237	240	240	897	930.6	955.5	2700
Cu	401	396	393	385	392.6	398.6	8960
Solder	\	\	\	\	\	\	7500

Table 3.10. Constant thermal parameters [120]

Material Layer	Thermal conductivity, λ , W/(m*K)	Heat capacity at constant pressure, c_p , J/(kg*K)	Density, ρ , kg/m ³
Silicon	84	711.8	2300
solder	38	129.8	9700
copper	400	385.2	8900

Table 3.11. Non-constant thermal parameters [120]

Material	Thermal conductivity, λ , W/(m*K) Power Fit: $y = a x^b$		Heat capacity at constant pressure, c_p , J/(kg*K) Quadratic Fit: $y = a + b x + c x^2$		
	a	b	a	b	c
Copper	608	-0.07	178	2.36	-2.06×10^{-3}
Silicon	438056	-1.4	293	0.396	-3.2×10^{-4}
Solder	242	-0.23	134	0	0

Table 3.12. Key values for the thermal parameters

Materials	Thermal conductivity, λ , W/(m*K)				Heat capacity, c_p , J/(kg*K)				Density, ρ , kg/m ³
	25°C	75°C	125°C	Range	25°C	75°C	125°C	Range	Range
Si	148	119	98.9	84-150	705	757.7	788.3	705-788.3	2300-2330
Al	237	240	240	220-240	897	930.6	955.5	880-955.5	2700
Cu	401	396	393	380-401	385	392.6	398.6	380-398.6	8850 - 8960
Al ₂ O ₃	45	30	25	18-35	835	880	920	835-1000	3890
Solder	66	63	60	27-78	130	130	130	129.8-220	7370-7500

In order to simplify the simulation model and reduce the calculation, constant values are preferred to be assigned to the thermal parameters of the IGBT module materials. At the first step, those values of the thermal parameters at 75 °C are chosen as the initial values used in the model, as shown in Table 3.13.

Table 3.13. Initial thermal parameters of the materials

Layers' Name	Material	Thermal conductivity, λ , W/(m*K)	Heat capacity at constant pressure, c_p , J/(kg*K)	Density, ρ , kg/m ³
IGBT die and Diode die	Si	119	757.7	2329
Bond wire and terminals	Al	240	930.6	2700
Copper layer and baseplate	Cu	396	392.6	8850
Ceramics	Al ₂ O ₃	30	880	3890
Solder	SnAgPb	63	130	7370

3.3 Thermal circuit based modification of material properties

The material properties for each layer are sourced from available literature, providing general ranges for these properties. Since the transient thermal response is critical for this study, special attention is given to the transient thermal impedance of the FEA model. The

transient thermal impedance provided by the manufacturer datasheet is used as a reference. Accordingly, a thermal circuit of the IGBT power module is constructed and analysed in this subsection to optimize the parameters chosen for material properties.

The thermal resistance and the thermal capacitance along the heat flux direction can be calculated using equations (3.1) and (3.2)

$$R_{th} = d / (\lambda \times A) \quad (3.1)$$

$$C_{th} = c_p \times \rho \times V \quad (3.2)$$

where d is the thickness, λ is the thermal conductivity, c_p is the heat capacity at constant pressure and ρ is the density. These parameters' values are introduced in Section 3.1 and 3.2.

As for the A , the effective area, should be considered carefully. Because the heat conducts not only in vertical direction, but also in horizontal direction, as shown in Fig. 3.5. [121] studies the method to calculate the angle α to calculate the effective area accurately, but the equations are very complex. Generally, an $\alpha = 45^\circ$ can be used in normal condition to reduce the amount of calculation [122].

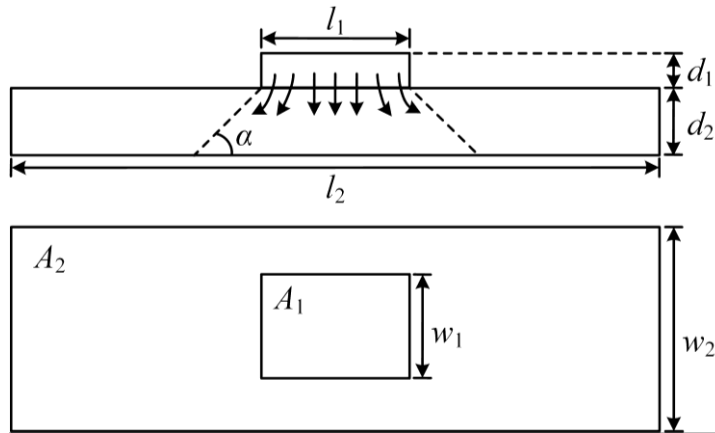


Fig. 3.5. The conduction of the heat between two layers

Therefore, the effective conduction area is calculated as equation (3.3)

$$A = (l_1 + d_2/2) \times (w_1 + d_2/2) \quad (3.3)$$

The thermal resistance and the thermal capacitance of the seven layers (the IGBT layer, the solder layer 1, the copper layer 1, the ceramic layer, the copper layer 2, the solder layer 2 and the baseplate layer) are calculated based on equation (3.1-2) and the material and geometric properties of the studied IGBT module listed in Tables 3.3 and 3.13: the results are shown in Table 3.14.

From the derived thermal resistance and capacitance values a seventh order Cauer

thermal circuit can be built, as shown in Fig. 3.6. When a step signal with amplitude of 1W is applied on the heat source side, the transient thermal impedances of the entire module and each individual layer can be plotted, as shown in Fig. 3.6.

The transient thermal impedance of each layer represents the proportionate influence of that layer within the transient time domain. For instance, the ceramics layer exhibits the most substantial effect on the thermal response beyond 10 ms, accounting for three-fifths of the total impedance.

Table 3.14. The thermal parameters of each layer

Layers	Thermal resistance	Thermal capacitance	Time constant
IGBT layer	0.0326	0.0164	5.35×10^{-4}
solder layer 1	0.0191	0.0029	5.54×10^{-5}
copper layer 1	0.0142	0.0594	8.43×10^{-4}
ceramic layer	0.1828	0.0809	1.48×10^{-2}
copper layer 2	0.0089	0.0715	6.36×10^{-4}
solder layer 2	0.0116	0.0047	5.45×10^{-5}
baseplate layer	0.0515	1.532	7.89×10^{-2}

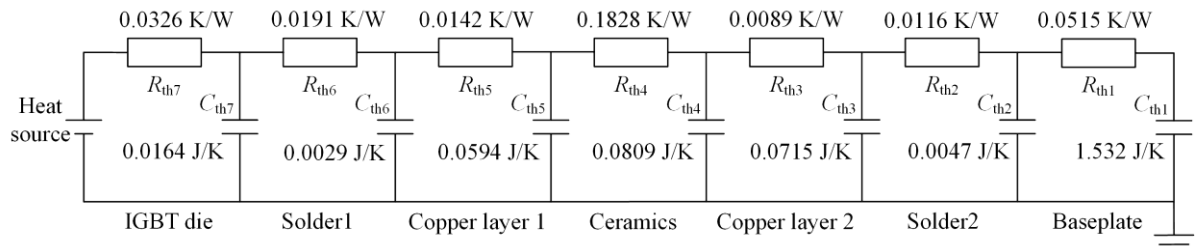


Fig. 3.6. The initial Cauer thermal circuit

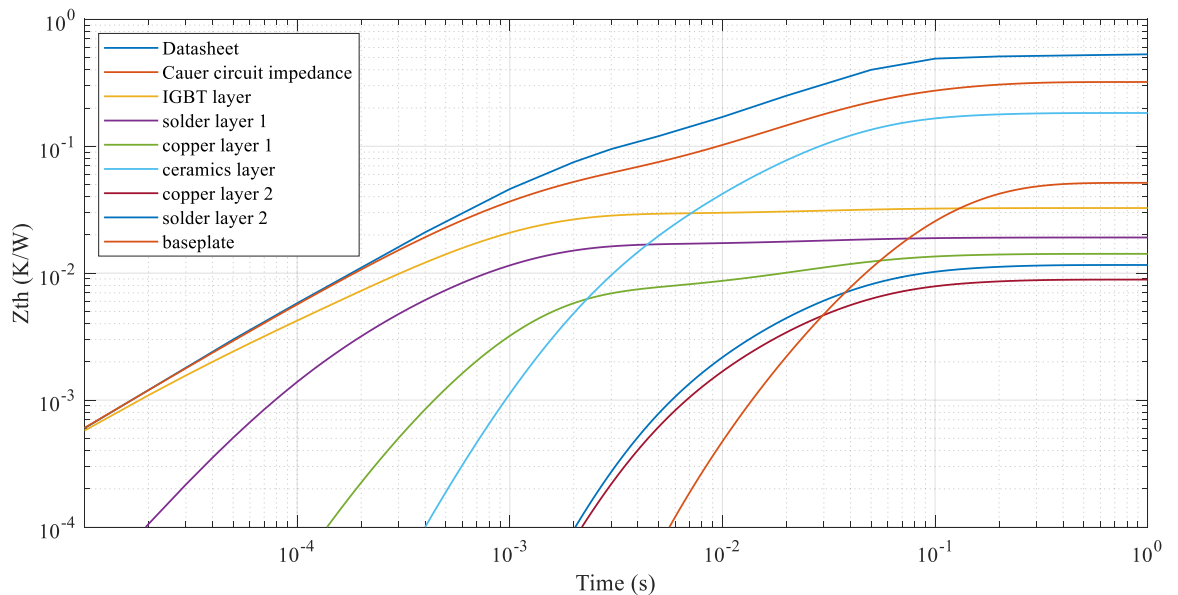


Fig. 3.7. The transient thermal impedance

In Fig. 3.7, the Cauer circuit impedance is seen to fit well with the transient thermal impedance given by the datasheet when time is lower than 10^{-4} s, which means the parameters of the IGBT layer shown in the figure in orange may be assumed to be accurate in lower than 10^{-4} s range. However, the total thermal impedance is lower than that of the datasheet impedance. This suggests that the problem lies with the ceramics layer because the ceramics layer plays the major role when time is larger than 10 ms. The thermal conductivity of the ceramics can be changed from current 30 W/(m*K) to 18 W/(m*K), which is the minimum value shown in Table 3.12. Then the improved transient thermal impedance shown in Fig. 3.8 is drawn. Compared with the transient thermal impedance shown in Fig. 3.7, the Cauer circuit impedance curve becomes closer to the datasheet impedance curve in the time range larger than 0.1 s.

The result still shows a considerable difference between the datasheet curve and the Cauer circuit impedance curve in the time larger than 1 ms and smaller than 0.1 s regions. Again if we focus on the layers that have significant impact - solder layer 1 becomes the focus and it is chosen to be improved to reduce the difference. The problem with the solder layer 1 is that its thickness cannot be accurately determined with the techniques available to this project. Its current thickness is assumed to be the same as solder layer 2. Since the solder material has a large thermal conductivity range in the literature review, the logical conclusion is to try to fit the Cauer circuit transient impedance with the datasheet impedance by improving the parameters of the solder layer 1. When its thermal conductivity is changed from current 63 W/(m*K) to 27 W/(m*K), and its thickness is changed from 0.06 mm to 0.10 mm, the Cauer circuit impedance fits with the datasheet transient thermal impedance well as shown in Fig. 3.9. These parameters are within the allowable tolerance range for this layer.

The improved thermal parameters are shown in Table. 3.15. The improved material properties and geometry dimensions are listed in Table 3.16 and Table 3.17. The corresponding Cauer thermal circuit is shown in Fig. 3.10.

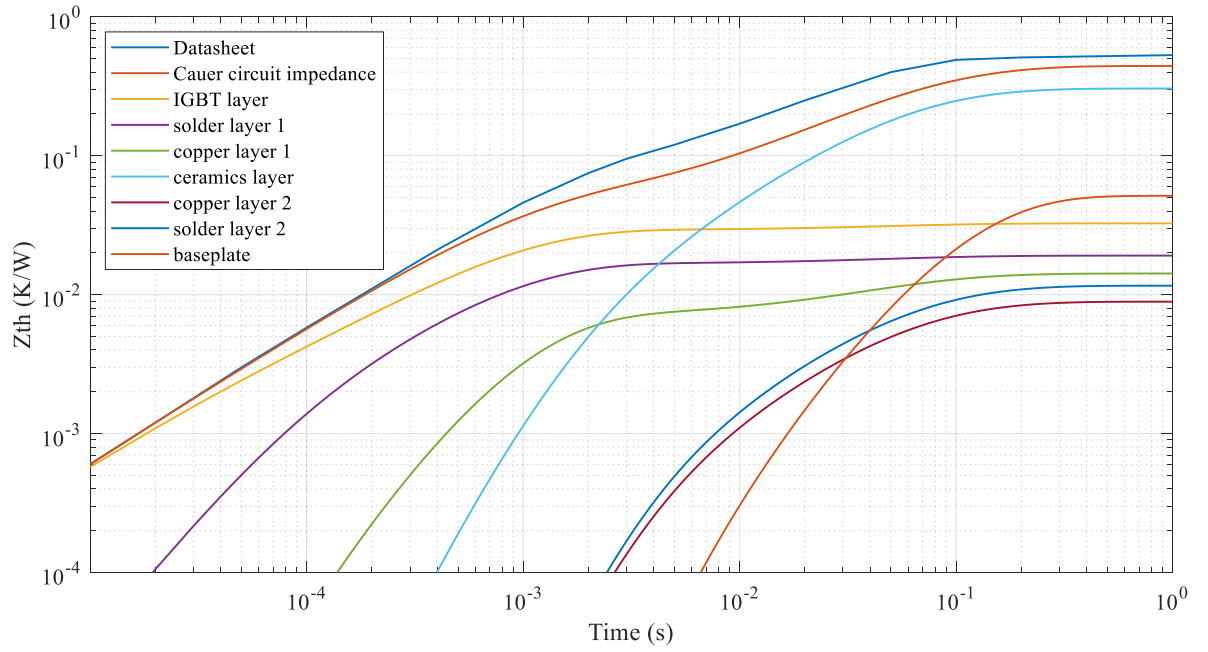


Fig. 3.8. The improved transient thermal impedance

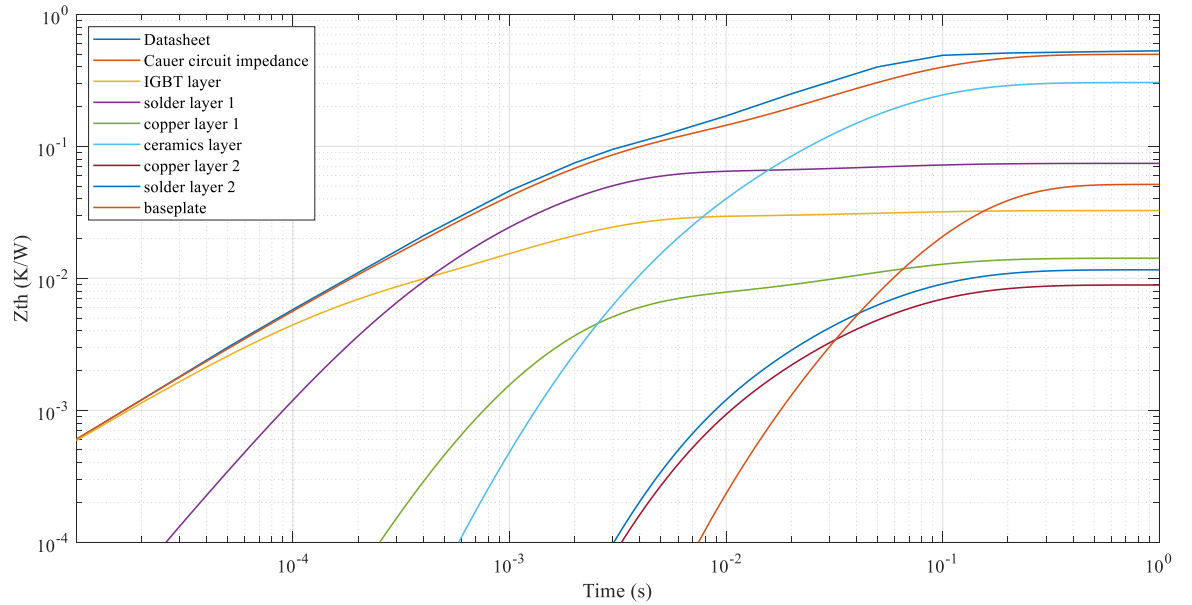


Fig. 3.9. Final transient thermal impedance

Table 3.15. Thermal parameters of each layer

Layers	Thermal resistance	Thermal capacitance	Time constant
IGBT layer	0.0326	0.0164	5.35×10^{-4}
solder layer 1	0.0743	0.0048	3.57×10^{-4}
copper layer 1	0.0142	0.0594	8.43×10^{-4}
ceramic layer	0.3047	0.0809	2.47×10^{-2}
copper layer 2	0.0089	0.0715	6.36×10^{-4}
solder layer 2	0.0116	0.0047	5.45×10^{-5}
baseplate layer	0.0515	1.532	7.89×10^{-2}

Table 3.16. Thermal parameters of the materials

Layers' Name	Material	Thermal conductivity, λ , W/(m*K)	Heat capacity at constant pressure, c_p , J/(kg*K)	Density, ρ , kg/m ³
IGBT die and Diode die	Si	119	757.7	2329
Bond wire and terminals	Al	240	930.6	2700
Copper layer and baseplate	Cu	396	392.6	8850
Ceramics	Al ₂ O ₃	18	880	3890
Solder	SnAgPb	27	130	7370

Table 3.17. Dimensions of the model

Name	Length, l , mm	Width, w , mm	Height, d , mm	Diameter, D , mm
Bond wire	/	/	/	0.20
IGBT die	7.20	6.80	0.19	/
Solder1_I	5.40	5.00	0.10	/
Solder2_I	7.80	7.40	0.10	/
Diode die	5.40	5.40	0.19	/
Solder1_D	4.00	4.00	0.10	/
Solder2_D	6.00	6.00	0.10	/
Copper layer 1	/	/	0.31	/
Ceramics	30.50	28.00	0.36	/
Copper layer 2	28.50	26.00	0.27	/
Solder	28.50	26.00	0.10	/
Baseplate	91.00	31.00	3.00	/
Thermal grease	91.00	31.00	0.2	/
Heat sink	100.00	50.00	/	/

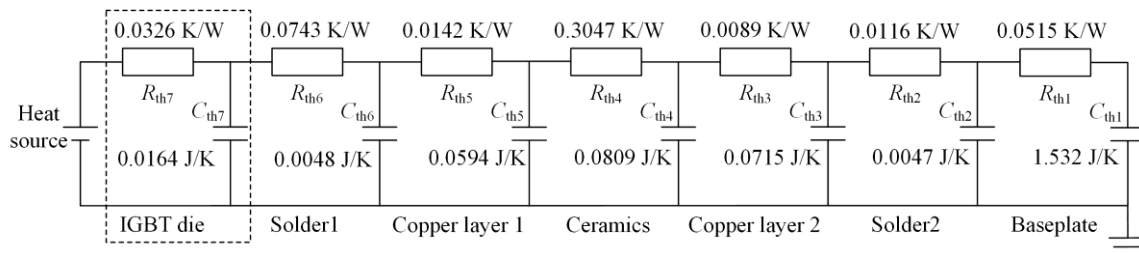


Fig. 3.10. The final Cauer thermal circuit

3.4 Simplification of IGBT FEA model and the mesh detail

Based on the abovementioned illustration, the dimensions and material properties of the IGBT power module were determined. The FEM model of the IGBT power module was built as shown in Fig. 3.11, where the layered structure of the IGBT power module is presented. The IGBT chip is simplified as a rectangular solid of silicone. The bottom surface of the chip is the IGBT collector, soldering on the copper layer. The chip top surface covered with a circle of solder layer is the emitter where six bond wires are soldered on. The gate of the IGBT is located at the centre and soldered with a bond wire connecting to the control port.

The copper layer 1 marked using orange colour provides a good electrical conduction path for the IGBT chip and the diode, and also offers an effective thermal path to dissipate the heat generated by the chip. The yellow layer is ceramic, generally consists of Al_2O_3 , which has capability to provide effective electrical insulation and thermal conduction.

In some cases, to reduce model complexity and decrease computing time, the heat sink and the thermal pad can be omitted as shown in Fig. 3.12 (a). Meanwhile, the simulation study will focus on only one IGBT chip and does not consider the thermal coupling with other parts. To further reduce model complexity and decrease computation time, only the module's left half side is considered in simulation because of the symmetrical structure of the IGBT power module. To further simplify the model, the diode operation is neglected in this study. This is achieved by removing the respective bond wires, further reducing the model complexity. Thus, the diode is disconnected from the electrical circuit. The simplified geometry used in the simulations and the model electrical terminals are shown in Fig. 3.12 (b).

In summary, the key assumptions in the FEA model include three aspects. 1) The IGBT chip is assumed to be a rectangular solid of silicone, characterized by homogeneous properties of Si material. 2) Several components are omitted, including the heat sink, thermal pad, silicone gel, the left half side of the modules, and the bond wires on the diode chip. Consequently, the thermal boundary conditions are adjusted to ensure consistent thermal simulation, as outlined in Section 3.5. 3) The material properties are assumed to be constant, remaining unaffected by temperature variations, as discussed in Section 3.3.

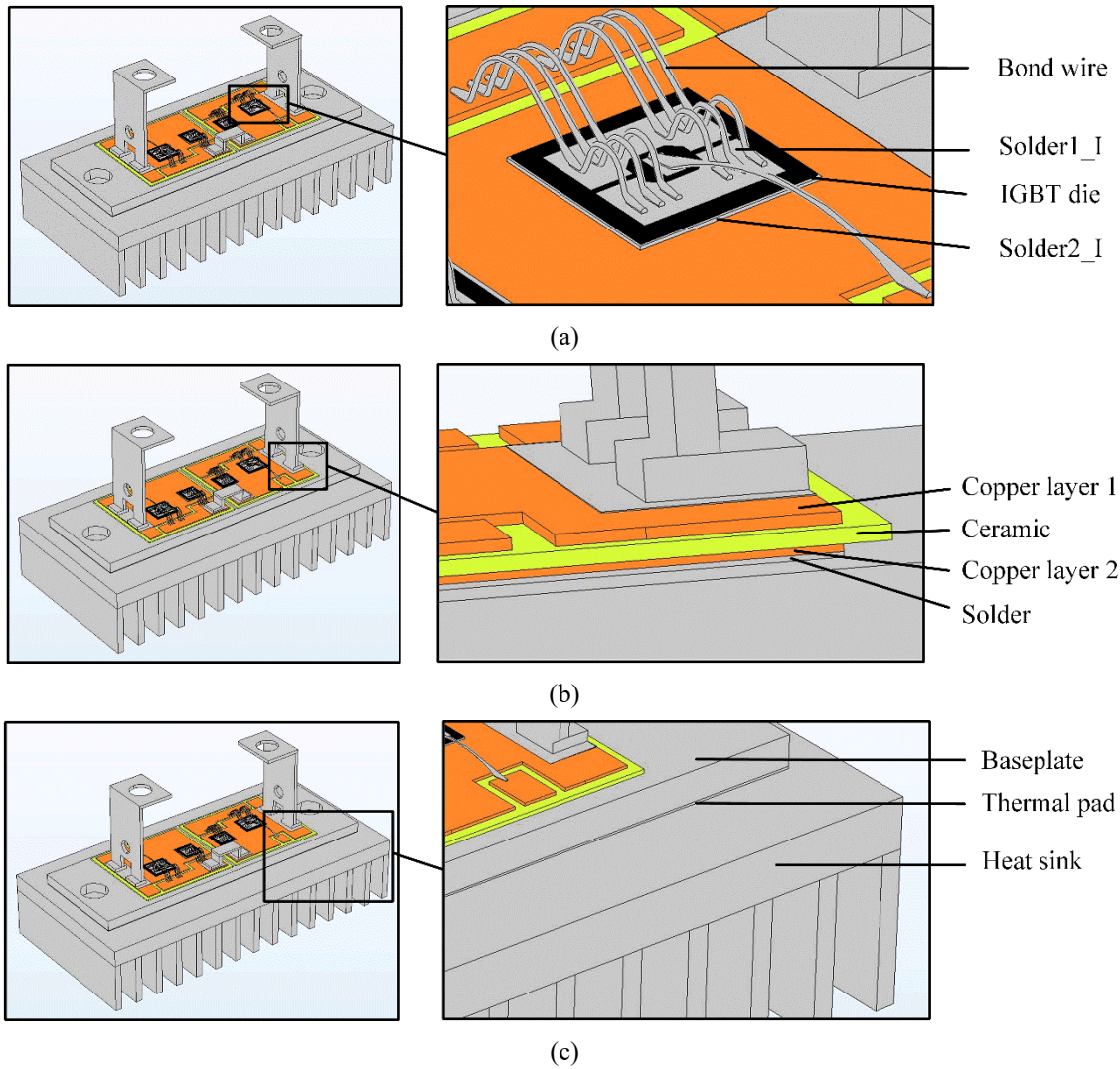


Fig. 3.11. The FEA model of IGBT power module. (a) Detail structure of the chip and the bond wires. (b) Detail structure of the ceramic layer and the copper layers. (c) Detail structure of the baseplate and the heat sink

The next step in the simulation process for COMSOL involves meshing of the model. The meshing function is an indispensable aspect of this process as it enables the accurate and efficient numerical resolution to be determined that is suitable to the features of the physical system under analysis. The function divides the continuous geometry into a collection of finite elements that are small in size, which can be utilized to numerically solve the underlying equations that describe the physical system. Increasing the number of elements in the mesh can enhance the accuracy of the solution, but also increases the computational cost and memory usage. Conversely, reducing the number of elements can lower computational cost and memory usage, but may lead to a less accurate solution.

For the purpose of this study, the chip and its bond wire components are of core interest and have small dimensions. Conversely, other components such as the baseplate, copper layer, ceramic layer, and terminals have relatively large dimensions, but are not of interest

to this study. Therefore, the model is fine-meshed in areas with small dimensions but coarse-meshed in areas with large dimensions, with a high value assigned to the element growth rate. A detailed illustration of the mesh is provided in Fig. 3.13.

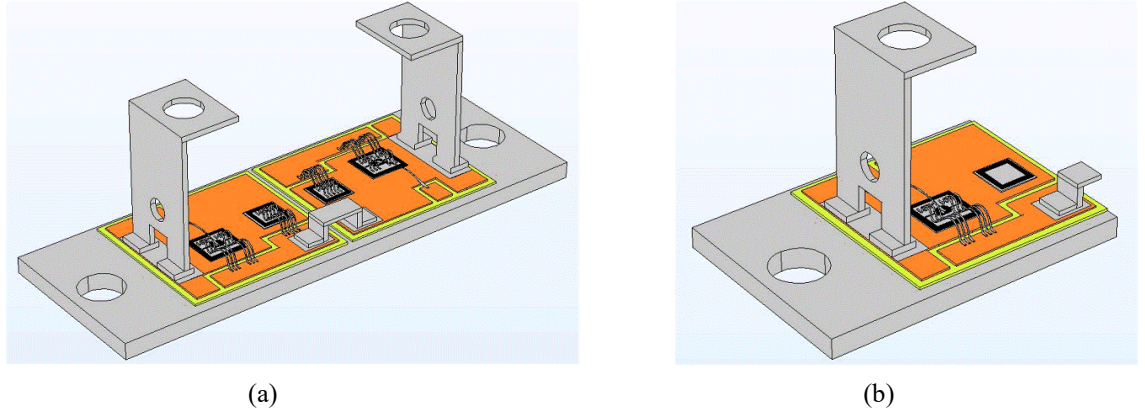


Fig. 3.12. The IGBT FEA model geometry. (a) The FEA model without heat sink. (b) The IGBT half module.

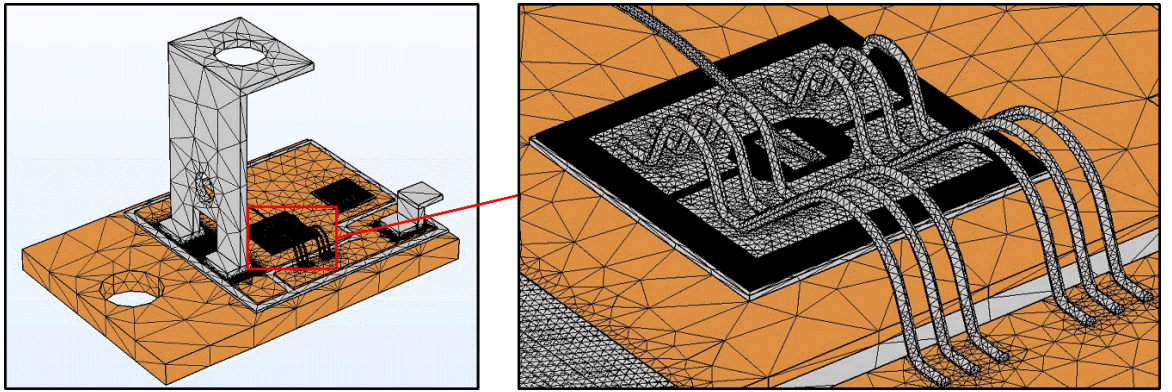


Fig. 3.13. The mesh detail of the IGBT half model

3.5 Electro-thermal performance simulation

In Section 3.4, the IGBT power module FEA model is simplified from Fig. 3.11 to Fig. 3.12 (a) and then to Fig. 3.12 (b). The section outlines the electrical and thermal boundary settings and presents stationary and transient simulation results to demonstrate the FEA model's performance.

3.5.1 Electrical boundary setting

The electrical physics is then added into the FEA model, with the electrical conductivity of each material set as shown in Table 3.18. Because the internal structure of the IGBT chip is not modelled, the switching on and off of the IGBT chip will be simulated by changing the electrical conductivity. The electrical conductivity of the chip is thence defined as a function $\sigma_{SI}f(t)$. In stationary study, $f(t)$ is set to 1; while in transient study, $f(t)$

can be set to a piecewise function if needed. Equation 3.1 shows an example of $f(t)$ when the PWM control signal is 50% duty cycle and 1kHz frequency.

$$f(t) = \begin{cases} 1 & 0 \text{ ms} \leq t < 0.5 \text{ ms} \\ 0 & 0.5 \text{ ms} \leq t < 1 \text{ ms} \end{cases} \quad (3.1)$$

The value of σ_{Si} is based on the output characteristic of the IGBT power module's datasheet: the typical value of $V_{CE(sat)}$ is 1.85 V at 25°C and 2.25 V at 150 °C. The relationship between $V_{CE(sat)}$ and junction temperature T_j can be linearized:

$$V_{CE(sat)} = 1.77 + 0.0032 T_j \quad (3.2)$$

Therefore, at the rated current $I_{C(rate)}$, σ_{Si} is represented by Equation 3.3.

$$\sigma_{Si} = \frac{d_{IGBT} \cdot I_{C(rate)}}{A_{IGBT} \cdot V_{CE(sat)}} \quad (3.3)$$

where d_{IGBT} is the IGBT chip thickness and A_{IGBT} is the chip top surface area.

Table 3.18. Thermal parameters of the materials

Layers' Name	Material	Electrical conductivity, σ , S/m
IGBT die and Diode die	Si	$\sigma_{Si} \cdot f(t)$
Bond wire and baseplate	Al	3.77×10^7
Copper layer	Cu	5.81×10^7
Ceramics	Al_2O_3	1.50×10^{-7}
Solder	SnAgPb	9.10×10^6

In this study, the IGBT chip is controlled using a PWM signal with a 50% duty cycle and variable frequencies. The IGBT chip is on when the PWM control signal is at a high voltage level and off at a low voltage level. In transient study, a reasonable operation mode is that when the IGBT is on, a current with amplitude of $I_{C(rate)}$ flows through the chip, while no current flows through the chip when the IGBT is off (ignoring the leakage current). The current in this operation can be substituted using its root mean square (RMS) value for stationary study. Since the duty cycle is 50%, the RMS value can be calculated using:

$$I_{RMS} = \sqrt{\frac{1}{2} I_{C(rate)}^2} \quad (3.4)$$

3.5.2 Thermal boundary setting and simulation results

In the forthcoming Chapter 4, a test rig will be introduced, wherein the IGBT power module is attached to a heat sink designed for forced air-cooling. The heat sink is equipped

with a fan, powered by a DC power supply. The fan's rotational speed can be adjusted by altering the supply voltage, resulting in an adjustable cooling capacity for the heat sink. To remain faithful to real power module conditions in the lab, the FEA model aims to simulate thermal boundaries as closely as possible. The heat transfer coefficient (h) of each surface is thus selected from a suitable range, allowing the FEA model to approximate experimental results. The range for the h value for forced air cooling surfaces usually falls between 10 and 500 W/(m²·K), while it lies between 1-10 W/(m²·K) for natural air cooling [123].

In the complete model depicted in Fig. 3.11, the heat sink fin surfaces are exposed to forced cooling air. After adjusting the h values, the FEA model generates a thermal distribution shown in Fig. 3.14, which is almost same as the experiment thermal distribution when the heat sink fan is running at the maximum power. The heat transfer coefficient for the heat sink fin surfaces is set to 300 W/(m²·K), while it is 5 W/(m²·K) for other surfaces. Additionally, both the initial temperature and ambient temperature are fixed at 25°C.

In the following step, the heat sink is removed, and the IGBT power module baseplate bottom surface, which is in contact with the heat sink, needs to experience high thermal dissipation to achieve the same effect – i.e. as if the heat sink were still in place. Therefore, the h value for the baseplate bottom surface is set to 3000 W/(m²·K), as depicted in Fig. 3.15, which yields a thermal distribution comparable to the one shown in Fig. 3.14.

Next, the IGBT FEA model is simplified further to a half model, wherein the baseplate area is halved, resulting in a reduction of the effective cooling area. Consequently, a higher h value is required. Finally, the h value for the baseplate bottom surface is set to 3800 W/(m²·K) to ensure that the IGBT chip retains the same thermal distribution as before the simplification. The simulation result of the half model is shown in Fig. 3.16. The inset of Fig. 3.16 shows the detail thermal distribution of the IGBT chip and bond wires, where the highest temperature is observed on the bond wires. This is because the heat dissipation of the bond wires is limited: The Joule heat generated on the bond wires is mostly conducted to the chip, whereas the covering of air or silicone gel around the bond wires is assumed to not provide a significant heat conduction path.

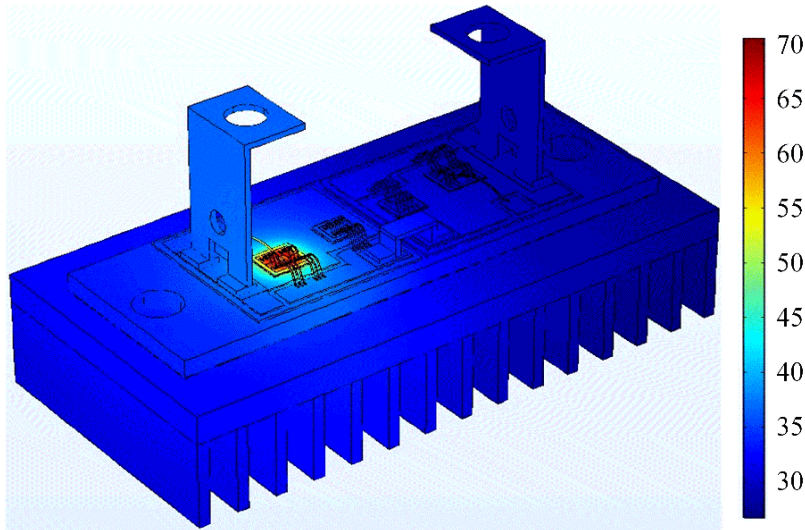


Fig. 3.14. The thermal distribution of the full FEA model with a heat sink model

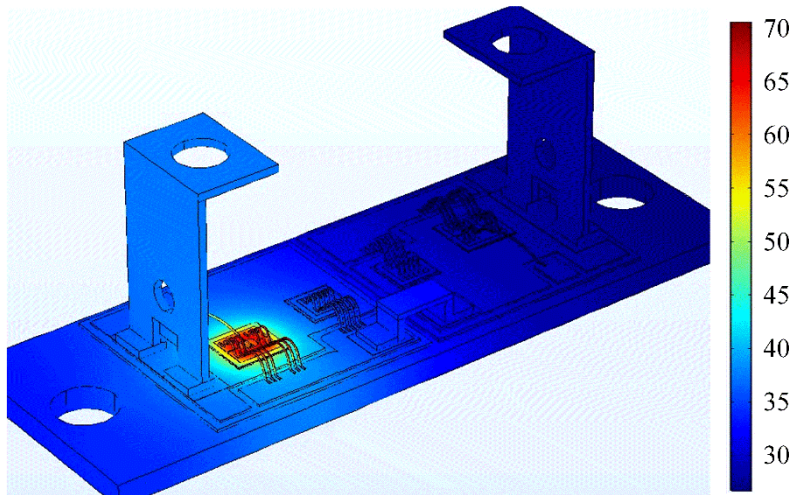


Fig. 3.15. The thermal distribution of the full FEA model without heat sink

The focus of interest is on the thermal distribution of the IGBT chip itself. Therefore, Fig. 3.17 shows the detail thermal distribution of the IGBT chip with the bond wires hidden. The current flows through the IGBT chip from the bottom surface (collector) to the upper surface (emitter), and then through the bond wires to the copper layer connected with terminals. Because the gate is situated at the center of the chip, the current density in the chip exhibits a circular distribution, leading to a corresponding circular distribution of temperature. Additionally, the current density of the chip area connected with bond wires is significantly higher than other areas within the chip, resulting in concentrated power loss on the area of the chip soldered with bond wires. Therefore, the highest temperature of the chip appears in the chip around the bond wires' connection. Considering the physical space, the spaces between the bond wires can be promising locations for the installation of FBG sensors to detect the maximum temperature.

In Chapter 4, the experimental setup will be discussed, along with several examples of

the thermal distribution of the IGBT chip obtained under different operating conditions. Comparisons of these results will be presented in Chapter 4.6 and the simulated thermal distribution is found to fit the experiment result very well.

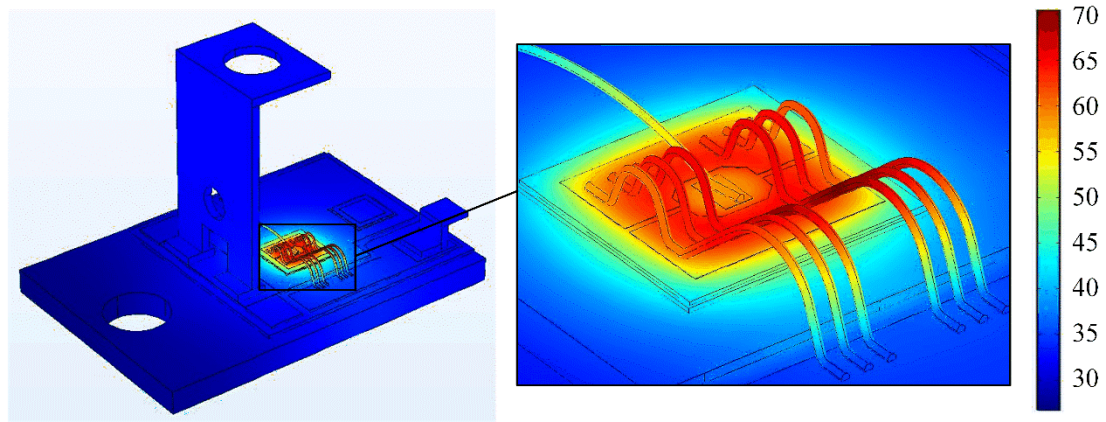


Fig. 3.16. The thermal distribution of the half FEA model

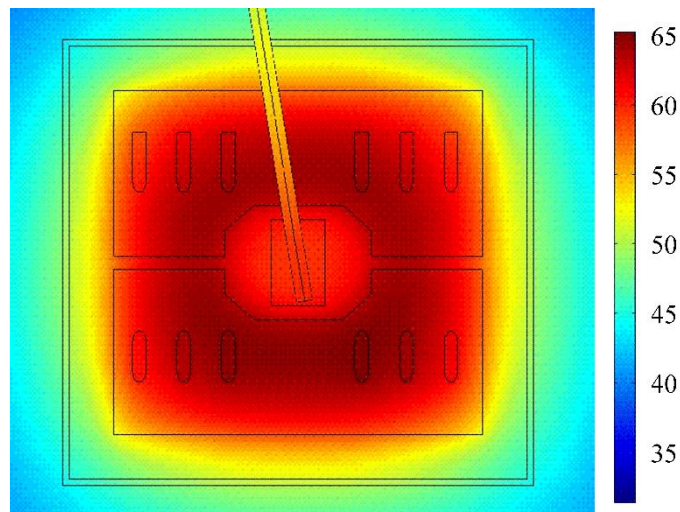


Fig. 3.17. The thermal distribution of the IGBT chip

It is noted that this thermal boundary setting corresponds to the operating condition of the heat sink fan at maximum power (at a rated drive voltage of 24 V). When the fan speed is reduced, resulting in a decrease in the heat dissipation capacity of the heat sink, the device's junction temperature will rise. In the simulation work in Chapter 5.4, the heat transfer coefficient of the baseplate is adjusted to a smaller value to obtain a higher junction temperature for verification. In the experiment in Chapter 7.2, the fan was turned off to measure the highest temperature for verification, with the test results indicating a junction temperature of approximately 150°C.

3.6 Summary

This chapter details the development of a precise FEA model for the IGBT power

module. Initially, the layer structure of the IGBT power module is presented, and the geometry dimensions are determined using direct measurements with calipers and indirect calculations based on cross-section photos. Material thermal properties are established based on available literature and analysis of the IGBT model's thermal circuit to ensure alignment with the performance outlined in the datasheet. It is found that the ceramic layer of the IGBT power module plays an important role in the heat dissipation in the time range of seconds while the IGBT chip and its adjacent solder layer determine the fluctuation of junction temperature at the millisecond level.

Next, the FEM model of the IGBT power module is constructed and meshed. However, the complexity of the simulation model resulted in a large amount of calculation and lead to the failure of electro-thermal simulation due to lack of memory in the computer used. Therefore, the FEA model was simplified, and reasonable electrical and thermal boundaries were assigned. The thermal distribution of the chip remained unaffected by adjustments to the thermal model boundaries.

Thermal simulations of the IGBT power module were subsequently conducted to identify feasible FBG sensor installation positions. The chip displayed a circular temperature distribution, with the highest temperature observed near the bond wire connection. Considering physical space limitations, the spaces between the bond wires were identified as promising FBG sensor installation locations to detect maximum temperatures.

Chapter 4: Test Rig

This chapter outlines the purpose built experimental test-rig used in this research. It aims to provide details of the built test-rig and the associated tools for the experimental work conducted throughout the research.

4.1 FBG thermal sensing system

The section focuses on the FBG thermal sensing system used in the study, which includes the in-situ FBG temperature sensors for thermal monitoring and the commercial interrogation system employed during the PhD research.

4.1.1 FBG temperature sensor design and packaging

The FBG sensor is a type of distributed Bragg reflector etched in an optical fibre that reflects a particular light wavelength and transmits all others [101]. A typical structure of the standard off-the-shelf FBG sensor is shown in Fig. 4.1 [21]. The FBG head comprises a short segment consisting of several gratings imprinted within the fibre core, which is enveloped by the cladding layer and then protected by the coating layer. Due to the lower refractive index of the cladding layer compared to the core, the light is bound to propagate within the fibre core [101].

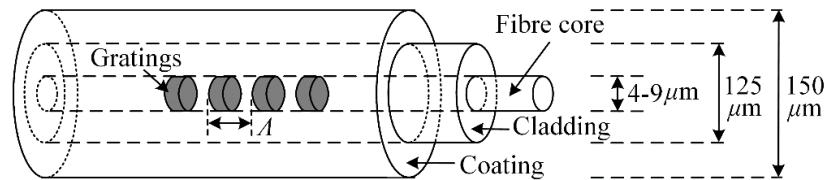


Fig. 4.1. Typical structure of the FBG sensor

Specifications for the sensors used in the study including dimensions, centre wavelength range, fibre and coating type, and probe connector type, need to be identified. Table 4.1 lists the specifications provided to the manufacturer for the standard FBG sensors employed in the research. The standard FBG's centre wavelength range is determined based on the interrogator unit's broadband light source range. The study uses a single-mode Polyimide SMF-28e fibre, which can withstand continuous temperatures of up to $\approx 300^\circ\text{C}$ [124], as the fibre type. The Polyimide fibre is available as either a standard SMF or a bend-insensitive SMF, with the latter preferred for this application due to its design for small bending radii and lower bending loss. A layer of Polyamide coats the fibre to increase its mechanical strength. The FC/APC connector type is recognised as the optimal choice for FBG sensing due to low return losses, and is used in the research here, consistent with the

interrogator unit. A sketch of a single FBG probe is presented in Fig. 4.2 (Fig. 2.3), and Fig. 4.3 provides an image of a packaged FBG sensor [125].

Table 4.1. Dimensions and properties of the FBG sensor

FBGs centre wavelengths	1528-1568	nm
FBG length	1, 3, 5	mm
Refractivity	> 80%	%
Bandwidth	< 0.3	nm
Connector type	FC/APC	--
Fibre length	Specified on drawing	m
Fibre type	Polyimide SMF-28e (standard – bent sensitive)	--
Recoating	Polyimide	--
Temperature range	Up to 250 °C	°C

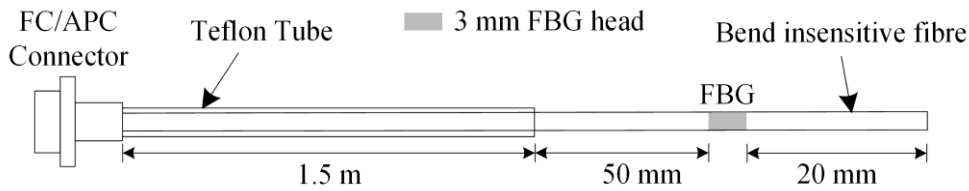


Fig. 4.2. Sketch of a single FBG probe

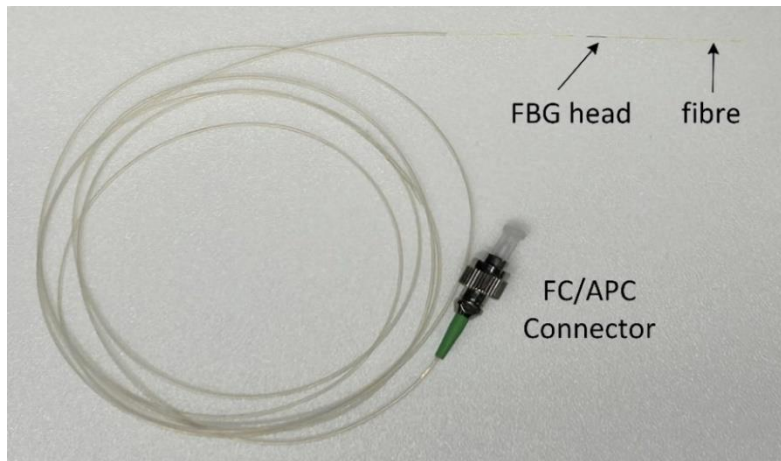


Fig. 4.3. Photograph of FBG packaged temperature sensor [125]

4.1.2 Interrogation

In this research, the SmartScan 04 interrogator unit manufactured by Smart Fibres Ltd is employed, as shown in Fig. 4.4(a). Smart Fibres Ltd specializes in measurement systems based on FBG technology. The SmartScan 04 unit, is chosen for its high resolution (< 1pm wavelength shift) and a maximum sampling frequency of 25 kHz for dynamic measurement

of FBG sensors, and is a compact and robust interrogator [107]. The specifications of the interrogator are detailed in Table 4.2 [107]. As depicted in Fig. 4.4(b), the SmartScan interrogator operates on the wavelength division multiplexing technique, which is explained in Chapter 2, Section 2.3.3. Four channels, labelled CH1, CH2, CH3, and CH4 in Fig. 4.4(a), are available for the SmartScan interrogator, each of which is capable of running up to 16 FBGs imprinted in a single strand of single-mode optical fibre simultaneously.

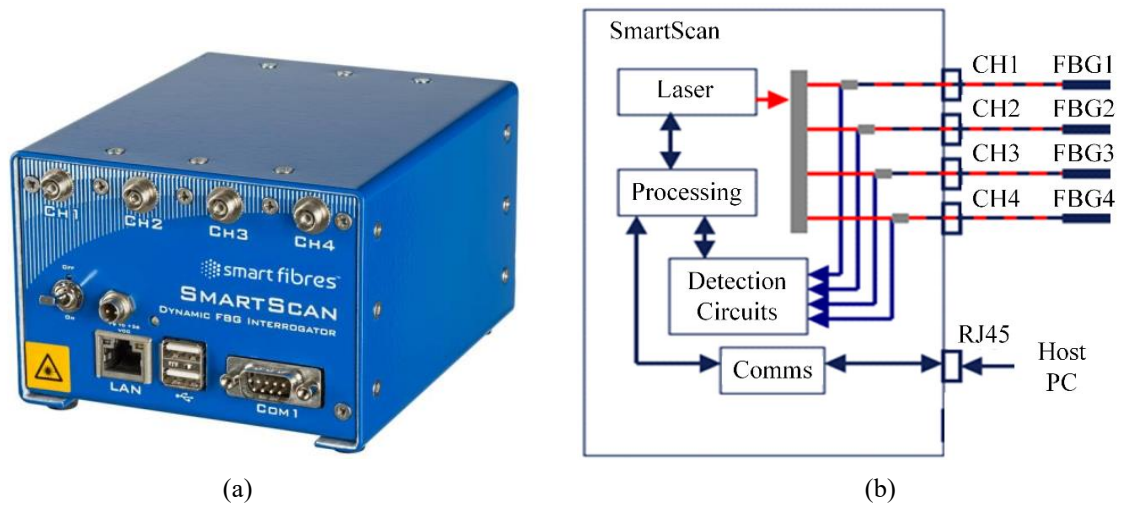


Fig. 4.4. System diagram of FBG sensor interrogation. (a) Photography of the SmartScan interrogator. (b) SmartScan interrogator system diagram

Table 4.2 SmartScan interrogator specifications [107]

Wavelength range	40 nm (1528-1568 nm)
Number of optical channels	4
Maximum number of sensors	16
Scan frequency (all sensors simultaneously)	2.5 kHz
Maximum scan frequency (with reduced wavelength range)	25 kHz
Bragg grating full width half maximum	Minimum > 0.2nm, > 0.5nm recommended
Wavelength stability	< 5 pm over operating temperature range
Resolution	< 1 pm
Optical connector	FC/APC
Operating temperature	-15 to +55°C
Dimensions	140×115×85 mm
Data connector	RJ45 standard

The interrogator can: excite the laser to the optical fibre connected; receive the reflected light from the sensor; decode the received light wavelength; transfer the resulting data to a computer for visualisation and recording [107]. The recorded wavelength can then be translated into a temperature value using the calibrated wavelength-to-temperature (λ - T) characteristic of the FBG sensor. The calibration of the FBG sensor's λ - T characteristic is necessary and discussed in Section 5.2. Additionally, the interrogator unit is equipped with an optional data logging connector that can be used to connect a USB memory device for storing large data sets.

4.1.3 SmartSoft

The SmartScan interrogator unit is accompanied by SmartSoft, a LabVIEW based software routine that facilitates the operation of the device. SmartSoft has a customised interface window and is utilised for configuring the interrogator and the connected FBGs, as well as for processing acquired data to meet various sensing requirements [107]. The interface windows contain several settings for the setup of the interrogation system and the interrogated FBGs. In this regard, the subsequent paragraphs and figures explain the process of setting up and acquiring data from four FBG sensor comprising one FBG head each.

To begin with, four FBG sensors are connected to the four channels of the SmartScan respectively using the FC/APC connectors. The SmartScan is connected to a computer that runs SmartSoft, which enables the initialisation of the SmartScan and communication between the SmartScan and the four FBG sensors. Fig. 4.5 displays the instrumentation setup window in SmartSoft that was employed to set up the connected FBGs, the data acquisition system, and the processing system, as well as the reflected light spectrums from the four channels.

The SmartScan acquisition rate can be adjusted based on the number of activated optical channels and the number of FBGs per channel, which is set to a desired value within the specifications (the first green box from the left in Fig. 4.5). This configuration enables the adjustment of the active light wavelength range sent to the optical fibre containing the FBG sensors, thereby allowing the tuning of the scan cycle time (the second green box from the left in Fig. 4.5). The cycle time refers to the time taken to complete one scan of the light sent to the FBGs and received by the detector circuit. For example, a single FBG probe with λ_B at 1550 nm can only be illuminated with a maximum light range of 3 nm to function as a thermal sensor. Thus, activating a 3 nm range of the broadband light source (1548.5 –

1551.5 nm) will reduce the cycle time required to scan this light range (3 nm) as compared to the time required to scan 40 nm of the whole light range of the broadband source. Table 4.3 demonstrates the possible scan rates, the associated activated light ranges for SmartScan, and the temperature ranges corresponding to the activated bandwidths [107].

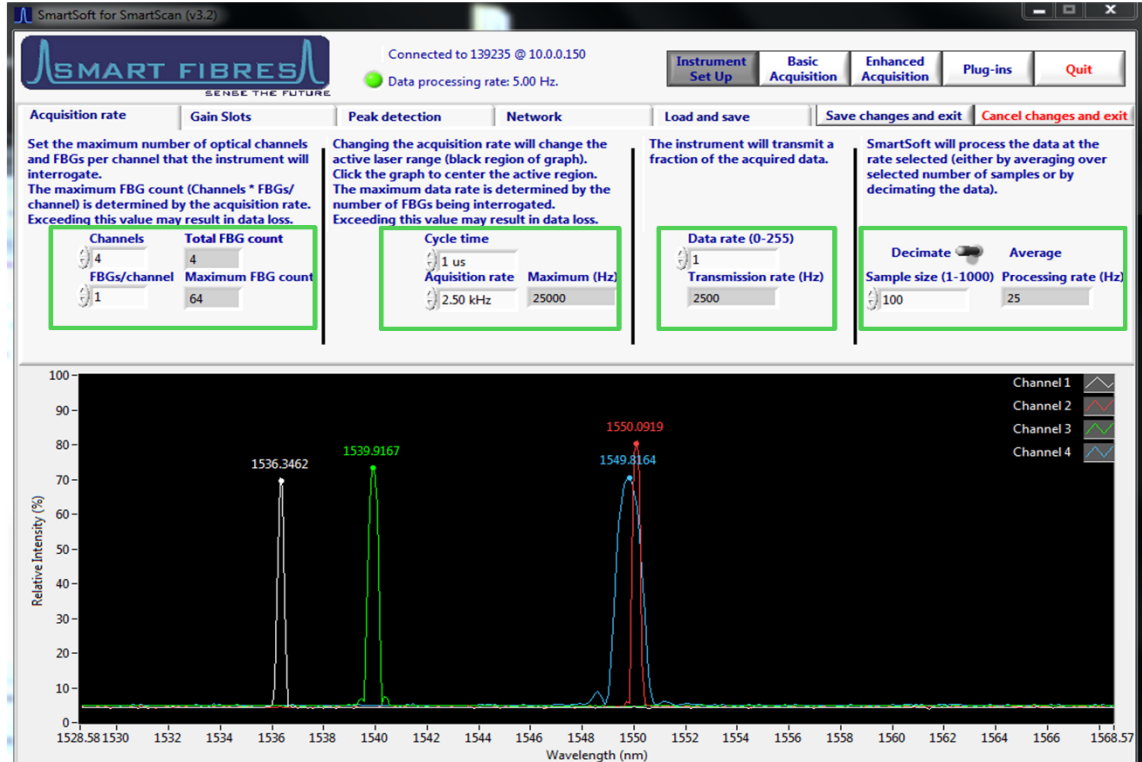


Fig. 4.5. SmartSoft instrumentation window interface

Table 4.3. SmartScan multiple scan rate [107]

Scan rate (kHz)	Activated bandwidth (nm)	Corresponding temperature range (°C)
2.5	40	3200
5	20	1600
10	10	800
20	5	400
25	4	320

The rate of data processing by SmartSoft is adjustable and can be achieved by either changing the transmission rate (the rate of transmitting data from the SmartScan to the PC) or by altering the processing sampling size (the third and fourth green box from the left in Fig. 4.5, respectively). Typically, all the acquired data is transmitted to the PC for processing. However, it may be necessary to slow the transmission rate on a slow network connection or because the host PC cannot process the data quickly enough. The processing

sampling size can be set with a number x , resulting in every x^{th} transmitted data point being processed. Fig. 4.5 shows four peaks with numbers displayed at their respective tops. Each peak represents the reflected λ_B from one FBG sensor. The numbers represent the determined peak λ_B for each FBG head by SmartSoft.

Once the FBGs, acquisition and processing systems are set up, the sensor measurements type and units can be configured, and real-time measurements can be viewed and recorded. For measurements other than the reflected wavelength, such as strain or temperature, a number of coefficients are required to convert the measured wavelength shift to the physical quantity being measured. These coefficients are typically obtained through calibration tests, as explained in Section 4.2. The final setting of the FBG sensors is shown in Fig. 4.6, with the left table displaying the available FBG sensors per channel corresponding to the settings made in the instrumentation setup window, and the right-hand table showing the configured sensors that can be monitored online and recorded. The first four arrows (named CH1 to CH4) indicate the instantaneous monitored peak λ_B for each FBG, while the 5th arrow represent the measured temperature based on the entered coefficients for the wavelength shift-temperature conversion. The inset figure shows the function definition window to convert the measured wavelength to temperature or mechanical stress.

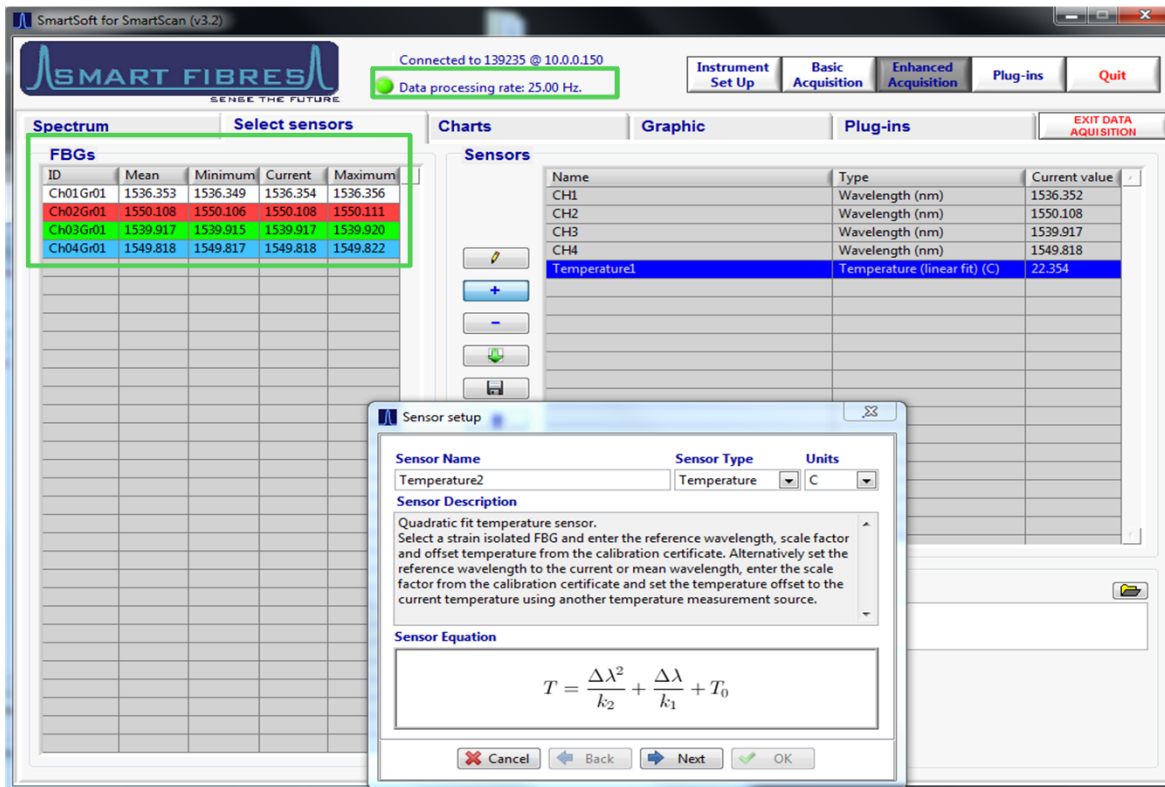


Fig. 4.6. Enhanced acquisition – Sensors' tab

4.2 FBG sensor thermal calibration test-rig

In order to obtain temperature readings from the reflected λ_B of the FBG sensors, it is necessary to perform a thermal calibration test to determine the optimal temperature-wavelength fit curve for each FBG. During this test, the FBG sensors are exposed to controlled, steady-state thermal excitation levels and their reflected λ_B s are monitored and recorded for each thermal level. The FBGs under calibration could be single or an array, unpackaged or packaged, and embedded or free within a coil or machine structure.

To achieve the required controlled thermal excitation, an industrial thermal chamber (type TMS Europe SNOL 60/300 LFN) shown as Fig. 4.7 with a temperature control accuracy of $\pm 0.5^\circ\text{C}$ and a maximum temperature of 300°C was utilized. The temperature references were measured by the thermal chamber proprietary thermal sensor.



Fig. 4.7. The thermal chamber

The thermal calibration test was conducted by placing the FBG sensor in the thermal chamber and exposing it to incremental set point temperatures up to the maximum temperature of the IGBT power module for embedding. The temperature was regulated by the chamber controller in a rising sequence of a certain temperature step, which was deemed sufficient to achieve satisfactory characterization of the sensor behaviour. At each step, the temperature was held constant for a sufficient period to ensure thermal equilibrium before thermal measurements were taken. The FBG reflected wavelength and the chamber temperature were recorded at each evaluated thermal equilibrium set point in the investigated temperature range. The recorded data was then used to calculate the temperature-wavelength conversion fit curve. Based on a comparison study of different

curve fit models, such as linear fit, 2nd, 3rd, and 4th order polynomial fits, the polynomial quadratic fit curve was found to be the most appropriate fit for the FBG thermal sensors in this type of application and was therefore used in this research.

Although attempts were made to ensure thermal equilibrium during the calibration process, it is possible that the thermal chamber's inner space had a thermal gradient originating from the heat source, proprietary thermal sensor, and the calibrated FBG sensor. This thermal gradient serves as a potential source of calibration error. The calibration is supposed to be more accurate by putting high precision temperature sensor next to the FBG sensor.

4.3 Main test rig and components

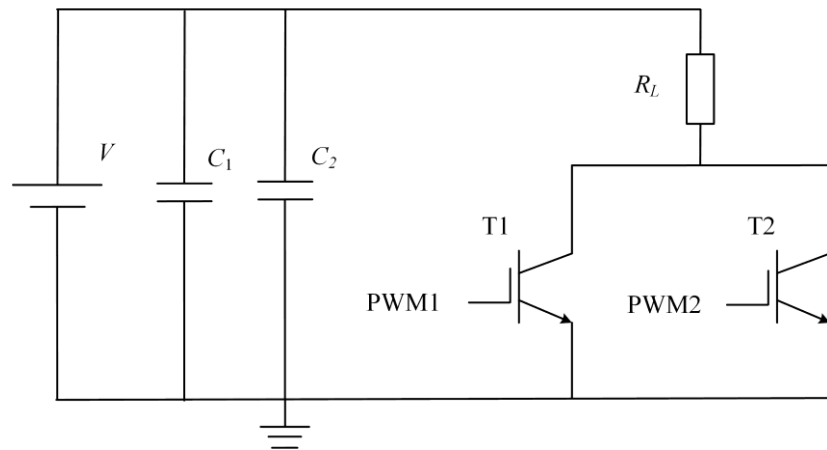
A test rig was built to provide up to rated DC current (50 A DC) to heat the commercial IGBT test module. The circuit schematic is shown in Fig. 4.8 (a). This circuit mainly consisted of a DC power source, a resistance load, a capacitor filter and two IGBTs. The test rig is shown in Fig. 4.8 (b). The control timing diagram of the two IGBTs is shown in Fig. 4.9.

The DC power source is a programmable precision high power DC power supply, which is shown in Fig. 4.10. Its rated power is 5 kW and the maximum output current is 50 A. Its typical output voltage rise time is 10 ms from 10 V up to 50 V with full load, and the typical voltage fall time is also 10 ms.

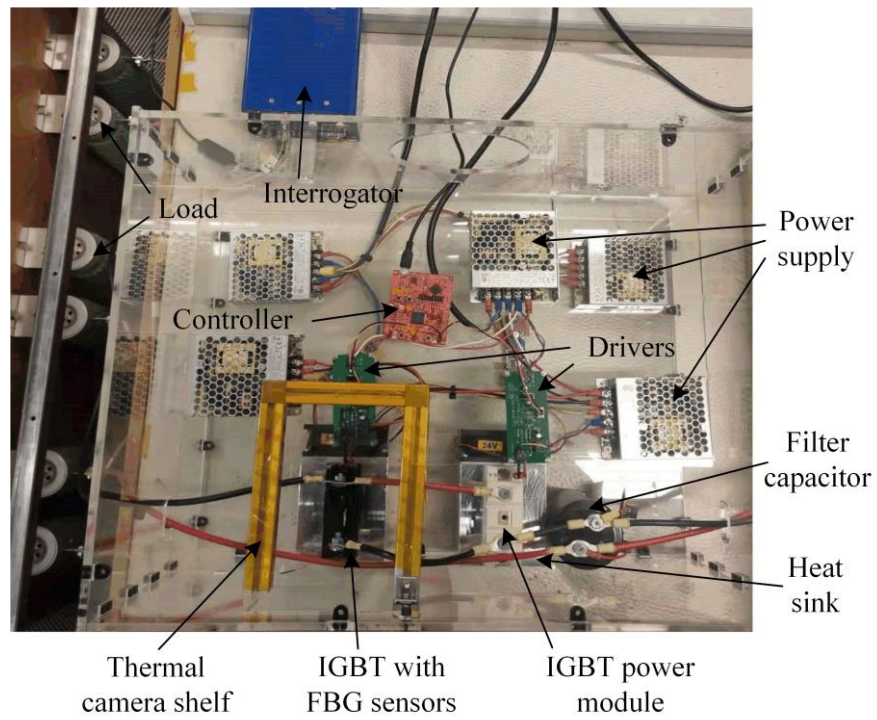
The RC filter consists of two capacitors: C1 is an Aluminium electrolytic capacitor and the capacitance is 4700 μF ; C2 is a ceramic capacitor and the capacitance is 1 μF . Both the two capacitors have rated voltage of 100 V to ensure the security of the experiment.

The resistance load consists of six ripple resistors connected in series and parallel, and the total resistance is 0.67 Ω and rated power is 7.5 kW.

The IGBT power module utilized in this investigation is the Semikron SKM50GB12T4. This module comprises two IGBT chips and two diode chips, and its structure is detailed in chapter 3.3. For the experiments, two IGBT power modules were affixed to two forced air-cooled heat sinks, respectively, with a single chip per power module being used. Specifically, T1 acted as the FBG instrumented chip under test while T2 was designated as the freewheeling circuit as shown in Fig. 4.8. The IGBTs were alternately turned on and off to decrease the voltage pulse caused by the circuit's inductive components when either IGBT was turned off.



(a)



(b)

Fig. 4.8. Test rig. (a) electric circuit diagram, (b) Test rig top view.

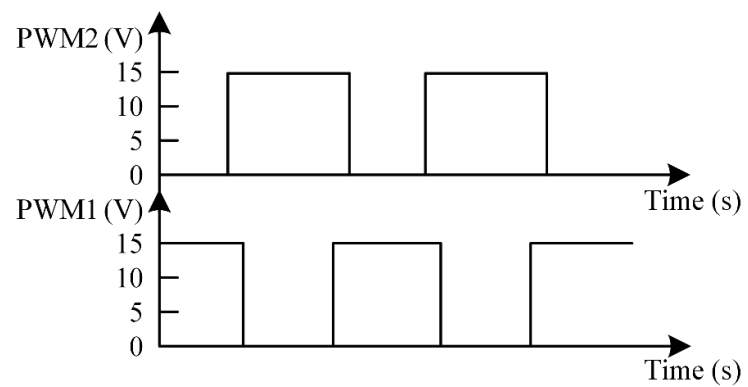


Fig. 4.9. Control timing diagram of the two IGBTs.

The forced air heat sink, illustrated in Fig. 4.11, has a thermal resistance of 0.14 K/W and a DC-powered fan, whose rotation speed can be regulated to modify the heat sink's cooling ability. The control voltage for the fan is rated at 24V DC.



Fig. 4.10. The DC power source.



Fig. 4.11. Forced air cooling heatsink.

A thermal pad was put between each IGBT power module and corresponding heat sink to keep the module-heat-sink contact thermal resistance consistent between tests. The thermal pads used were 0.5 mm thick with a 6 W/(m·K) thermal conductivity.

The IGBT control signal was generated by a Texas instruments MSP430 F5529 microcontroller. It contains everything needed to start developing on a USB enabled MSP430 MCU, including on-board emulation for programming and debugging as well as on-board buttons and LEDs for quick integration of a simple user interface.

The controller was connected with two Si8271 based IGBTs gate drivers. The driver board circuit and the PCB are shown in Fig. 4.12 and Fig. 4.13, respectively.

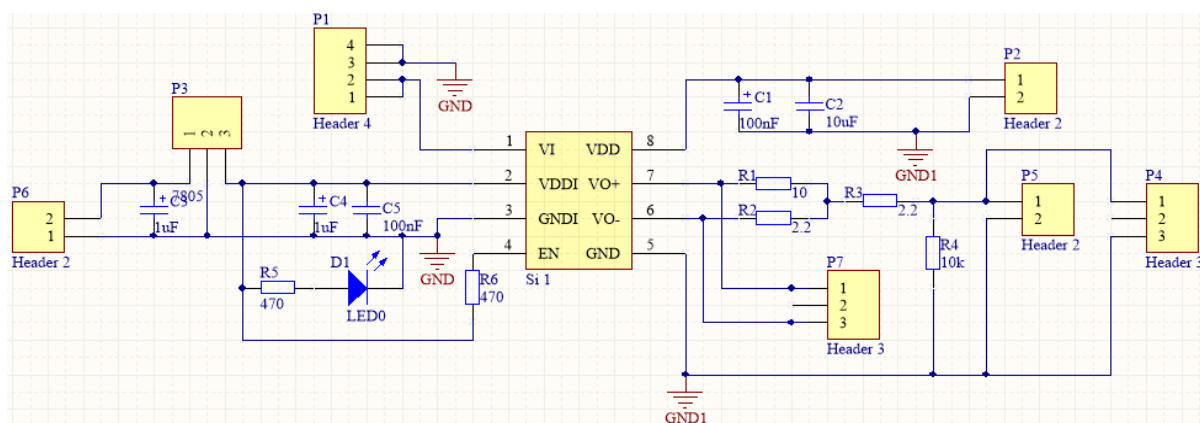


Fig. 4.12. Driver board circuit

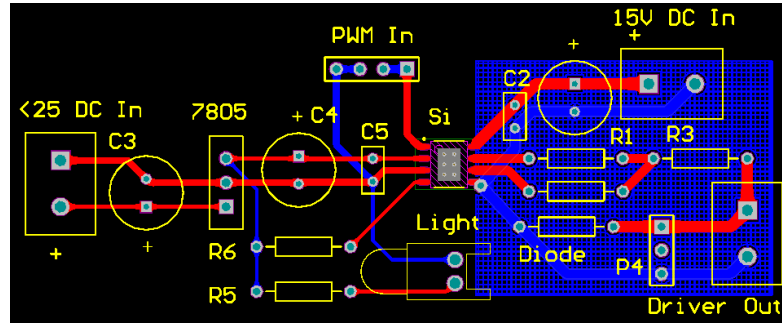


Fig. 4.13. Driver board PCB

Si8271 chip has eight pins as shown in Fig. 4.12. The inner circuit of the Si8271 chip is a push-pull structure and this chip has an isolation function. Pin 1 is the control signal input port. Pin 2 was connected to a 7805 based DC power supply, which provided power to the chip. Pin 8 was also connected to a DC power supply, which offered power to drive the IGBT chip. The voltage of the Pin 8 decided the output voltage level of the driver board, which was the IGBT gate voltage. Pin 3 and Pin 5 both are ground, but they are isolated. Pin 4 is the chip enable port: the chip will work when pin 4 has a high-level voltage (5V), vice versa. Pin 6 and pin 7 are the two output ports of the push-pull circuit. The resistors R_1 and R_2 shown in Fig. 4.12 are chosen as $10\ \Omega$ and $2.2\ \Omega$ resistors respectively. A relatively large resistance connected with pin 7 protects the IGBT from turn-on peak current and charge accumulation. A relatively small resistance connected to pin 6 can accelerate the discharge and reduce the turn off time. The blue mesh shown in Fig. 4.13 is copper clad laminate, which connects with the pin 5 GND.

In this study, a Fluke Ti10 thermal imager was utilized for temperature measurements. The thermal imager has a temperature measurement range of -20°C to $+250^\circ\text{C}$, with a temperature measurement accuracy of $\pm 2^\circ\text{C}$ or 2% (whichever is greater) [126]. It has a minimum focus distance of 15 cm, and a visible light lens of 46 cm, which can be manually adjusted. The thermal imager has an image refresh frequency of 9 Hz, but it cannot record temperature change processes in videos.

To capture the temperature of the IGBT chip surface, the thermal camera was placed on the camera shelf directly above the chip, as shown in Fig. 4.9. However, due to the low emissivity of the IGBT chip surface (with the silver solder layer), it was not possible to obtain an accurate temperature measurement directly. To overcome this issue, the IGBT surface was coated with MOTIP black paint to increase its emissivity. To ensure a homogeneous emissivity and accurate thermal camera temperature readings, 20 coats of paint were applied.

Some key specification of the Equipment of the test rig are listed in the Table 4.4.

Table 4.4. Key Specification of the Equipment used for Experiments.

Equipment	Type	Details
Main power supply	Sorensen SGI	Rated 50A/100V/5kW
Auxiliary power supplies	Switching Power Supply	Rated 2.4A/15V/35W
IGBT	SKM50GB12T4	Rated 50A/1200V
Load	Ripple resistor	0.67Ω/ Rated 9kW
Controller	MSP430 F5529	16-Bit RISC Architecture, up to 25-MHz System Clock
Driver	Si8271 based	Max 60 ns propagation delay
Thermal camera	Fluke Ti10	Accuracy ± 5 °C or 5 %
		Thermal Sensitivity ≤ 0.2 °C at 30 °C
		Temperature Range -20 °C to +250 °C
Interrogator	SmartScan04	Repeatability < 1 pm
		Max. scan freq. 2. kHz
Capacitor	Aluminum electrolytic	4700μF/60V
Heat sink	Forced air cooling	max. air flow 80 m ³ /h

4.4 $V_{CE} - T_j - I_C$ calibration test rig

At present, IGBT on-state voltage (V_{CE}) based junction temperature (T_j) evaluation is a classic method to realize T_j acquisition as reviewed in Chapter 2. V_{CE} is a TSEP that varies with temperature and current (I_C). To obtain an accurate T_j measurement, the relationship between V_{CE} , T_j and I_C must be calibrated beforehand, a process that is discussed in detail in Chapter 7. This V_{CE} -based method is compared to the FBG sensor-based T_j measurement technology in Chapter 7. This section introduces the test setup for calibrating the relationship between V_{CE} , T_j , and I_C .

The circuit diagram used for calibration is shown in Fig. 4.14. The main circuit comprises a DC power supply, a capacitor filter, a resistive load, and three IGBTs. The specific IGBT_DUT is the IGBT concerned with the $V_{CE} - T_j - I_C$ relationship. It was placed inside a digital thermal chamber with a resolution of 0.1°C. The collector-to-emitter voltage ($V_{CE,DUT}$) of the IGBT_DUT was directly measured using a high bandwidth voltage probe with a measurement bandwidth of 20 MHz. The collector current (I_{DUT}) was measured using a current probe with a bandwidth of 10 MHz.

The IGBT gate port was connected to an adjustable DC power supply to ensure the

IGBT_DUT is always on. IGBT_s was connected with the IGBT_DUT in series while the IGBT_p was connected in parallel. A current impulse was generated by the cooperation of the IGBT_s and IGBT_p. The IGBT_p was kept initially on, during which a constant current flowed through it. Later on IGBT_p is turned off, immediately after IGBT_s turned on. Thus the current that flowed through IGBT_p is diverted to IGBT_s. The IGBT_s is kept on for tens of microseconds until I_{DUT} reaches steady state, this on period is required since the inductive component of the power cable limits the change rate of the current. After that, IGBT_s turns off immediately after IGBT_p turns on. Then the current turns back to the parallel IGBT branch. Thus, a current impulse was generated to the IGBT_DUT, and the current flowing through the power supply and the load R_L would never be cut off directly, to avoid voltage impulse that might occur due to the parasitic inductive component within the circuit and load.

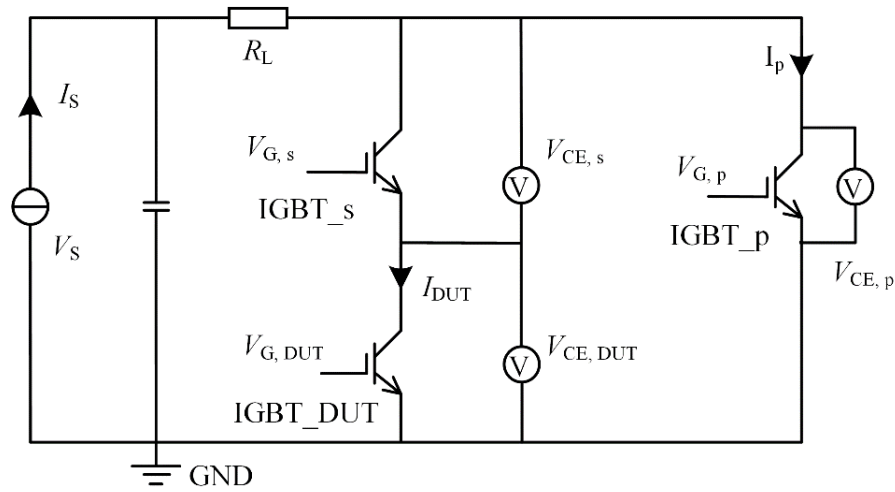


Fig. 4.14. Circuit diagram of the $V_{CE} - T_j - I_C$ relationship calibration test rig

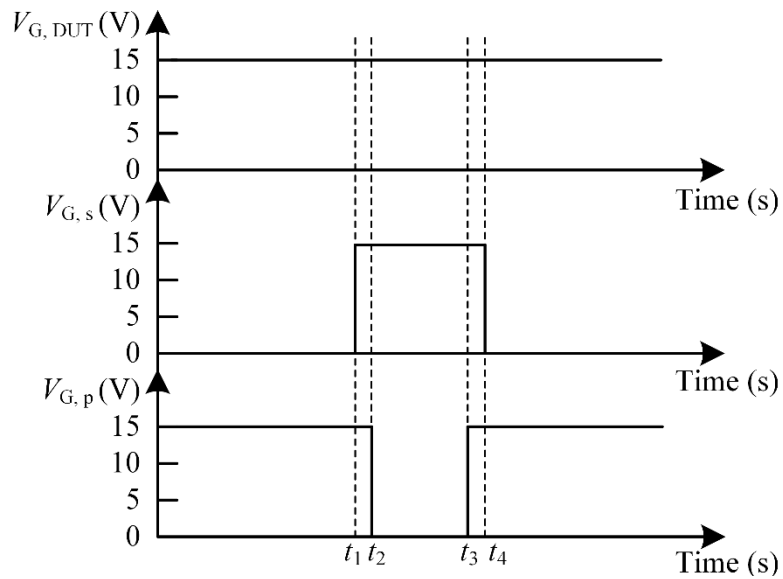


Fig. 4.15. Control timing diagram of the three IGBTs.

To ensure that the IGBT_DUT remains on on-state, the gate port of the IGBT was connected to an DC power supply. The IGBT_s was connected in series with the IGBT_DUT, while the IGBT_p was connected in parallel. By coordinating the operation of the IGBT_s and IGBT_p, a current impulse was generated. The control timing diagram of the three IGBTs is shown in Fig. 4.15. Initially, the IGBT_p remained on, allowing a constant current to flow through it. After a specific amount of time, the IGBT_p turned off, immediately after IGBT_s turned on. Consequently, the current that previously flowed through the IGBT_p is redirected towards the IGBT_s. The IGBT_s remains active for tens of microseconds to ensure that the I_{DUT} reaches steady state. This step was necessary because the inductive component of the power cable limited the rate of current change. Subsequently, the IGBT_s was turned off immediately after IGBT_p turned on, and the current reverted back to the parallel IGBT branch. This process generated a current impulse to the IGBT_DUT, while ensuring that the current flowing through the power supply and the load R_L was never abruptly interrupted. Thus, it was able to prevent voltage impulses that could arise due to parasitic inductive components in the circuit and load.

4.5 Summary

This chapter provided a detailed description of the different test-rig systems, including the FBG sensing system and the additional tools, used to conduct experimental research in this PhD study.

Chapter 5: FBG Sensor Installation and Interfacing Technologies

An FBG sensor can be installed on the surface of the IGBT chip inside an IGBT power module. The FBG sensor has high sensitivity to temperature and mechanical strain excitation as introduced in Section 2.3.1. The high temperature sensitivity of the FBG sensor promises potential of high accuracy in temperature measurement. However, because the thermal measurement is the only physical parameter of interest in this study, the strain sensitivity could cause the sensor readings to be disturbed by the presence of mechanical stress. Therefore, the installation of the FBG sensor needs to be carefully managed to prevent interference from inadvertent mechanical stress and to ensure the accuracy of the temperature measurement. In addition, the gap between the FBG sensor and the IGBT chip cannot be eliminated. The filled interface material provides thermal contact between the sensor and the chip surface; and the quality of the thermal contact is proven to be able to affect the accuracy and the response rate of the thermal sensing.

This chapter explores the installation methods and associated sensing performance features for direct on-chip surface temperature sensing in IGBTs using FBG technology. To this end one thermal paste and three glues with different properties are chosen as interfacing materials for comparison. The feasibility investigation of the interfacing materials includes two steps. Step 1 is to calibrate the performance of the installed FBG sensors under different interfacing materials, to check the interference induced during the installation process. Step 2 is to test the measurement accuracy and response rate of the FBG sensors fixed using different interfacing materials. Corresponding to the two steps, the in-situ calibration requirements of the IGBT installed FBG sensors are examined as a precursor to in-service thermal measurement. The test rig introduced in Section 4.1 is used to perform a range of experiments to characterize the measurement performance of the studied interfacing options in a variety of IGBT operating conditions. A control group of installed FBG sensors without additive interfacing material is also built for comparison.

5.1 Test interface materials and their properties

An ideal interface material is expected to possess infinite thermal conductivity, a glass transition temperature higher than the IGBT's maximum operating temperature, and a suitable viscosity to secure the fibre position.

One thermal paste and three glues were chosen for this study. Their relevant physical properties are shown in Table 5.1. The air as a comparison interfacing material in a control group is also included.

Table 5.1. Interfacing materials and their properties

Glue type	Air	Thermal paste	8329TCM	ES578	TCOR75S
Material	--	silicone-based	epoxy-based	epoxy-based	silicone-based
Color	--	white	Grey	Black	White
Therm. Cond. (W/(m·K))	0.026	5.2	1.4	1	1.8
Curing method	--	--	24 hrs./25°C	10 hrs./100°C	24 hrs./25°C
T_g (°C)	--	--	46	105	--
Hardness	--	--	77D	80D-85D	75A
CTE prior T_g (ppm/°C)	--	--	71	45	--
CTE after T_g (ppm/°C)	--	--	131	--	--

The thermal conductivity of the air is 0.026 W/(m·K) while the thermal conductivities of the thermal paste and the glues range from 1 to 5.2 W/(m·K). The thermal conductivities of the solid interface materials (thermal paste and glues) are much larger than that of the air.

The glues were deliberately chosen to have different physical properties including curing temperature, glass transition temperature (T_g), and hardness to provide a meaningful comparative analysis.

The T_g is one of the most important parameters of a glue, especially in applications at high temperature. As an amorphous material, the glue will experience a gradual and reversible transition from a hard and relatively brittle "glassy" state into a viscous or rubbery state, as the temperature is increased. The T_g of the glue is characterized by a temperature, over which this glass transition occurs. The glue transits from a viscous or rubbery state into the glass state when the temperature decreases from over to below T_g . As the glue transits from one state to the other, the glue's residual strain excerpted over the FBG head changes, potentially altering the performance of the FBG sensor. The first glue listed in Table I, the 8329TCM, has a low T_g (46°C) and low cure temperature. In contrast, the ES578 has a much higher T_g (105°C) and cure temperature (100°C). Finally, the TCOR75S, is a silicone-based glue, which is quite soft after it cures. No T_g is provided by the manufacturer for the silicone-based glue. However, cured silicone rubber has typical T_g values around -20°C, suggesting that under normal working temperature, the silicone-based

glue will be consistently operating on the rubbery state.

The CTE of glue is also a significant parameter in this study. Compared with the CTE of the fibre (0.55 ppm/°C), all the three glues have relatively larger CTEs. Therefore, materials CTE mismatch may produce additional stress on the FBG during temperature fluctuation, which will be verified and demonstrated in Section 5.5.

As the FBG sensors were intended to be installed on the surface of the IGBT chip, the commercial IGBT power modules purchased for the experiments were found to be filled with silicone gel, covering both the IGBT chip and bond wires. The removal of the silicone gel was necessary as a preparation step before testing. For this purpose, a chemical silicone solvent, Dowsil DS-2025, was employed in this research to dissolve the silicone gel inside the commercial IGBT power modules. In the chemical laboratory, the IGBT modules were positioned upside down in a corrosion-resistant glass tank after the removal of the module case. Subsequently, the solvent was introduced into the tank to fully submerge the entire IGBT device. Over time, the silicone gel gradually dissolved in the dissolving agent, facilitated by the effect of gravity due to the inverted position of the device. After allowing the process to proceed undisturbed for a period of two weeks, the original silicone coating of the IGBT device was completely removed. For the practical implementation of the proposed scheme utilizing FBG sensors to measure the IGBT junction temperature, the installation of FBG sensors on the chip surface is necessary during the packaging process of the IGBT power modules, preceding the injection of the silicone gel during manufacturing.

5.2 Calibration of the Free FBG Sensors

Fig. 5.1 (also shown in Fig. 4.2) displays the configuration of the FBG sensors utilized in this study. The FBG sensor head is 3 mm in length and is imprinted in a single mode polyamide coated fibre. The fibre is protected by a 1.5 m Teflon tube. The central Bragg wavelengths of all FBG sensors used in this study were around 1539.9 nm (± 0.2 nm) at 30°C.

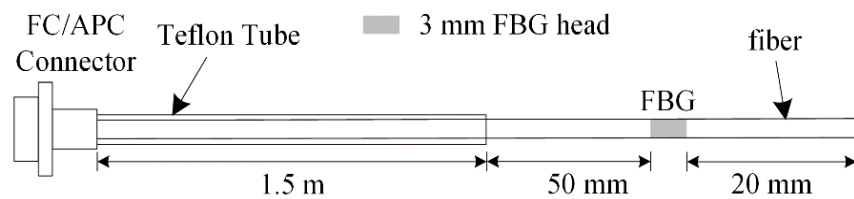


Fig. 5.1. Schematic representation of the used FBG sensors.

Before installation, the free FBG sensors were calibrated to obtain the FBG temperature-wavelength (T - λ) relationships using the test rig introduced in Section 4.2. Each FBG head was placed in a ceramic capillary connected to a stainless-steel plate using Kapton tape to ensure calibration in a mechanically stress-free environment. The steel plate-FBG sensor set was placed in a digitally controlled thermal chamber where the FBG heads underwent four identical thermal cycles. In each cycle, the temperature was initially increased from ambient (about 30 °C) to 40 °C, followed by uniform 20 °C increments until a temperature of 160 °C was reached. Due to the fibre confinement and controlled temperature inside the thermal chamber, ambient temperature did not play an active role during sensor calibration. At each temperature increment, once thermal equilibrium was reached, the peak wavelength (λ_B) recorded by the interrogator unit was recorded. For each FBG, the average value of λ_B for the four cycles was calculated at each temperature.

Fig. 5.2 depicts an example of the measured and averaged calibration results for an FBG sensor. The inset in the figure shows the typical deviation of the measured wavelength λ_B of the four thermal cycles at 120°C. The minor variations in the calibration results are attributed to calibration errors, which include shifts caused by the calibration units such as the thermal chamber and the inherent errors of the FBG sensors and interrogator unit. The maximum standard deviation (SD) of the four cycles at seven measurement temperatures was 2.6 pm. The averaged data displays good linearity with an R-square of 0.9993. The T - λ curved fitted equation is used to calculate the temperature from the measured wavelength. Comparable deviation margins were observed for all FBG sensors under calibration.

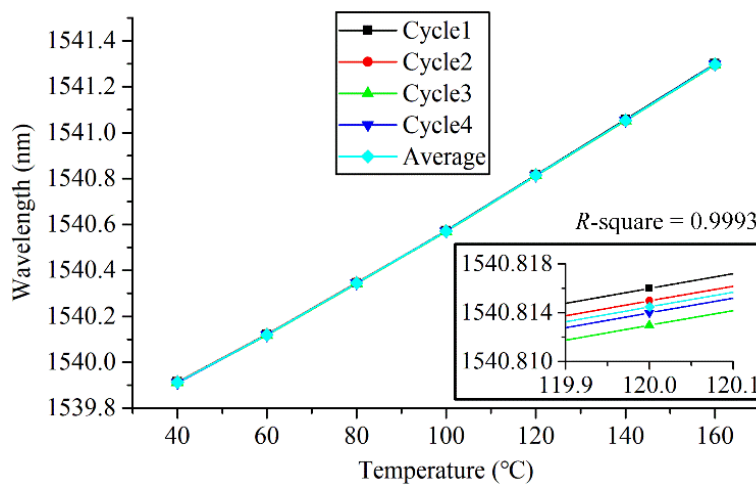


Fig. 5.2. Wavelength-temperature characteristic for the free FBG sensor. with an inset showing the typical deviation of the measured wavelength λ_B of the four thermal cycles at 120 °C.

Based on the calibration data, the sensitivity of the utilized FBG was calculated as $11.7 \text{ pm}/^{\circ}\text{C}$. The resolution of the temperature measurement is generally limited by the resolution of the interrogator unit employed. For the interrogator/FBG combination used, a resolution of 1 pm is achieved, equivalent to 0.08°C . This is more than sufficient for practical thermal monitoring of power electronic devices, where thermal changes in the order of one degree or higher are typically monitored.

5.3 FBG Sensor Installation

The IGBT die of the Semikron SKM50GB12T4 module considered in this work is shown in Fig. 5.3. The length, width, and thickness of the IGBT chip are 7.2 mm , 6.8 mm , and 0.10 mm , respectively. A single bond wire connects the gate to the control port of the IGBT power module. The remaining 6 bond wires are bonded on the solder layer on the chip top surface, which acts as the IGBT emitter.

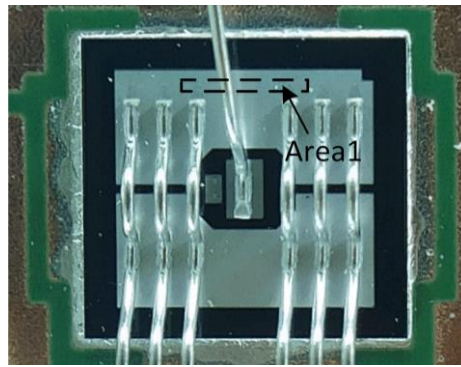


Fig. 5.3. The IGBT chip and the bond wires

Sensor installation was performed manually. To facilitate handling and installation of the FBG sensor in a relatively spacious area of the chip surface, area 1 as shown in Fig. 5.3, was chosen. Five cases were formed: one ‘air-interface’ case, one ‘paste-interface’ case, and three ‘glue-interface’ cases. For each case, one FBG sensor was attached on the area 1 of a chip.

The considered practical installation scenarios for the ‘air-interface’ case, the ‘paste-interface’, and the ‘glue-interface’ cases are shown in Fig. 5.4 (a) (b) (c), respectively.

Fig. 5.4 (a) shows the ‘air-interface’ installation case: the FBG head was placed in area 1 while the left side of the fibre, which was connected to the interrogator, was anchored using glue. The fixed point was 15 mm away from the FBG head, to minimize any mechanical disturbance to the measurements. The end of the fibre was loosely inserted in a fixed position Teflon capillary, to retain the fibre position while avoiding introduction of undesirable mechanical stress. Teflon was chosen due to its mechanical and dielectric

properties, combined with flexibility and extreme resistance to harsh environments. The Teflon capillaries were chosen with suitable inner diameter and wall thickness to minimize the gap between the fibre and the IGBT chip surface, to help achieve a more effective thermal sensing performance of the FBG sensor embedded on the chip surface. These dimensions also allowed the fibre to keep straight to avoid any bend in the shape which can result in mechanical stress to the sensor head. General parameters of the capillary are shown in Table 5.2

Fig. 5.4 (b) shows the ‘paste-interface’ installation case. This retains the installation characteristics of the ‘air-interface’ scenario with a significant difference: the thermal paste was used to ensure a soft, solid bond between the sensing head and the IGBT chip surface to provide improved heat conduction between the two.

Fig. 5.4 (c) illustrates the 'glue-interface' scenarios. To ensure optimal thermal contact between the sensor and the sensed surface, the installation of each FBG sensor was carried out with great care to minimize the distance between the fibre and the IGBT chip surface. To accomplish this, glue was used to fill any gaps. Initially, a small amount of glue was applied to area 1 before placing the fibre on this area. Kapton tape was then affixed to the two sides of the FBG sensor head (around the black area illustrated in Fig. 5.3) to secure the fibre to the IGBT chip surface. Subsequently, glue was applied to the entire FBG sensor head to cover the fibre, and the glue was cured according to the manufacturer's instructions. For the IGBTs with 8329TCM and TCOR75S, the curing process was carried out at room temperature for 24 hours, while for the IGBT with ES578, it was placed inside a thermal chamber at 100 °C for 10 hours. After the glue had cured, the Kapton tape around the black area was removed. The aim of the installation process was to minimize any gap between the fibre and the chip surface to promote efficient heat transfer into the sensor.

Table 5.2. Dimensions and properties of Teflon capillary

Dimension/Properties	Value/Unit
Inner diameter	0.6 mm
Outer diameter	0.8 mm
Wall thickness	0.1 mm
Operating temperature	250 °C
Melting point temperature	350 °C
Thermal conductivity	0.173 W/(m·k)
Hardness, R scale	R-126

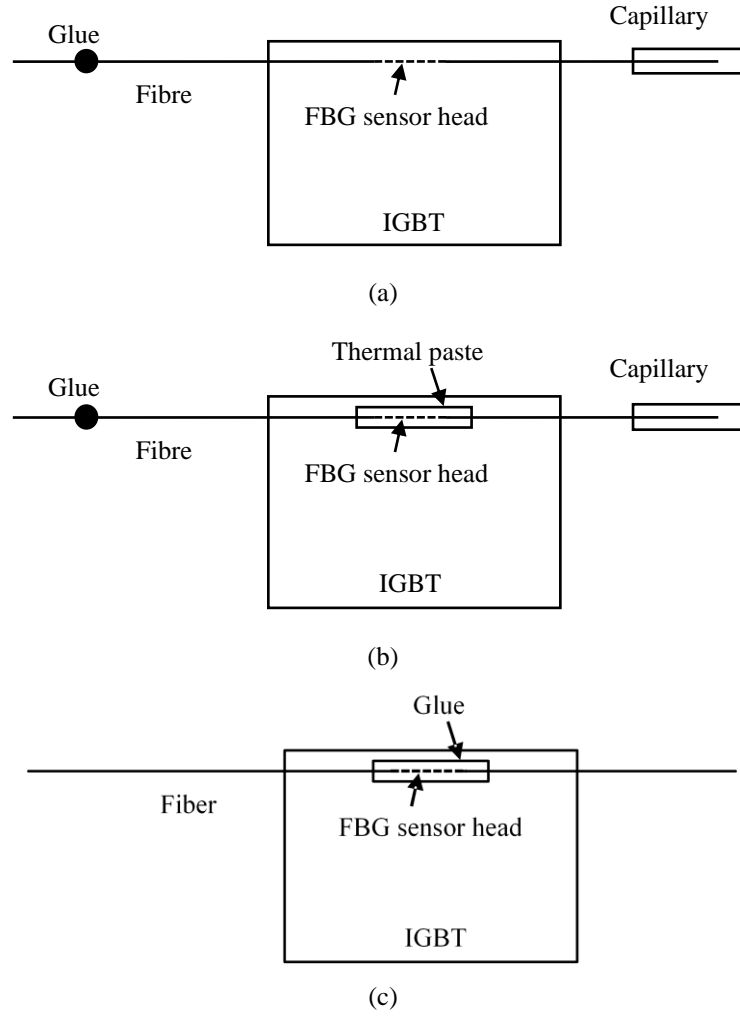


Fig. 5.4. Schematic representation of the installed FBG for the three interface options assessed: (a) 'air-interface', (b) 'paste-interface', (c) 'glue-interface'.

5.4 Simulation of interface thermal conductivity effect on sensing performance

The detail of the IGBT FEA model is illustrated in Section 3. In this section, the FBG sensor and interface materials are modelled and added to the IGBT model based on the installation schematic demonstrated in Section 5.3. The sensing performance of the FBG sensor is simulated under the condition of the interface materials with different thermal conductivities. Transient response and stationary response are introduced separately.

A single, homogeneous material (silica glass) is considered for the entire fibre for simplicity. A 3mm section of the fibre, shown in light blue in Fig. 5.5, represents the FBG sensing head. A $75\mu\text{m}$ gap between the IGBT top surface and the bottom of the optical fibre is assumed in the simulations. A box structure, centered along the IGBT length and surrounding the FBG sensing head (see Fig. 5.5), is used to emulate the thermal interface

material between the IGBT surface and the FBG sensing head.

The thermal conductivities of all interface material candidates are shown in Table 5.1. The thermal conductivity of the air is $0.026 \text{ W/(m}\cdot\text{K)}$ while the thermal paste and the glues have close thermal conductivity in the range from $1 \text{ W/(m}\cdot\text{K)}$ to $5.2 \text{ W/(m}\cdot\text{K)}$. Therefore, in this simulation section, a new name ‘solid-interface’ is used to represent the thermal paste and the glues to be simplification since the study focus on the effect of various thermal conductivities while the precise kind of material is taken to not matter.

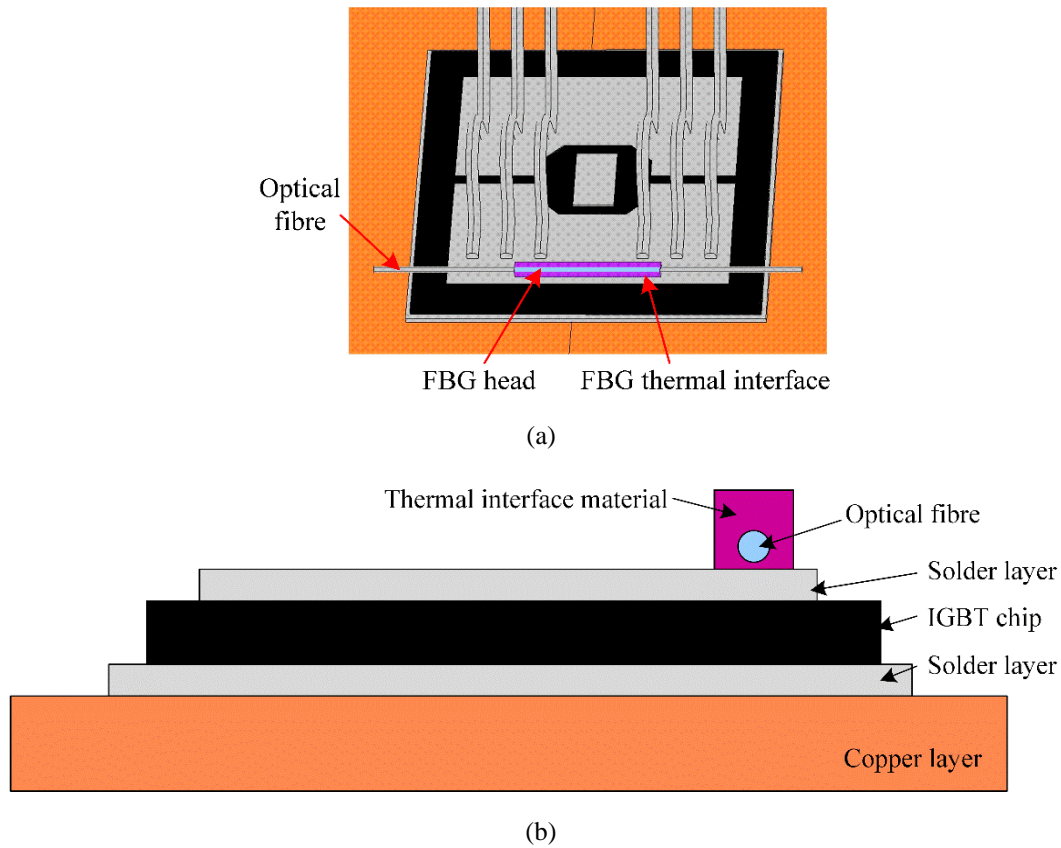


Fig. 5.5. Instrumented IGBT module FE model geometry. (a) Top view. (b) Cross-section view.

The average surface temperature of the area in the top solder layer, where the thermal interface is seated, is used as the reference temperature in the comparisons. Meanwhile, the average temperature of the 3 mm fibre section, used to emulate the FBG sensing head, is assumed as the temperature reported by the FBG sensor.

The heat transfer coefficient (h) of all the exposed IGBT module surfaces above the baseplate lowest surface was set to $5 \text{ W/(m}^2\cdot\text{K)}$ while the h of the baseplate bottom surface was set to $2500 \text{ W/(m}^2\cdot\text{K)}$. The heat transfer coefficient of the baseplate was set to a smaller value than the setting as introduced in Section 3.5.2, in order to obtain higher temperature ranges to verify the feasibility and accuracy of the FBG sensing scheme in the whole IGBT operation temperature ranges. A 25°C ambient temperature is assumed in the simulations

and mechanical effects (e.g., thermal expansion, residual fibre strain) are neglected. It should be noted that the fibre location used in this assessment was mostly chosen based on physical considerations, i.e. to facilitate ease of physical sensor installation in the same position during laboratory tests.

5.4.1 Transient response

This section investigates the IGBT installed FBG sensor's transient thermal response. Two different thermal interfaces are considered in the analysis. The 'air-interface' represents the case that the gap between the FBG sensor and the IGBT chip surface is filled with no additive thermal interface materials but with only air. The 'solid-interface' means the cases that the gap is filled with some thermal interface materials (either thermal paste or glues) with different thermal conductivities.

The temperature response of the FBG sensing head to a single 50A, IGBT switching cycle is shown in Fig. 5.6 for both thermal interfaces; the temperature variations shown in the figure mostly result from the conduction losses occurring in the IGBT structure due to the assumed current (switching) pattern.

As can be seen in Fig. 5.6, the temperature of the FBG with the high thermal conductivity material closely follows the temperature profile of the IGBT surface. In contrast, the 'air-interface' FBG exhibits a very different temperature profile.

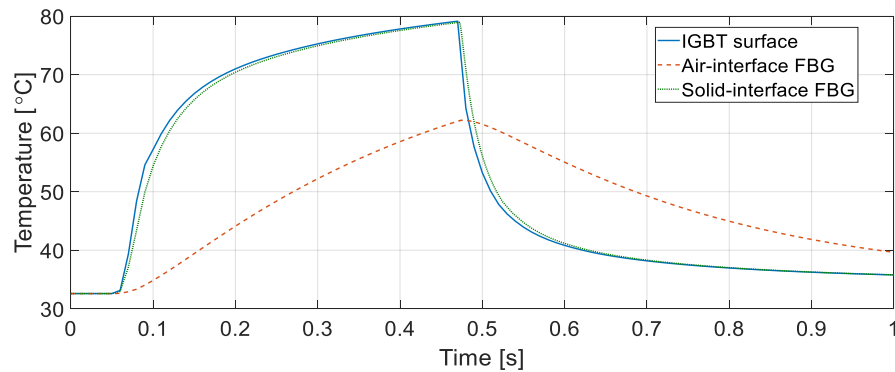


Fig. 5.6. FBG average sensing head temperature, transient response to a 50A, 0.5s pulse for a 75 μ m gap.

The poor correlation of the 'air-interface' FBG is further highlighted in Fig. 5.7, where tests are shown under the same current conditions but with a 5 μ m gap. Thus, even for a very small 5 μ m air-gap, a considerable difference in temperature profiles is observed between the 'air-interface' FBG and the sensed surface. In contrast, the 'solid-interface' FBG temperature is almost indistinguishable from that of the IGBT surface. Given that even minute air-gaps between the fibre and the monitored surface can be detrimental to the

sensor response, having a high thermal conductivity interface material is of utmost relevance. This is especially true when fast thermal changes need to be carefully monitored. Furthermore, as Figs. 5.6-5.7 suggest, the reported average temperature of the ‘air-interface’ FBG may include a considerable error, as further investigated in section 5.6.

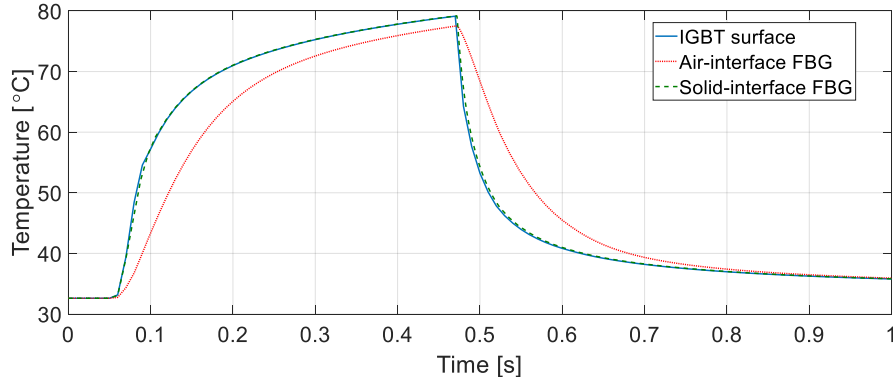


Fig. 5.7. FBG average sensing head temperature, transient response to a 50A, 0.5s pulse for a 5 μ m gap.

5.4.2 Stationary response

In this section, the FBG response under stationary conditions is analyzed for different switching frequencies. For the model solution, first, a steady state solution of the FE model is obtained assuming that an equivalent, RMS current flows through the module terminals. The resulting steady state solution is then used as the starting point for a time-domain simulation, where the FBG temperature response to the time-varying current can be observed. Fig. 5.8 shows a comparison of the FBG average temperature for the air and the solid interface FBG cases, when a 50A, 50% duty cycle current flows through the IGBT at either 1Hz, 10Hz or 100Hz switching frequency. An illustrative 75 μ m distance between the IGBT surface and the fibre bottom is considered in the simulations.

As can be seen in Fig. 5.8, the ‘air-interface’ FBG exhibits a much shorter temperature swing and a lower average temperature than the ‘solid-interface’ FBG, irrespectively of the switching frequency considered. The air-gap interface has an evident detrimental effect on the heat transfer between the sensed surface and the sensor. Hence, a good thermal interface between the FBG and the sensed area is required to have adequate transient and stationary temperature readings. Furthermore, although the mean FBG temperature for the ‘solid-interface’ FBG is similar to that of the IGBT surface for the investigated frequencies, as the switching frequency increases the FBG temperature fails to follow the IGBT surface temperature profile. This behaviour is largely related to the thermal interface thermal properties, as discussed below.

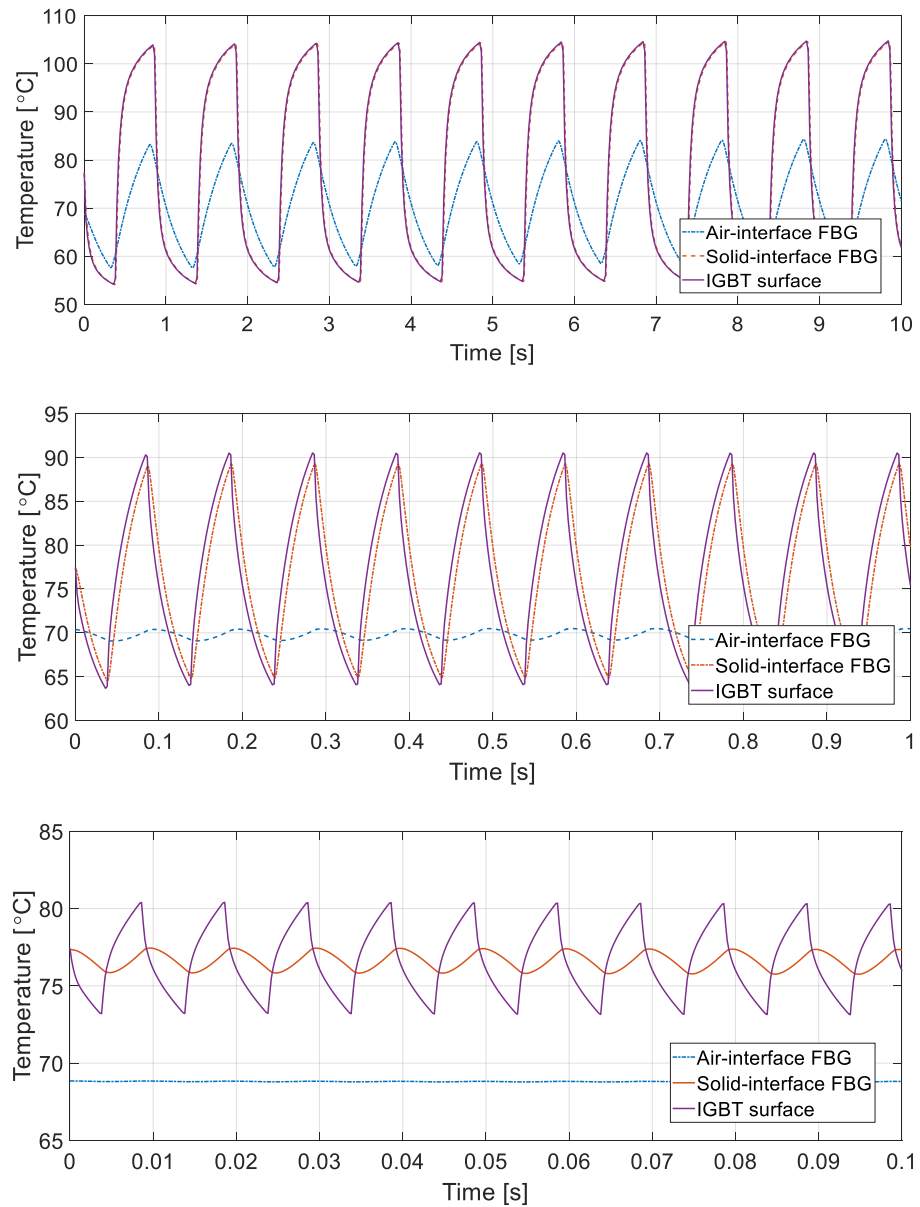


Fig. 5.8. FBG average sensing head temperature for a 75 μ m gap, 50A at 1Hz (top), 10Hz (middle) and 100Hz (bottom) switching frequencies.

In Fig. 5.9, the average temperature of the IGBT surface in the area where the FBG thermal interface is seated is compared to the FBG sensing head average temperature for the ‘air-interface’ case. Clearly, as the gap between the fibre and the sensed surface increases, the temperature swing of the FBG temperature decreases. The FBG temperature waveform also differs substantially from that of the IGBT surface temperature. These two observations suggest inadequate thermal coupling between the sensed surface and the sensor. It is interesting to notice in Fig. 5.9 that the gap variations have ± 1 °C on the FBG temperature waveform. This behaviour contrasts with the effect that variations in thermal interface thermal conductivity have on the waveform, as illustrated in Fig. 5.10.

In Fig. 5.10, the IGBT surface temperature is compared against the FBG temperature

when thermal interfaces with different thermal conductivities are employed. In the comparison a gapless FBG installation is assumed. The results in Fig. 5.10 show that as the thermal interface thermal conductivity increases, the FBG temperature more closely follows the surface temperature profile. However, even if a thermal interface with a higher thermal conductivity than the monitored surface is considered, the FBG temperature fails to match the temperature profile of the sensed surface. The difference between the monitored and sensed temperature can be explained as the result of a combination of factors: the short time between switching events, the relatively low thermal conductivity of the optic fibre (1.38 W/(m·K) for silica glass) and the assumed temperature averaging effect occurring in the FBG. The combination of such factors prevents the FBG from reaching an average temperature identical to that of the sensed surface: ideal, instantaneous heat transfer is required to eliminate such difference, which is unattainable in practical applications.

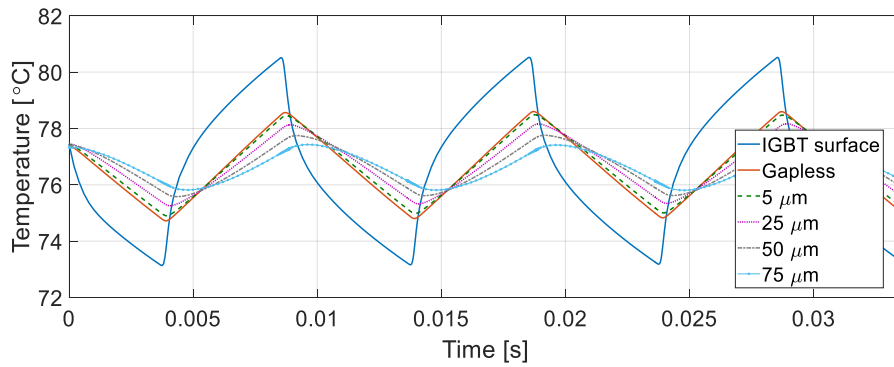


Fig. 5.9. FBG average sensing head temperature for different interface gaps at 100Hz, 50A.

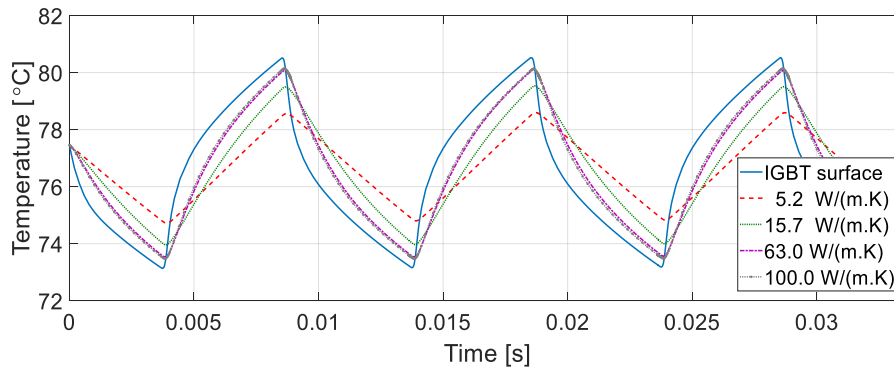


Fig. 5.10. Gapless FBG average sensing head temperature for different thermal interface thermal conductivities at 100Hz, 50A.

To achieve the best correlation between the sensed temperature and that perceived by the sensor, a thermal interface with a thermal conductivity similar to that of the sensed surface is required. This is necessary if tracking low magnitude, fast switching events is required.

In the FE model, the top solder layer (where the FBG is seated) has a thermal

conductivity of 63 W/(m·K). Electrically nonconductive thermal pastes with such high thermal conductivity value are not available. This limitation suggests the need for a metal based thermal interface, when thermal effects resulting from fast switching, low duration events need to be closely monitored. To accommodate such interface, more drastic and challenging modifications to commercial IGBT module design and manufacture would be required. The assessment of such alternatives is beyond the scope of this study, whose main thrust is to assess the FBG performance for in-situ temperature sensing on commercially available IGBT modules.

5.5 Influence from the interface materials on the sensors

In the principle of the FBG sensors, thermal fluctuation leads to a change in the reflected light wavelength. The interrogator decodes the light wavelength and uploads the wavelength values to the PC. The measured temperature values are then calculated from the light wavelength based on the wavelength to temperature (λ - T) relationship. Therefore, each FBG sensor needs to be calibrated before attachment to establish the λ - T relationship, as described in Section 5.2. After being attached on the IGBT chip with a certain interface material, each FBG sensor was re-calibrated several times, until the λ - T relationship reached a new stable trend. This recalibration process is conducted to check for any interference introduced by mechanical stress exerted on the FBG sensor from the interface materials and installation methods. The λ - T relationship of the ‘air-interface’ case and the ‘paste-interface’ are found keeping constant after the installation. The changes in the λ - T relationship observed after glue curing compared to the free FBG, are discussed in this Section based on the calibration results.

5.5.1 ‘Air-interface’ case and ‘paste-interface’ case

The FBG sensors were calibrated after being installed to confirm whether any modulation to their λ - T characteristic. To this end the FBG instrumented IGBT power modules (‘air-interface’ case and ‘paste-interface’ case) were fixed on a stainless-steel plate which was then placed inside a controlled thermal chamber and the calibration procedure described in section 5.2 repeated.

For both cases, the calibration results were found to be closely similar to the calibration results of the free FBG sensors. The maximum difference between the ‘air-interface’ case and the free FBG sensor is 2 pm in wavelength (equivalent to about 0.2 °C in temperature) while the maximum difference between the ‘paste-interface’ case and the free FBG sensor is

3 pm in wavelength (equivalent to about 0.3 °C in temperature). These differences are deemed too low to require in-situ calibration, hence for simplicity the free FBG sensor calibration characteristic can be used in practice for in-situ measurement.

5.5.2 Glue 8329TCM based ‘Glue-interface’ case

The λ - T relationship of the FBG sensor (named FBG 1) in glue 8329TCM based ‘Glue-interface’ case was calibrated after the cure of the glue. The λ - T relationship was found changing after installation. Seven sets of calibration after installation were done to analyse the change and study the new wavelength-temperature relationship resulting from the installation. Results for FBG1 are shown in Fig. 5.11.

Fig. 5.11 (b) shows a zoomed-in view of the measurements taken at 120 °C. The second to seventh calibrations show a relatively stable condition. The average of the second to seventh calibrations is defined as the new wavelength to temperature relationship and is drawn in Fig. 5.12 (a) together with the error bar. The standard deviation (SD) of the second to seventh calibration results is shown in Fig. 5.12 (b), which shows that the FBG-glue condition becomes increasing stable when the temperature increase.

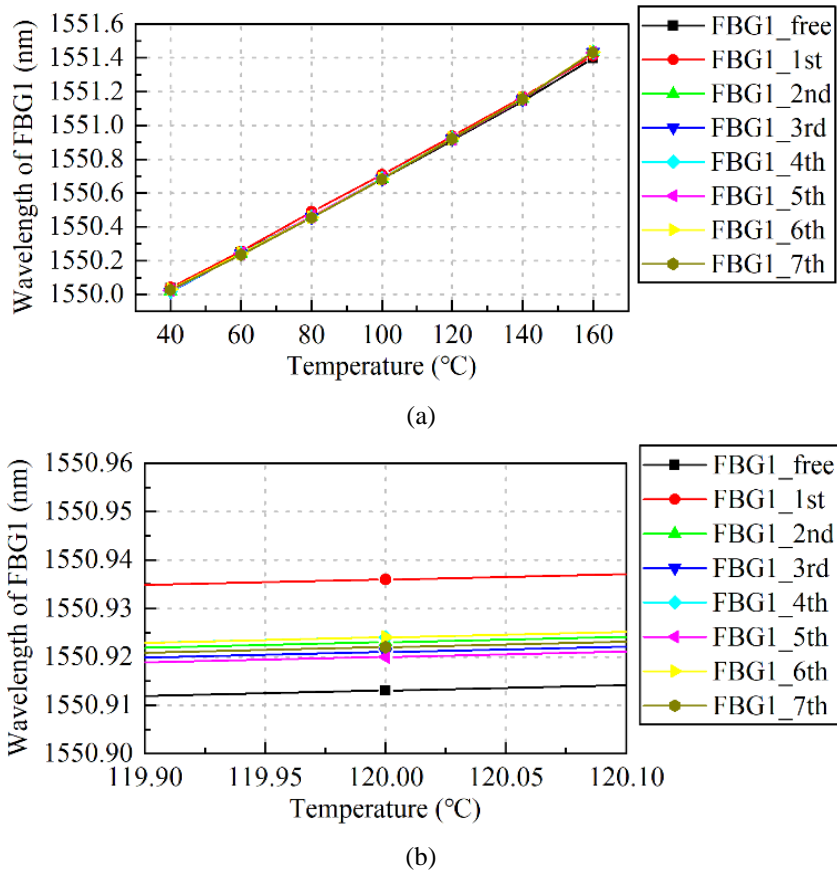


Fig. 5.11. The calibration results of FBG sensor 1 before and after the installation. (a) The 8 iterations of calibration results across the whole temperature range. (b) Detailed calibration results at 120°C.

Fig. 5.13 presents the difference in measured wavelength value between each post curing calibration and that of the free FBG sensor; the corresponding change in temperature is indicated on the right side of the figure. Here a 0.01 nm change in wavelength generally corresponds to $\approx 0.87^\circ\text{C}$ temperature change according to the thermal sensitivity defined in Eq. 2.2. As the FBG sensor is only susceptible to temperature and strain, the changes shown in Fig. 5.13 should result from parasitic, adhesive induced strain, as thermal conditions are identical between tests. Moreover, since the free FBG sensor calibration is performed in zero strain conditions the difference shown in Fig. 5.13 means that adhesive induced mechanical strain is present.

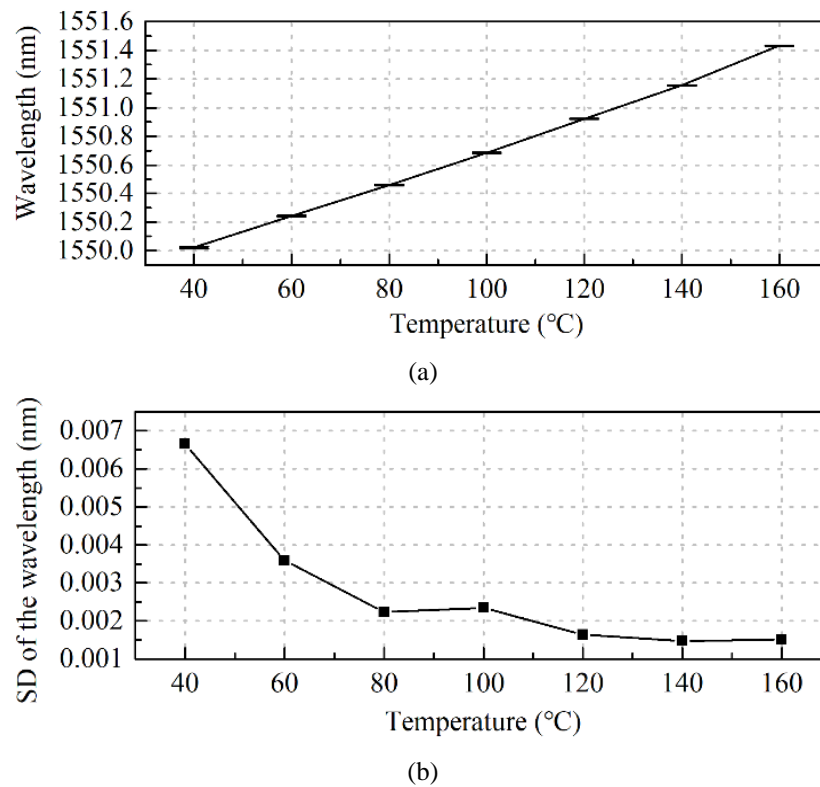


Fig. 5.12. The average and standard deviation of the second to the seventh calibration results of FBG sensor 1. (a) The average calibration curve. (b) The standard deviation of the average calibration curve.

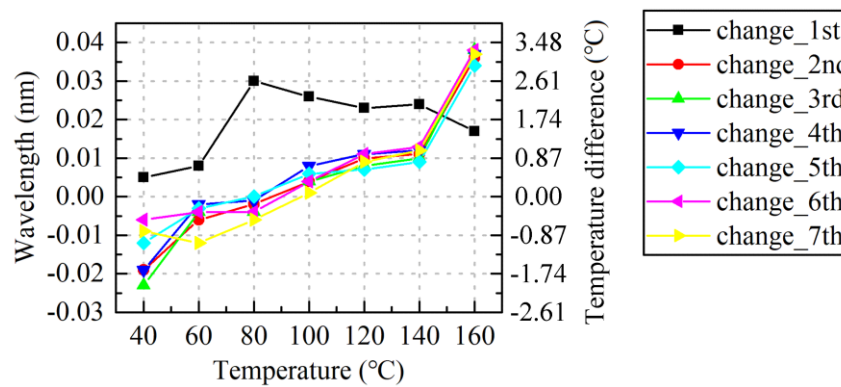


Fig. 5.13. The changes in the calibration results compared with the free FBG sensor

The black trace in Fig. 5.13 shows that the adhesive curing induced residual strain was close to zero at low temperature. At higher temperatures and up to the maximum 160 °C however the residual strain is seen to be more pronounced. This is believed to largely be caused by the adhesive and the fibre CTEs mismatch, as both will expand with temperature increase however the adhesive's CTE is larger, and its higher expansion could thus impose residual strain on the sensor.

Fig. 5.13 also shows that, for the 2nd to 7th calibrations the wavelengths measured at 40 °C are relatively dispersed. The temperature of the test IGBT was decreased to ambient between experiments. However, the adhesive's multiple transition between "glassy" and rubbery state is nonlinear and with a hysteresis component [127][128]. Therefore, it cannot be guaranteed that the adhesive's condition at ambient temperature is identical between calibrations, particularly in case of the 1st calibration performed after curing. For instance, it is argued in [128] that substantial differences in epoxy compound's internal/residual strain may exist due to incomplete curing, which can be particularly evident after the first transition cycle. These uncertainties can further explain the differences in Fig. 5.13. Furthermore, post-curing (exposing adhesive to high temperature after initial curing) is known to stabilize adhesive physical properties [128]. Thus, the CTE mismatch effects combined with those arising from variations in the adhesive's state can give rise to the observed wavelength variations.

Additionally, Fig. 5.13 shows that the wavelength changes of the 2nd to 7th calibrations are negative when the temperature is lower than 80 °C but positive at temperatures higher than 100 °C. This suggests that the state at which the residual strain is close to zero has transitioned from ambient temperature to ≈ 90 °C after the 1st calibration.

5.5.3 Glue ES578 based 'Glue-interface' case

ES578 has a higher T_g and a higher cure temperature compared with the glue 8329TCM. ES578 was tested using one FBG sensor labelled FBG 2, and cured at 100 °C.

Four calibrations were performed and compared with the free FBG sensors calibration curve. The results for FBG 2 are shown in Fig. 5.14. To avoid at first the influence of the adhesive's T_g , the maximum temperature during the initial batch of four calibration tests was purposely set to 80 °C, 25 °C lower than the adhesive's T_g .

The calibration curves after installation show a large negative deviation from the free FBG sensor calibration curve, as shown in Fig. 5.14. The negative deviation indicates an evident residual stress induced by the cured epoxy adhesive. As a result it can be seen that

the free to bonded wavelength difference at 40 °C is ≈ 0.4 nm. Post sensor installation calibration is therefore necessary for the ES578 bonded FBGs' wavelength to be accurately translated into temperature. This would require the entire module to be exposed to a thermal calibration process which would impose an undesirable degree of complexity in practical application.

It should be noted that the four iterations of calibration results were highly consistent, showing only minute differences compared with each other, as shown in Fig. 5.15.

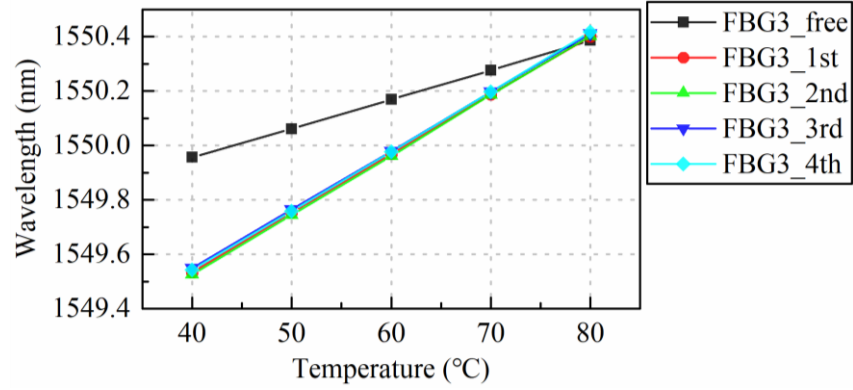


Fig. 5.14. The calibration results of FBG sensor 2 before and after the installation

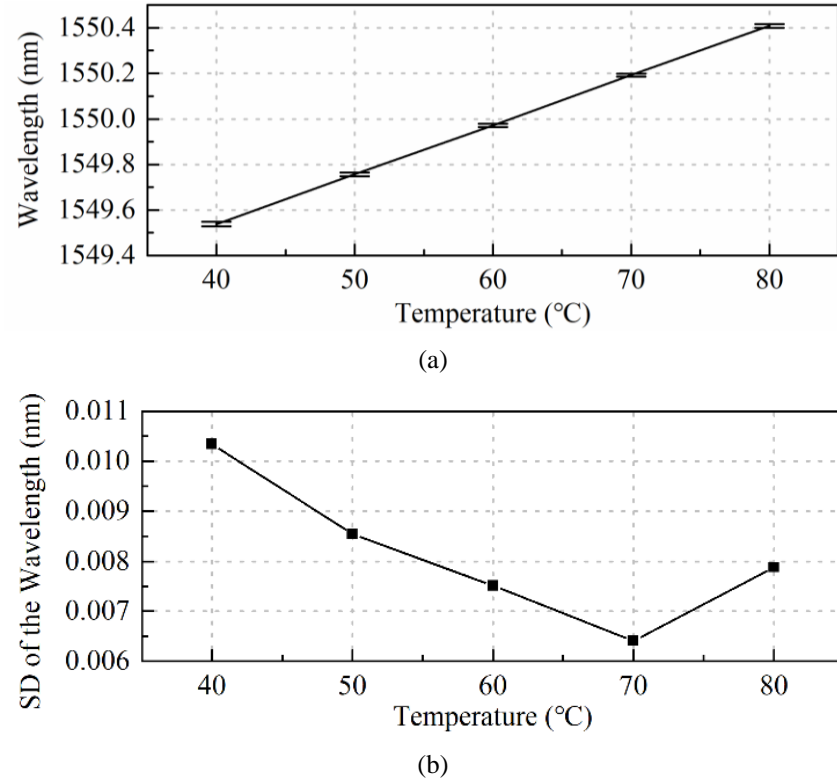


Fig. 5.15. The average and standard deviation of the first to the fourth calibration results of FBG sensor 3

This consistency may be attributed to the fact that the maximum temperature used during calibration did not exceed the adhesive T_g , and therefore the adhesive's non-linear working region is avoided. Thus, the adhesive maintained consistent properties during the

multiple separate calibrations performed. To verify this observation, the bonded FBG 2 were calibrated in the full chip's temperature range up to 160 °C (thus $>T_g$ of 105 °C) another four times and results shown in Fig. 5.16.

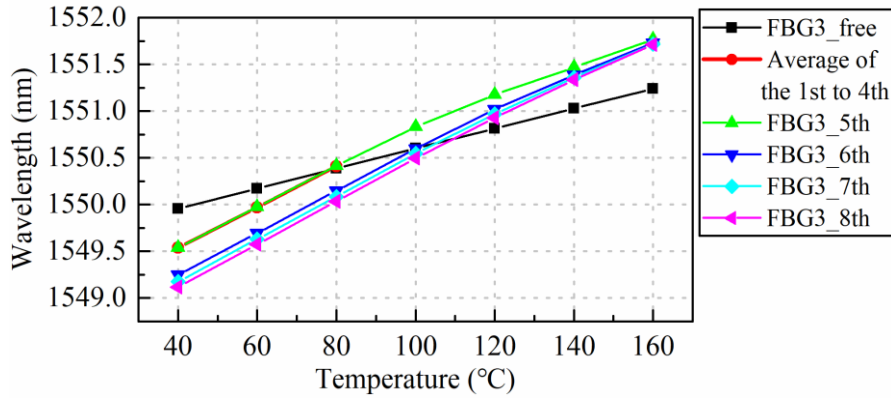


Fig. 5.16. The calibration results of FBG sensor 3 with temperature higher than the T_g

The 5th T - λ calibration curve, shown in green in Fig. 5.16, is similar to the average curve shown in Fig. 5.15 (a) for the 40 °C to 80 °C temperature range. However, the T - λ curve is seen to lose linearity at temperatures exceeding 100 °C. As the adhesive's CTE is larger than that of the fibre, the adhesive can expand at a higher rate, resulting in possible added residual stress on the fibre, and an increased bonded sensor calibration characteristic's slope compared to that of the free FBG, as seen in both Fig. 5.14 and Fig. 5.16. The adhesive's transition to rubbery state once operating temperature is above its T_g could potentially dampen the residual strain transfer and contribute to the observed gradual calibration curve slope reduction at above T_g temperature. This would require further research that is beyond the scope of this study.

In addition, the T - λ curve change is evident after the 5th calibration, once the adhesive's T_g was exceeded. In Fig. 5.16, the 6th to the 8th calibration curves exhibit notably lower and consistent wavelengths in the range of 40 to ≈ 120 °C compared with the 5th calibration curve. However, the wavelengths at ≈ 140 to ≈ 160 °C of the 5th to 8th calibration curves are relatively close. This pattern is similar to the pattern shown in Fig. 5.13 for the lower T_g adhesive. Thus, post-curing seems to help to stabilize the adhesive physical properties. It is also interesting to notice that the intersection with the free FBG calibration curve moved from ≈ 80 °C to ≈ 105 °C, which indicates that the state in which the residual strain equals zero has transitioned from ≈ 80 °C to close to T_g . The observed change with thermal cycling is consistent with published results [128].

5.5.4 Glue TCOR75S based ‘Glue-interface’ case

The third adhesive tested, TCOR75S, is a thermally conductive, vulcanized silicone-based adhesive. It is notably different from the two previously investigated adhesives in rated hardness and T_g values. As cured silicone has a very low T_g , typically around -20°C , no state transition should occur for a practical IGBT operating temperature range. Therefore, the adhesive is expected to exhibit consistent physical properties for the whole IGBT operating temperature range.

The cured TCOR75S adhesive is medium soft and elastic, and sufficient to ensure a solid bond in this application. However, the bond strength provided by this adhesive is relatively lower and thus the residual strain induced by the adhesive expected to be lower than that of the more rigid epoxy-based adhesives assessed in previous sections.

Similar to the previous cases, one FBG sensor labelled FBG 3 was installed using TCOR75S on a test IGBT. Four separate calibrations were performed after sensor installation and adhesive curing in the temperature range of 40 to 160°C .

The calibration curves obtained in tests for the full thermal range of up to 160°C are shown in Fig. 5.17. The 1st calibration curve is seen to be close to the free FBG calibration in the temperature range below 80°C , and slightly large in the range above 100°C . The slope of the 1st calibration curve is slightly larger than that of the free calibration curve, and the intersection of the two curves is below 80°C .

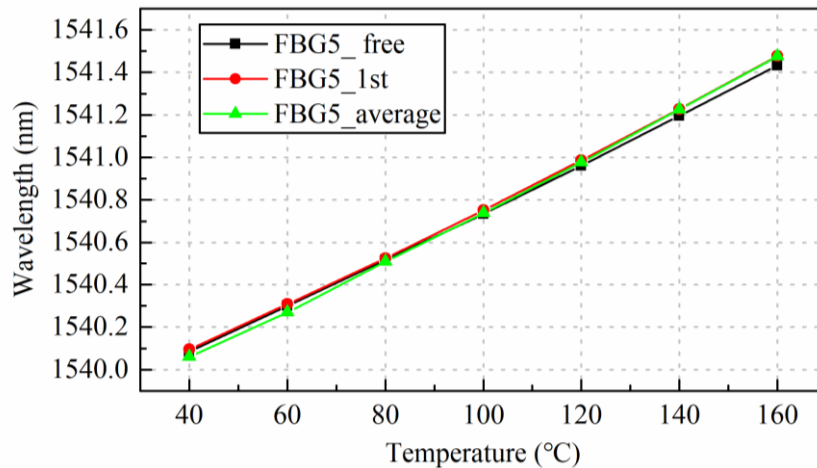


Fig. 5.17. Calibration results of FBG 5 sensor for rated temperature range.

After the first temperature increase to a high level as a part of 1st calibration, the curves obtained in the following three calibration tests (2nd to 4th) exhibit a larger slope compared with the 1st. Since the 2nd to 4th calibration curves show a stable condition with the standard

deviation below 0.007 nm, their average value is used in Fig. 5.17 to ensure the picture clarity. Besides the changed slope, the intersection of the average curve with the free calibration curve increases to around 100 °C.

This change pattern is similar to the patterns shown in Fig. 5.13 and Fig. 5.16, which suggests that all the tested adhesives experience a similar process during calibration, but with different levels of intensity. Thermal cycling over the rated temperature measurement range (post-curing) seems to be required to ensure highly consistent, repeatable measurements.

5.5.4 Summary of glue-induced effects

The study above shows the glue-induced effects on the performance of the FBG sensor. The application of cured glues for securing the FBG sensors ensures a robust attachment; however, it also generates residual mechanical stress or strain, denoted as $\Delta\epsilon$ in Eq. 2.1. This factor cannot be ignored in cases involving glue bonding, as changes in $\Delta\epsilon$ introduce complexities to temperature measurement. The calculation of the sensor-measured temperature from the wavelength is influenced by $\Delta\epsilon$, reflecting on the wavelength to temperature (λ - T) relationship update.

The CTE of the fibre is much smaller than that of the glues. Therefore, when the temperature decreases, the glue will shrink at a higher rate and can impose a resulting additional mechanical compressive strain on the FBG sensor thus leading to a decrease of the reflected wavelength. In contrast when the temperature increases (but remains below the T_g), both the glue and the fibre expand, but at different rate. The glue expands more in volume than the fibre, so following the described principles, can in this case impose additional tensile strain on the sensing fibre, and lead to an increase in the reflected Bragg wavelength.

The glue transits from the solid state to the rubbery state as the temperature exceeds its T_g . In the rubbery state, the glue becomes softer and experiences loss of rigidity, thus the strain brought from the glue to the fibre (embedded in glue) tends to grow at a lower rate. In principle, it can be assumed that if the temperature keeps increasing and the glue keeps softening until fully losing rigidity, the change in glue material hardness will relax the strain imposed on the fibre to zero. When the external temperature starts reducing to below the glass transition temperature the process is reversed, and the glue will transit back from the rubbery state to the solid state around its T_g , producing some residual stress and altering the FBG λ - T relationship, compared to that of the free FBG.

Consequently, depending on the required accuracy, it may be necessary to re-calibrate the FBG sensor after installation. A "burn-in" thermal cycle could be utilized to achieve more consistent measurements. Moreover, owing to the non-linear behaviour of glue during state transitions, the λ - T relationship may become unstable, particularly at lower temperatures, resulting in measurement errors. Nonetheless, if the glue operates consistently in a single state either below or above T_g , precise measurements can be obtained, as non-linearities are avoided.

5.6 Temperature measurement analysis of ‘Air-interface’ case and ‘paste-interface’ case

The ‘glue-interface’ cases show alteration in the wavelength to temperature (λ - T) relationship in the installation process. Re-calibration after the installation is therefore necessary for the three ‘glue-interface’ cases to ensure the measurement accuracy. The double calibration requirement makes the ‘glue-interface’ cases inconvenient for industrial application compared with ‘air-interface’ and ‘paste-interface’. Therefore, given the latter has higher feasibility, thermal sensing performance of the ‘air-interface’ and ‘paste-interface’ are tested and compared in this section while the ‘glue-interface’ cases are not considered for in depth investigation.

The FBG instrumented and painted IGBT power module is tested in the test rig, with the DC power source providing a constant 50A DC current. The two IGBTs T1 and T2 from two IGBT power modules are controlled by PWM signals with 50% duty cycle and 15 V amplitude. Separate tests are performed for PWM signal frequencies of 1 kHz, 100 Hz, 10 Hz, and 1 Hz. The thermal measurements are taken after allowing sufficient time for the test module to reach thermal equilibrium in the existing test conditions.

The FBG measurements obtained for 1 kHz operation in the ‘air-interface’ case and the corresponding thermal image taken by the thermal camera are shown in Fig. 5.18. As can be seen in Fig. 5.18(a), the average temperature measured by the FBG sensor is 67.2°C. The point identified in the thermal image in Fig. 5.18(b) is the thermal camera measured temperature in the location of the FBG head and can be seen to be in the range of 71.1 °C to 71.4 °C. The measurement of the ‘air-interface’ FBG sensor is observed to be ≈ 4 °C lower than the reference temperature.

The measurement obtained by the ‘solid-interface’ FBG sensor at 1 kHz is shown in Fig. 5.19(a), reporting an average temperature of 73.2 °C. The corresponding reference

temperature given by the thermal camera is $\approx 73.06\text{ }^{\circ}\text{C}$ to $73.44\text{ }^{\circ}\text{C}$ (Fig. 5.19(b)). It can be observed that the ‘solid-interface’ FBG sensor measurement is highly consistent with that obtained by the thermal camera. The measurement of the FBG sensor can be concluded to be accurate.

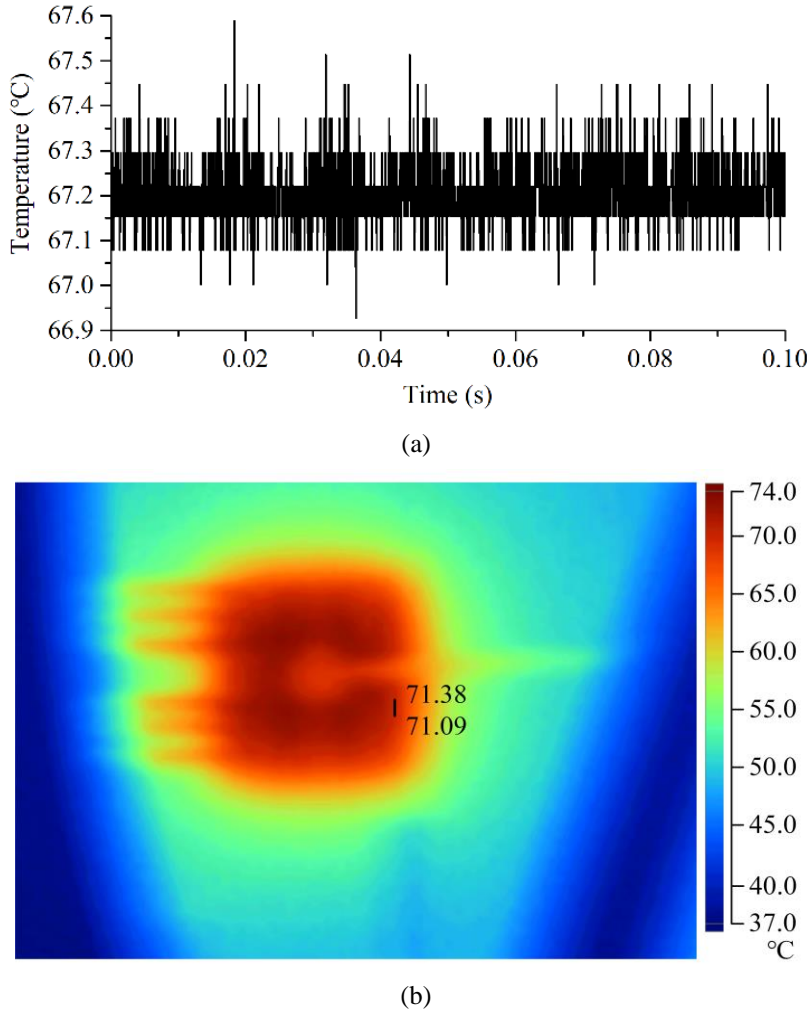
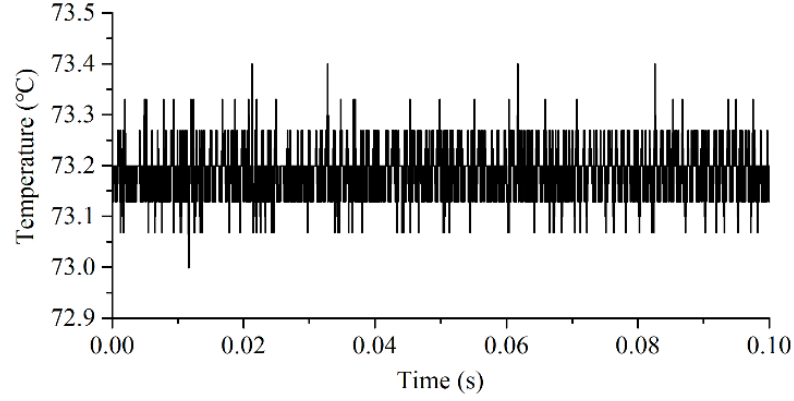


Fig. 5.18. Measurement of the ‘air-interface’ FBG sensor and the reference thermal image at 1 kHz. (a) The temperature measured by the ‘air-interface’ FBG sensor. (b) The thermal image taken by the thermal camera.

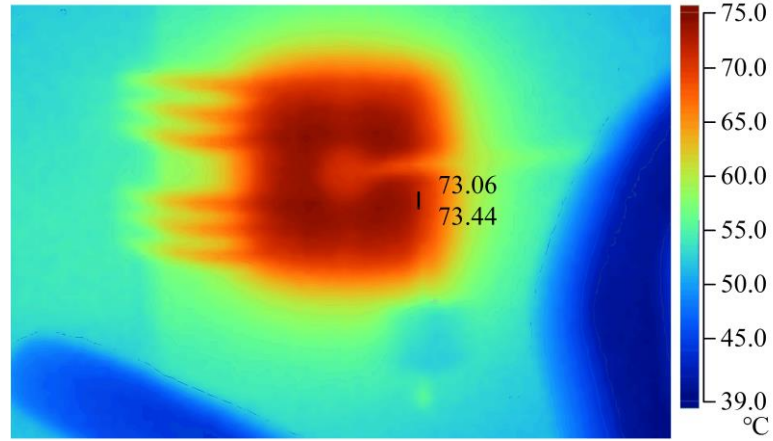
The more accurate measurement of the ‘solid-interface’ setup compared to the ‘air-interface’ case is largely attributed to the good heat conduction provided by the thermal paste installed between the FBG sensor and IGBT surface: the thermal conductivity of the paste and air are $5.2\text{ W}/(\text{m}\cdot\text{K})$ and $0.031\text{ W}/(\text{m}\cdot\text{K})$, respectively. The minute air gap in the ‘air-interface’ case between the FBG head and the IGBT surface leads to a negative error in the temperature measurement because the air gap has a large thermal resistance.

The observed minute temperature fluctuations can be attributed to variations in ambient temperature and intrinsic equipment measurement error. Under the PWM frequency of 100 Hz, the temperatures measured by the ‘air-interface’ and ‘solid-interface’ FBG sensors are

shown in Fig. 5.20. A distinctive variation at PWM frequency can be seen in the time domain measurement for the ‘solid-interface’ case (red trace) but is not observable in the ‘air-interface’ FBG sensor measurements, further confirming the higher fidelity provided by the ‘solid-interface’ sensing setup.



(a)



(b)

Fig. 5.19. Measurement of the ‘solid-interface’ FBG sensor and the reference thermal image at 1 kHz. (a) The temperature measured by the ‘solid-interface’ FBG sensor. (b) The thermal image taken by the thermal camera.

The temperatures measured by the ‘air-interface’ and ‘solid-interface’ FBG sensors when the PWM frequency is 10 Hz are shown in Fig. 5.21. The fluctuation in the temperature measured by the ‘solid-interface’ FBG sensor becomes quite large. The maximum temperature reaches $\approx 79.8^\circ\text{C}$ while the minimum temperature reaches $\approx 69.4^\circ\text{C}$. The peak-to-peak value is $\approx 10.4^\circ\text{C}$. In contrast, the PWM frequency is considerably less noticeable in the temperature measured by the ‘air-interface’ FBG sensor, showing a modest peak to peak value of $\approx 1.1^\circ\text{C}$.

When the PWM frequency is 1 Hz, the temperatures measured by the two cases are shown in Fig. 5.22. The temperature measured by the ‘solid-interface’ FBG sensor reports

a considerable fluctuation, whose peak-to-peak value is ≈ 49.4 °C. In contrast, the peak-to-peak value of the temperature fluctuation reported by the ‘air-interface’ FBG sensor are more modest at ≈ 24.6 °C.

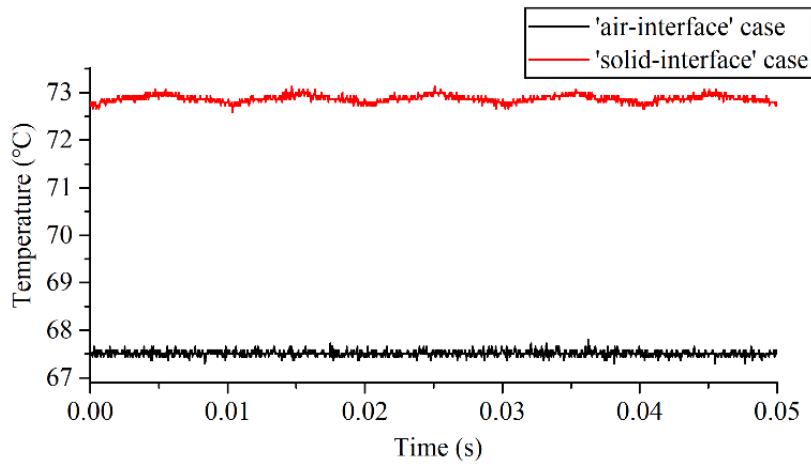


Fig. 5.20. Temperature measured by the ‘air-interface’ case and the ‘solid-interface’ case at 100 Hz.

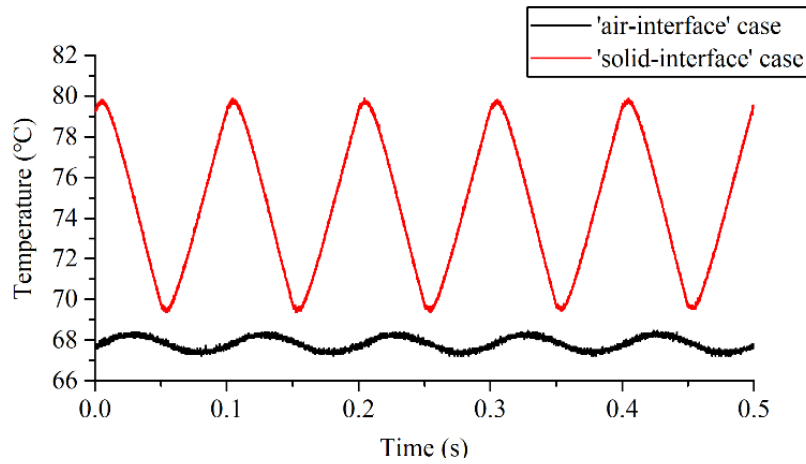


Fig. 5.21. Temperature measured by the ‘air-interface’ case and the ‘solid-interface’ case at 10 Hz.

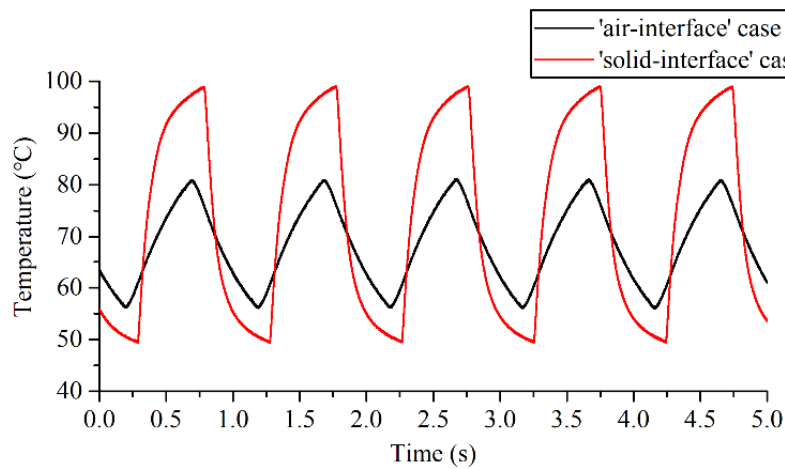


Fig. 5.22. Temperature measured by the ‘air-interface’ case and the ‘solid-interface’ case at 1 Hz.

The maximum, minimum, and average temperature measured by the two FBG cases are listed in Table 5.3. The differences shown in the measurement of the two installation

cases at 100 Hz, 10 Hz, and 1 Hz PWM frequencies are related to the air gap and the thermal paste. The higher thermal conductivity of the thermal paste forms a smaller thermal impedance between the FBG sensor and the IGBT surface, so that the 'solid-interface' FBG sensor can respond to the change in the IGBT surface temperature more rapidly.

Compared with the simulation results depicted in Fig. 5.8, the experimental results and simulation outcomes generally exhibit consistent temperature values and fluctuation amplitudes. At the PWM frequency of 100 Hz, the simulation results showcase approximately 2 °C fluctuation for the 'solid-interface' case and no visible fluctuation for the 'air-interface' case. Additionally, the temperature sensed by the 'air-interface' case is about 7 °C lower than that sensed by the 'solid-interface' case in the simulation. The experimental results presented in Fig. 5.20 illustrate a 1°C fluctuation for the 'solid-interface' case and constant temperature for the 'air-interface' case, with a temperature difference of approximately 5 °C. At a PWM frequency of 10 Hz, both the experimental and simulation results show a fluctuation of about 1°C for the 'air-interface' case, with the sensed temperature being approximately 7 to 8 °C lower than the measurement of the 'solid-interface' case. When the PWM frequency is 1 Hz, both the 'air-interface' case and the 'solid-interface' case exhibit consistent fluctuation amplitudes between the experimental results and the simulation results. Although the temperature sensed by the 'solid-interface' case in the experiment is about 5 °C lower than the simulated temperature, the relative position of the two temperature curves sensed by the 'air-interface' case and the 'solid-interface' case remains consistent. The alignment between the experimental results and the simulation outcomes validates the accuracy of the FEA model and the reliability of the obtained sensing performances of the two cases.

The temperatures of the IGBT chip are also measured by the thermal camera for PWM frequencies set to 100 Hz, 10 Hz, and 1 Hz in tests. However, the temperature fluctuations at high frequency cannot be recorded by the thermal camera which is limited in this respect by a practical refresh rate of 9 Hz. To validate the FBG sensors' measurement, the thermal camera viewfinder was recorded for a 2-minute period to obtain a thermal video of the IGBT chip for each installation type and each tested frequency. The maximum and minimum temperatures measured in the 2-minute video are listed in Table 5.3 to be compared with the corresponding FBG measurement for validation. The temperature ranges measured by the thermal camera for the two installation types are seen to be in close agreement. The temperature ranges measured with the 'solid-interface' FBG are highly consistent with those observed by the thermal camera for the three different frequencies

considered. However, for the ‘air-interface’ FBG, the temperature swings and levels recorded by the camera are larger and higher than those measured by the FBG sensors for all the investigated frequencies.

Table 5.3. Temperature measurements for the two FBG cases at 50A

50 A DC		‘air-interface’		‘solid-interface’	
		FBG	Camera	FBG	Camera
100 Hz	T_{\max} (°C)	67.8	73.4	73.2	73.4
	T_{\min} (°C)	67.1	73.9	72.6	72.9
	T_{ave} (°C)	67.4	73.6	72.9	73.1
10 Hz	T_{\max} (°C)	68.4	78.5	79.8	80.3
	T_{\min} (°C)	67.3	69.2	69.4	70.0
	T_{ave} (°C)	67.8	73.8	74.7	75.1
1 Hz	T_{\max} (°C)	80.8	98.0	98.8	98.1
	T_{\min} (°C)	56.2	52.8	49.4	53.0
	T_{ave} (°C)	68.4	75.4	73.7	75.5

Further tests were conducted at other current levels and consistent sensing performance was observed. For illustration purpose the results of tests conducted at 30 A DC current for 1 kHz, 100 Hz, 10 Hz, and 1 Hz are shown in Table 5.4. The temperatures measured by the ‘solid-interface’ and ‘air-interface’ FBG sensors exhibit a similar behaviour to those recorded at 50A, with the measurements obtained with the ‘solid-interface’ sensor showing a closer agreement with the thermal camera recordings.

Table 5.4. Temperature measurements for the two FBG cases at 30A.

30A DC	‘air-interface’		‘solid-interface’	
	FBG	Camera	FBG	Camera
$T(\min/\max)$ at 1 kHz (°C)	47.0-47.4	50.0-50.4	50.3-50.6	50.9-51.3
$T(\min/\max)$ at 100 Hz (°C)	47.6-47.9	52.2-52.7	50.4-50.8	52.0-52.3
$T(\min/\max)$ at 10 Hz (°C)	47.6-48.4	50.9-55.1	47.2-54.5	49.8-54.3
$T(\min/\max)$ at 1 Hz (°C)	42.2-54.3	43.8-62.9	36.5-61.3	41.9-60.2

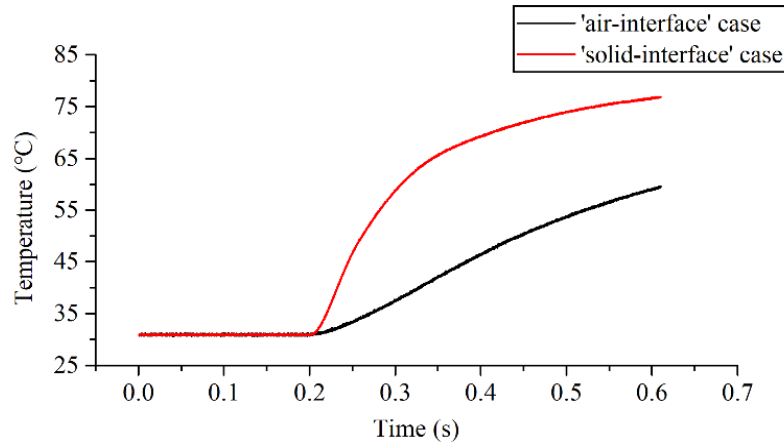


Fig. 5.23. Step responses for the 'air-interface' and 'solid-interface' FBG installations.

To test the sensitivity of the two FBG installation types to sudden temperature changes arising from large IGBT current transients, the sensor step response was also investigated. A step current with an amplitude of 50A was applied to the IGBT power modules for the 'air-interface' and 'solid-interface' cases under identical initial conditions. The recorded temperature step responses for the two cases are shown in Fig. 5.23. The data show that the 'air-interface' case response exhibits a much slower rise rate, compared to the 'solid-interface' case. The step response test reflects the substantially smaller thermal resistance introduced by the 'solid-interface', compared with that of the 'air-interface' case. This test confirms the benefits suggested by the FEA simulations of using a strong thermal interface between the sensor and the sensed surface when fast temperature changes need to be tracked.

5.7 Summary

This chapter demonstrates the performance features and application requirements of direct on-chip thermal sensing in IGBT modules using FBG technology, with a particular emphasis on the sensor bond interface with the chip surface. To evaluate and characterize the operative characteristics of junction temperature in-situ sensing on a commercial IGBT module design, the study employs a bespoke laboratory test system and an FE model. The FE simulation results indicate that to monitor fast, short duration transient events, a strong thermal interface is necessary. The simulations also reveal that even miniature air gaps between the sensor and the monitored surface can result in reduced temperature accuracy readings. These findings were further validated in experiments on a purpose-built experimental test system containing IGBT modules with an FBG sensor mounted directly on the top chip surface for direct measurement of the IGBT junction temperature.

The pre- and post-installation FBG sensor calibration characteristics analyzed in the

study demonstrate that the thermal paste interfacing technology does not affect the free sensor temperature-wavelength characteristic. Thus, direct installation or retrofit of sensors to suitable power electronic systems can be done without requiring re-calibration after sensor installation and the associated practical challenges. However, wrapping the FBG sensor inside the glue can create additional glue-induced mechanical strain/stress on the FBG sensor during the temperature change process due to the CTE mismatch of the glue and the fibre. Sensor post-installation calibration is necessary to ensure accurate measurements. Avoiding the glue's non-linear transition region can alleviate many of the negative, glue-induced effects. A glue that can cure at ambient temperature and whose T_g is either higher or lower than the operation temperature range is preferable to reduce the need for post-installation calibration.

The study's results suggest that using a soft, high conductivity thermal interface material can enable effective real-time, in-situ sensing of the IGBT junction temperature using FBG sensing technology within the rated current envelope. As observed from the thermal camera in tests, the temperature difference within the IGBT chip can be greater than 10 °C.

Chapter 6: FBG Head Size Influence on Localized On-chip Thermal Measurement in IGBT Power Modules

FBG sensors have demonstrated the potential for in-situ measurement on chips; however, further investigation is required to capture localized thermal conditions. The size of the FBG sensing head is of particular importance, as capturing the maximum temperature, or multiple distributed localised hotspots of interest on the small, unevenly heated chip surface may be affected by an inappropriate head dimension. Therefore, this section is to explore the impact of sensing head length on localized temperature sensing in an IGBT module and determine the fundamental requirements for effective thermal point sensing.

To achieve this goal, a thermal FEA model was first used to simulate the thermal map of the examined module, characterize its surface heat distribution, and identify the sensor locations of interest. Next, a specialized test rig was utilized to evaluate in-situ thermal monitoring performance of the chip geometry separately fitted with three different sizes of FBG sensors. Different orientations of sensing on the chip surface were analysed, along with the corresponding surface temperature distribution gradients, and their impact on individual sensor performance and in-situ applicability was assessed.

6.1 FEA thermal analysis

The FEA model introduced in Section 3.6 was used to simulate the thermal map of the examined module to characterize its surface heat distribution and inform the sensor locations of interest. The FEA model is re-drawn here as shown in Fig. 6.1. Due to module symmetry and to minimize computational requirements the thermal study focused on one of two IGBT chips contained in the test module (left chip in Fig. 6.1).

Typically, the IGBT is controlled by PWM signals to ensure that current flows through the chip only when it is switched on. This study investigated the chip's thermal behaviour under a nominal current amplitude of 50 A and a 50% duty cycle. The FEA model was employed to obtain the steady-state thermal distribution of the chip by applying an equivalent RMS current to terminal T1, with T3 grounded. The baseplate's bottom surface temperature was set to 22.0 °C, representing a typical ambient temperature, and the heat transfer coefficient was fixed at 3800 W/(m²·K) as explained in Section 3.5.2.

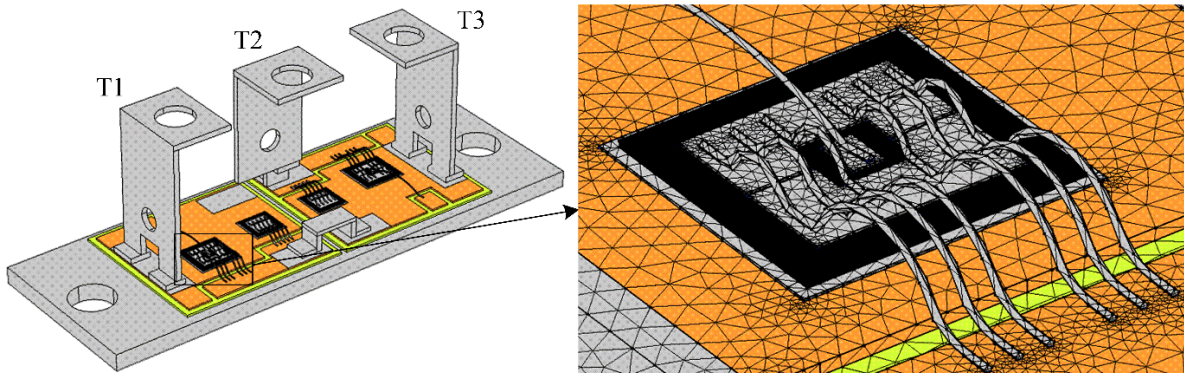


Fig. 6.1. The power module FEA model and IGBT mesh detail

The results are shown in Fig. 6.2. The hot spot is located near the bond wires, with the highest temperature found around the soldering connections of the bond wires as shown in Fig. 6.2 (b). The chip's gate is located in the centre, resulting in a quasi-radial temperature distribution on the chip surface. Fig. 6.2 (b) also shows that the temperature variation range on the chip surface is approximately 23 °C.

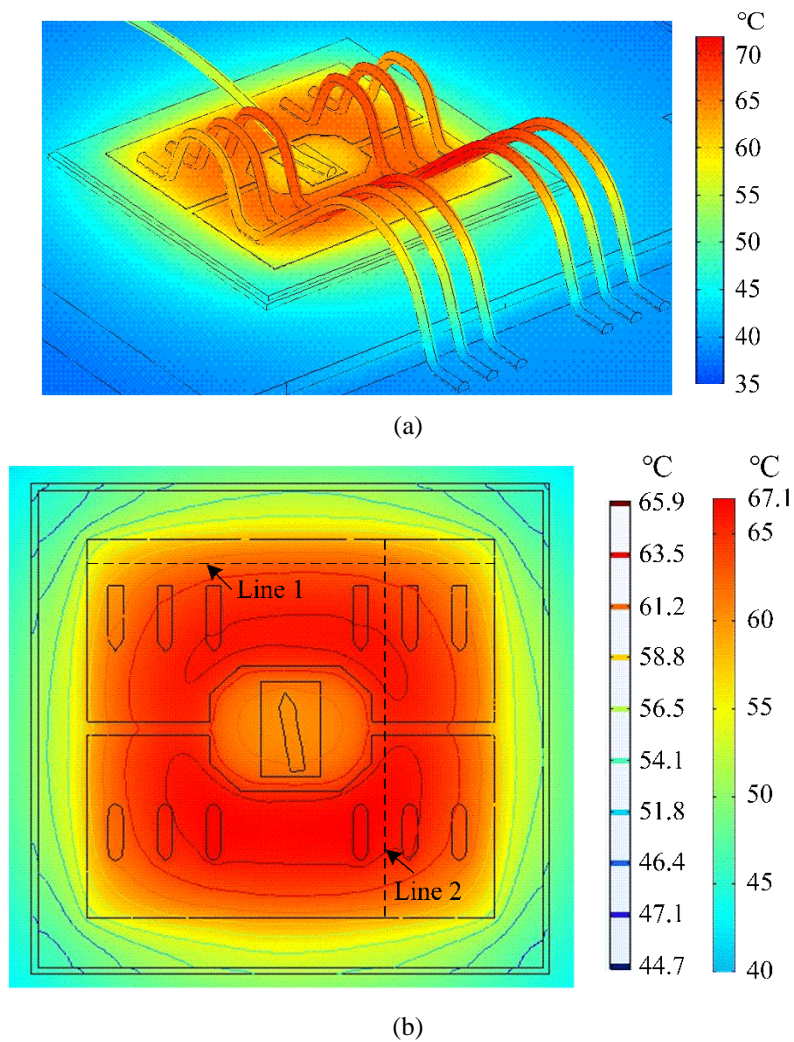


Fig. 6.2. FEA simulated thermal distribution of the IGBT chip. (a) IGBT chip with bond wires. (b) IGBT chip without bond wires.

To provide further insights related to sensor positioning, two auxiliary lines were drawn in Fig. 6.2 (b) to illustrate the chip surface temperature distribution in different orientations. Fig. 6.3 shows the predicted temperature distribution along line 1 (left to right) and line 2 (upper to lower side) in the solder layer. The black points represent discrete digitized simulation values, while the black lines are depicted using interpolation. The temperature gradient along the horizontal line 1 is highest at its centre point, whereas two temperature peaks are found along the vertical line 2. The line centre location does not constitute the thermal hot spot, as the two hottest areas are near the bond wire solder connections. This finding highlights the challenges associated with the placement of FBG sensors for observing localized surface thermal hotspots in a typical commercial IGBT geometry. Moreover, the temperature profiles in Fig. 6.3 show a considerable range ($\approx 8^\circ\text{C}$), and the practical implications of such variation on FBG temperature measurement are discussed in the subsequent sections.

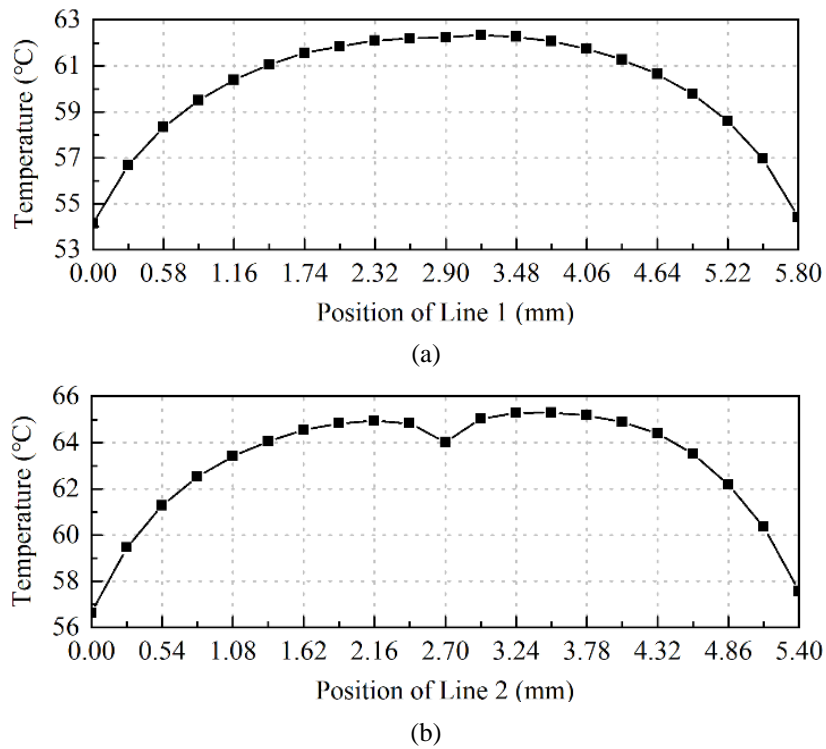


Fig. 6.3. FEA simulated temperature distribution along: (a) Line 1. (b) Line 2 in Fig. 6.2(b)

6.2 Test IGBT surface temperature distribution characterisation

In order to identify sensor locations of interest and to characterize the surface temperature distribution of the chip during operation, the test chip described in Section 4.1 was operated at a nominal current of 50 A and 1 kHz PWM frequency, and its surface thermal images were captured at thermal equilibrium. The ambient temperature during the

experiment was approximately 22.8°C. The thermal image obtained is shown in Fig. 6.4, which also displays the position of line 1. The observed locations of hotspots match those predicted by the simulations presented in section 6.1.

The temperature profile of line 1 is illustrated in Fig. 6.5, where the black points representing discrete values obtained in the experiment and the black line representing interpolated values. The presence of the gate bond wire in the area around the centre of line 1 resulted in a low temperature reading by the camera, as this area is obstructed. As shown in the simulation results in Fig. 6.3 (a), the actual temperature in this region is higher, but it cannot be directly measured with the thermal camera. However, the unobstructed measurements area reports similar temperatures to the simulated results, thereby further confirming their validity. To provide an indicative profile of the full line 1 thermal profile, the measurements obtained with a clear line of sight were curve-fitted using a 4th order fit, and the resulting profile is shown in red in Fig. 6.5.

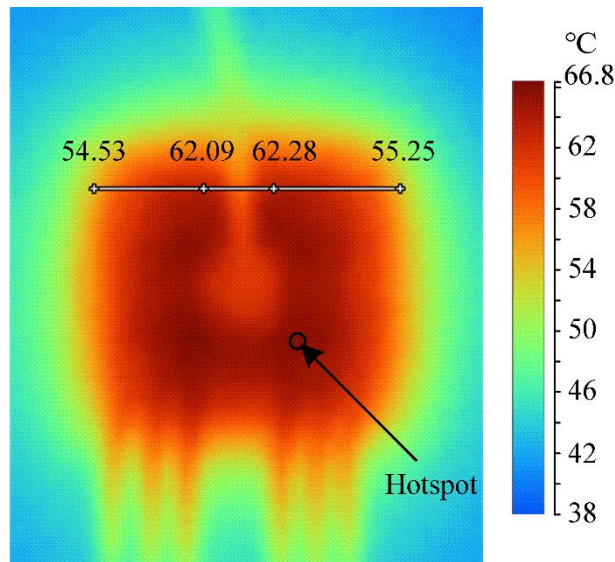


Fig. 6.4. IGBT surface thermal image at 50 A DC current

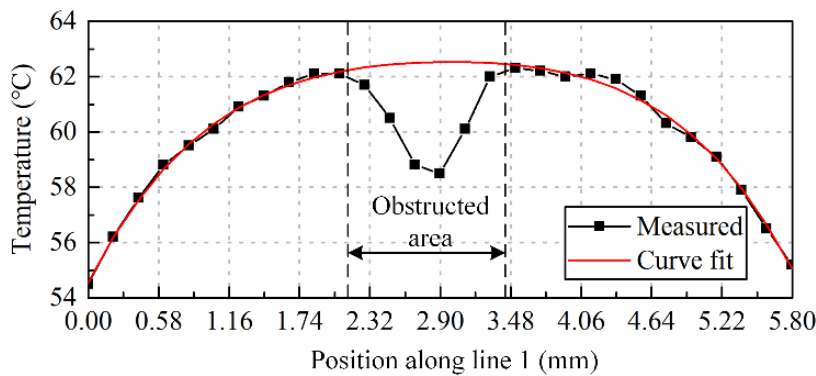


Fig. 6.5. Surface temperature distribution along line 1 (Fig. 6.2b) for thermal camera measurement.

6.3 Different head size FBG sensor performance analysis - experimental study

The impact of the sensor head size on thermal sensing performance was examined by conducting tests at various current operating points on the test IGBT, using the head interfacing method outlined in Section 5.3. The method involved placing the sensor at the desired location on the IGBT surface and filling the gap between the fibre and the chip surface with a high conductivity thermal paste, which facilitated improved heat conduction. The fibre termination was then loosely inserted into a Teflon capillary to retain its position, while the other end of the fibre was secured using glue to ensure stability. 1 mm, 3 mm and 5 mm FBG head lengths were assessed in experiments.

6.3.1 IGBT-FBG cases at location 1

Fig. 6.6 (a) (b) (c) illustrates the 1 mm, 3 mm, and 5 mm sensor instrumented IGBT chip, respectively, where the FBG head locations are marked red. The mid-points of all three considered head lengths are kept in identical location in tests, to provide consistency of comparison and assessment of length effects. The shaded sections of the IGBT bond wires in Fig. 6.6 represent the solder areas.

Fig. 6.7 illustrates the respective simulated thermal excitation profiles that the three examined FBG lengths are exposed to in-situ. The discrete digitized simulation values are represented by small black points, while the black lines are drawn using interpolation, as shown in Fig. 6.7. The thermal profile of the 5 mm FBG sensor head is presented in Fig. 6.7 (c), which is also illustrated in Fig. 6.3 (a). Since the mid-points of all three sensor head lengths are placed at the same location, the thermal excitation profile that the 3 mm FBG sensor is subjected to is depicted in Fig. 6.7 (b), which is the centre 3 mm area of Fig. 6.7 (c). Similarly, Fig. 6.7 (a) represents the centre 1 mm portion of Fig. 6.7 (c) and Fig. 6.7 (b).

This clearly shows that the sensing heads are exposed to non-uniform thermal excitation in this application, the scale of which is effectively defined by their length: the range of in-situ thermal excitation variation for the 1 mm, 3 mm, and 5 mm is predicted as $\approx 0.15^\circ\text{C}$, $\approx 1.3^\circ\text{C}$, and $\approx 5.0^\circ\text{C}$, respectively. A longer FBG head evidently results in a wider range thermal excitation imposed on the sensor. For the assessed IGBT geometry the thermal gradient that the 5 mm FBG sensor is expected to experience exceeds $2^\circ\text{C}/\text{mm}$.

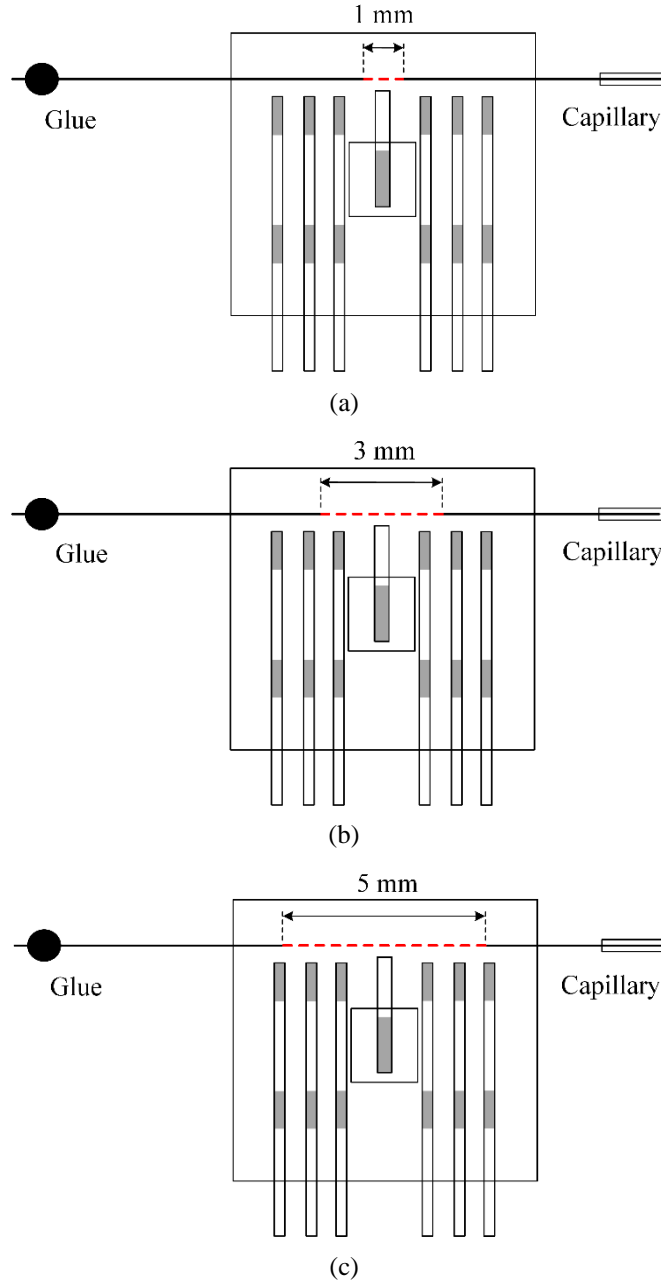


Fig. 6.6. FBG positions for location 1. (a) 1 mm FBG sensor, (b) 3 mm FBG sensor, (c) 5 mm FBG sensor.

6.3.2 Location 1 thermal excitation profiles and test results

The three IGBT modules instrumented with different length FBG sensors were individually operated and the reflected wavelengths recorded. These were then translated to temperature using the calibrated wavelength to temperature (λ - T) relationship. The tests were conducted at various constant current levels and switching frequencies, ranging from 10 A to 50 A in steps of 10 A to represent the in-service thermal conditions, with PWM switching frequencies of 10 Hz, 100 Hz, and 1 kHz being used. The measurements were taken after thermal equilibrium was achieved for each current level.

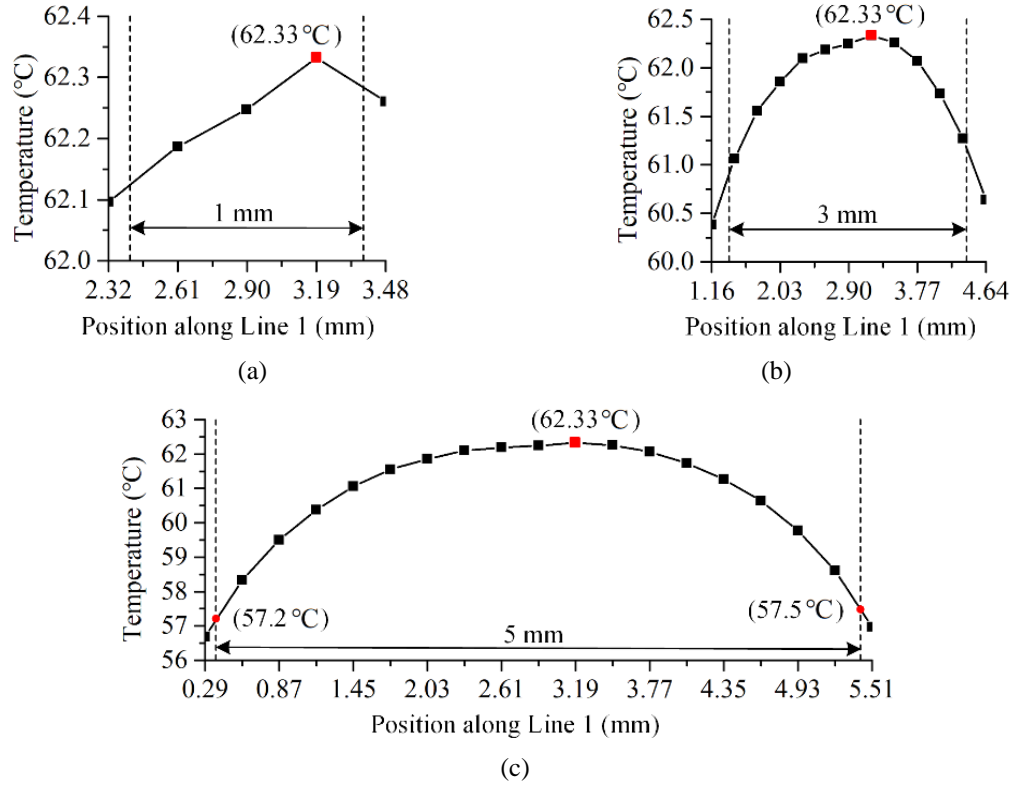


Fig. 6.7. FEA simulated thermal excitation profile at location 1 for: (a) 1 mm FBG sensor, (b) 3 mm FBG sensor, (c) 5 mm FBG sensor.

The average chip temperatures, T_j , of all three cases were shown in Table 6.1. To compare the results while eliminating interference from ambient temperature fluctuations, the measured temperature minus the measured ambient temperature, $T_j - T_a$, was presented in Table 6.2.

The $T_j - T_a$ temperature increase for the three FBG head sizes was compared in Figs. 6.8 to 6.10 at switching frequencies of 1 kHz, 100 Hz, and 10 Hz, respectively. The temperature readings of the three sensor sizes were found to differ by up to ≈ 6.0 °C in identical operating conditions.

The trends in the measurements were consistent across different switching frequencies. The 1 mm sensor consistently reported the highest reading, while the 5 mm sensor recorded the lowest temperature. The 3 mm sensor readings were higher than those of the 5 mm sensor and lower than the readings of the 1 mm sensor. The temperature difference between the three FBG sizes was highest for the 50 A tests. The readings of the 3 mm FBG sensor were 1.6 °C to 1.9 °C lower than those of the 1 mm FBG sensor, while the 5 mm FBG sensor reported 5.2 °C to 6.0 °C lower temperature than the 1 mm FBG sensor.

Table 6.1. Measurements at location 1, 1 kHz, 100 Hz and 10 Hz (°C)

Switching frequency	1 kHz			100 Hz			10Hz		
FBG head length	1 mm	3 mm	5 mm	1 mm	3 mm	5 mm	1 mm	3 mm	5 mm
10 A	27.0	27.0	26.9	26.6	27.1	27.0	26.9	27.3	26.7
20 A	32.4	32.5	31.1	32.8	32.7	30.8	32.6	32.8	30.2
30 A	39.6	39.3	37.7	40.3	39.8	37.7	40.4	39.7	37.4
40 A	49.1	48.8	45.8	49.9	49.7	46.3	50.1	49.7	46.1
50 A	60.1	59.8	55.6	62.0	61.2	56.1	62.4	61.2	55.9

Table 6.2. $T_j - T_a$ at location 1, 1 kHz, 100 Hz and 10Hz (°C)

Switching frequency	1 kHz			100 Hz			10 Hz		
FBG head length	1 mm	3 mm	5 mm	1 mm	3 mm	5 mm	1 mm	3 mm	5 mm
10 A	3.6	3.3	3.3	3.5	3.2	3.4	3.7	2.5	2.4
20 A	9.0	7.8	7.3	9.3	7.9	7.3	9.2	7.9	7.4
30 A	16.2	14.4	13.9	16.7	14.9	14.0	16.7	14.8	12.5
40 A	25.5	23.9	21.6	26.2	24.8	22.5	26.2	24.7	22.8
50 A	36.6	35.0	31.4	38.1	36.2	32.1	38.2	36.6	32.5

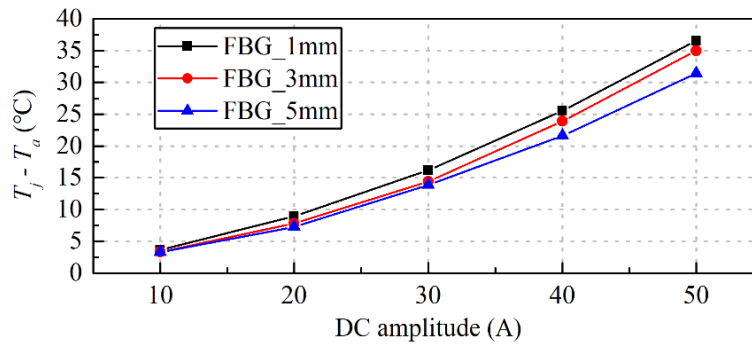


Fig. 6.8. Measurements of location 1 at 1 kHz switching frequency

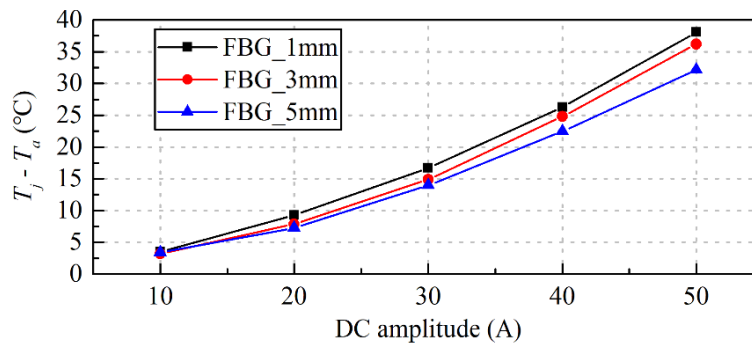


Fig. 6.9. Measurements of location 1 at 100 Hz switching frequency

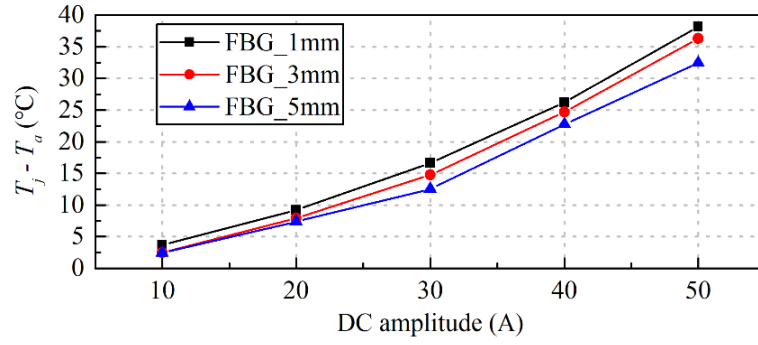


Fig. 6.10. Measurements of location 1 at 10 Hz switching frequency.

6.3.3 IGBT-FBG cases at location 2

This section aims to evaluate the performance of three different sensor lengths, namely 1mm, 3mm, and 5mm, in Location 2, which is represented by Line 2 in Fig. 6.2 (b). The sensors were placed at the same midpoint position in order to ensure consistency of comparison. Fig. 6.11 (a) (b) (c) illustrates the chips instrumented with 1 mm, 3 mm, and 5 mm FBG sensors, respectively, with the sensor heads shown in red. The non-uniform thermal excitation profiles that the FBG sensors were subjected to in-situ are demonstrated in Fig. 6.12. In particular, Fig. 6.12 (c) displays the thermal profile of the 5mm FBG sensor head, which is also presented in Fig. 6.3 (b). As the mid-points of all three head lengths were placed in the same location, the thermal excitation profile that the 3mm FBG sensor was exposed to is the centre 3 mm area of Fig. 6.12 (c), which is shown in Fig. 6.12 (b). Likewise, Fig. 6.12 (a) represents the centre 1mm section of Fig. 6.12 (c) and Fig. 6.12 (b).

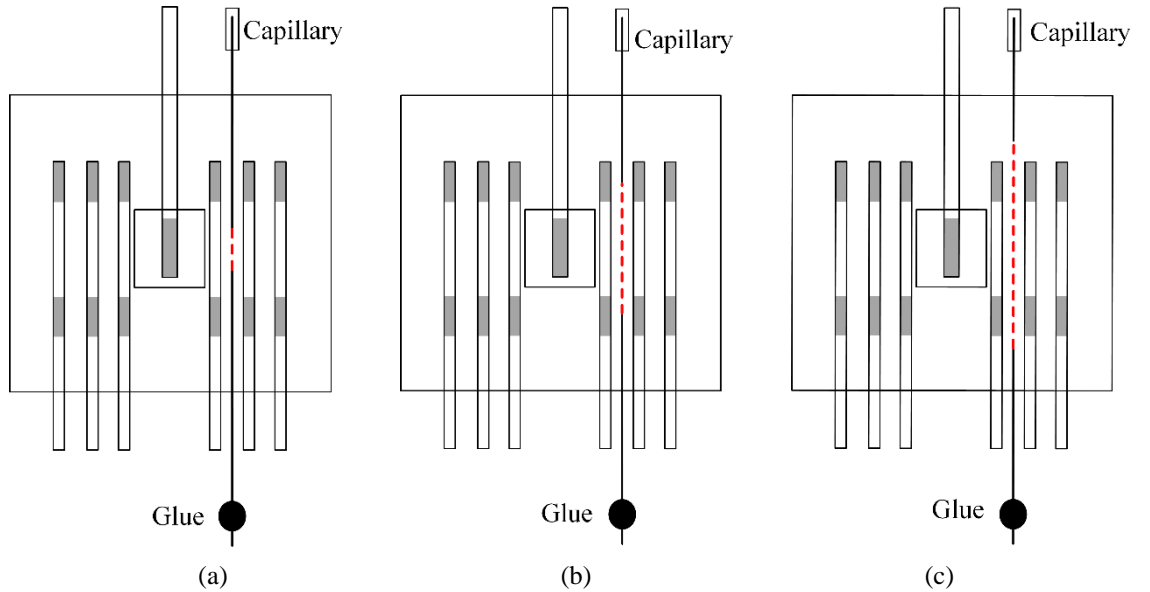


Fig. 6.11. The 3 mm IGBT-FBG case for location 2. (a) 1 mm FBG sensor, (b) 3 mm FBG sensor, (c) 5 mm FBG sensor.

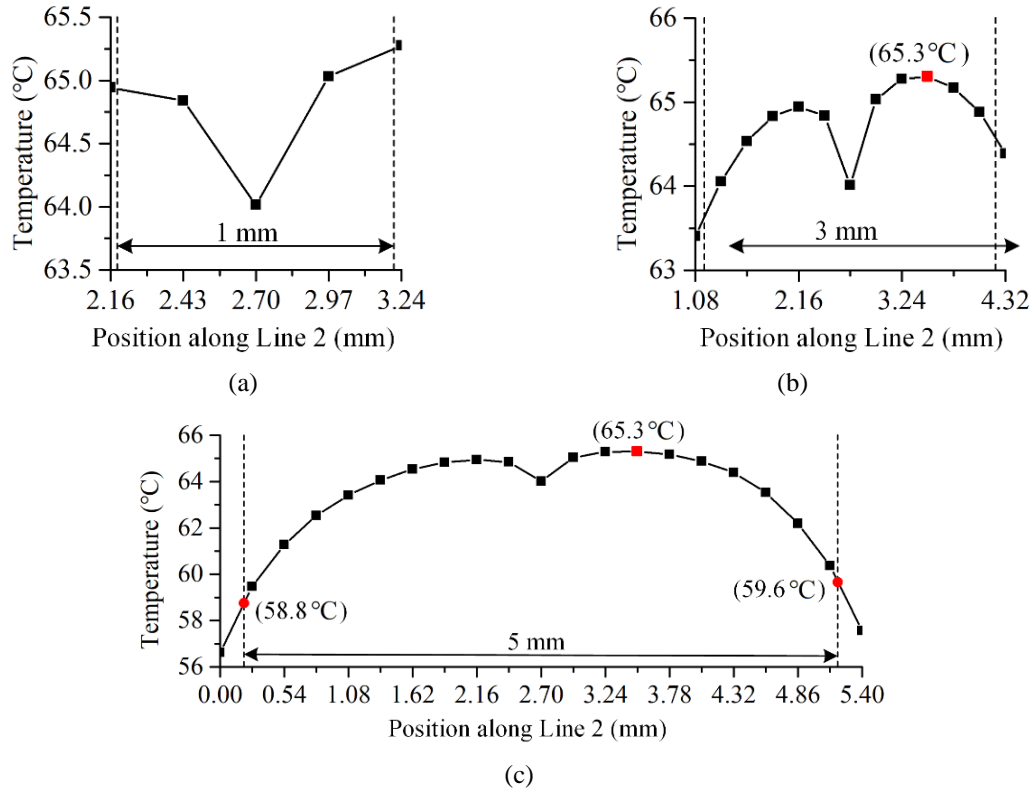


Fig. 6.12. FEA simulated FBG sensors thermal excitation profiles at location 2 for: (a) 1 mm FBG sensor. (b) 3 mm FBG sensor. (c) 5 mm FBG sensor.

6.3.4 Location 2 thermal excitation profiles and test results

The experimental procedure described in section 6.3.2 was consistently applied in these tests, with a constant current of 10 A to 50 A applied in increments of 10 A, and identical switching frequencies considered. The measurements obtained are presented in Table 6.3, and the temperature difference between the measured temperature and the ambient temperature ($T_j - T_a$) is illustrated in Figs. 6.13 to 6.15, with the data also provided in Table 6.4 for clarity. It was observed that there was a difference of up to ≈ 4.0 °C in the temperature sensed by sensors located in the same position under identical conditions.

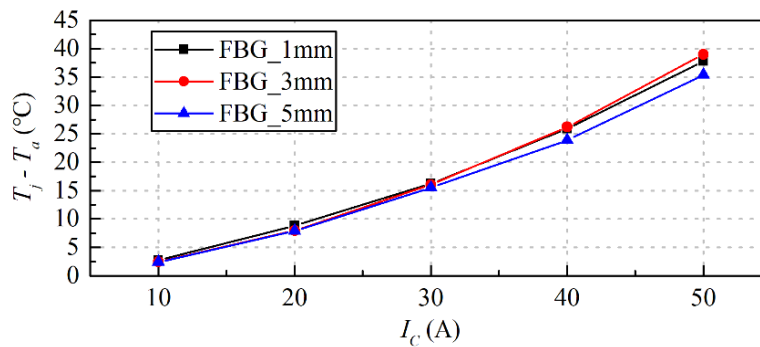


Fig. 6.13. Measurements of location 2 at 1 kHz switching frequency

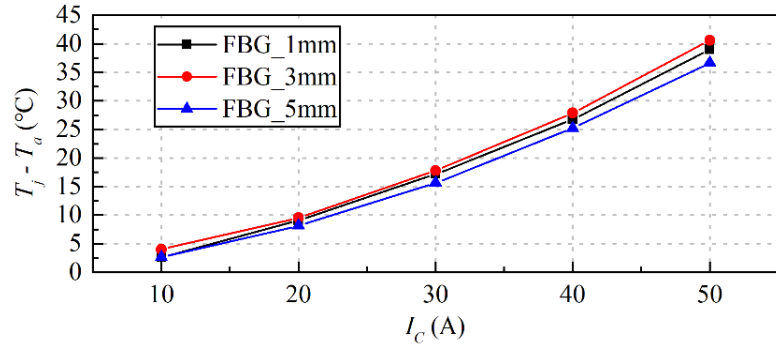


Fig. 6.14. Measurements of location 2 at 100 Hz switching frequency

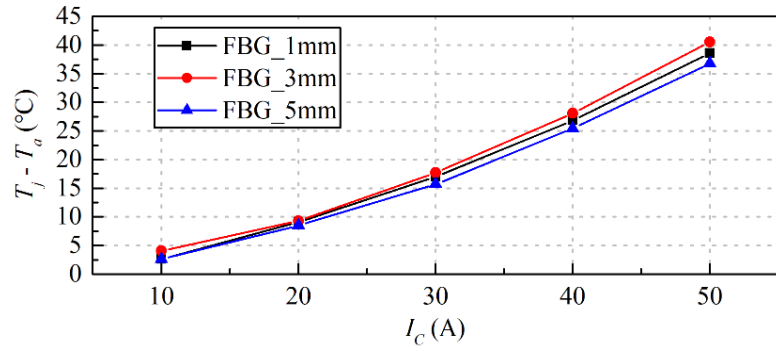


Fig. 6.15. Measurements of location 2 at 10 Hz switching frequency

Table 6.3. Measurements at location 2, 1 kHz, 100 Hz and 10 Hz (°C)

Switching frequency	1 kHz			100 Hz			10 Hz		
FBG head length	1 mm	3 mm	5 mm	1 mm	3 mm	5 mm	1 mm	3 mm	5 mm
10 A	28.0	28.1	28.7	28.4	28.6	29.0	29.0	28.7	29.3
20 A	34.6	33.9	34.8	35.1	34.3	35.2	35.6	34.5	35.5
30 A	42.8	42.3	42.4	43.2	43.1	42.9	43.9	43.3	43.1
40 A	52.5	52.8	51.6	53.1	53.4	52.2	53.8	53.6	53.5
50 A	64.2	64.7	62.7	64.9	65.7	63.7	65.9	66.1	64.4

Table 6.4. $T_j - T_a$ at location 2, 1 kHz, 100 Hz and 10 Hz (°C)

Switching frequency	1 kHz			100 Hz			10 Hz		
FBG head length	1 mm	3 mm	5 mm	1 mm	3 mm	5 mm	1 mm	3 mm	5 mm
10 A	2.7	2.5	2.4	2.6	4.0	2.6	2.6	4.1	2.6
20 A	8.8	8.0	7.9	9.1	9.5	8.2	9.1	9.3	8.5
30 A	16.2	16.1	15.5	17.2	17.8	15.6	17.0	17.7	15.7
40 A	25.9	26.2	23.9	26.7	27.9	25.2	26.8	28.1	25.4
50 A	37.8	39.0	35.4	39.0	40.6	36.6	38.6	40.5	36.8

The 5 mm sensor recorded the lowest temperature readings, while the 3 mm sensor reported the highest temperature readings. This can be attributed to the temperature distribution along line 2 and the length of the corresponding sensor head, as shown in Fig. 6.12. The combination of a particular head length with the corresponding extent of thermal variation along line 2 determines the level of thermal excitation that the sensor will experience in situ. Along line 2, thermal hotspots are present in the bond wire solder areas, with a relatively lower temperature in the space between them where the sensing head is located during testing. Thus, the 3 mm FBG spans the area of thermal variation along line 2, including the two thermal hotspots, and is expected to generally report the highest thermal readings. The 1 mm sensor, located between the two hotspot areas, records a lower temperature. Finally, the 5 mm sensor spans a line 2 area with a thermal variation of $\approx 6.5^\circ\text{C}$ below the hotspot temperature, resulting in the lowest thermal readings.

6.4 Experimental results discussion

The temperature distribution on the surface of the IGBT chip is non-uniform and can exhibit significant thermal gradients, resulting in varying temperature profiles along lines of different orientation and length on the chip surface. Since on-chip FBG sensors are inherently applied along narrow surface line lengths, this has important measurement implications. The sensor can generally be expected to be exposed to non-uniform thermal excitation in-situ, where the extent of excitation non-uniformity is determined by the orientation-specific surface temperature distribution profile characteristics and the sensing head length. Furthermore, it has been shown that for uniform FBGs subjected to pronounced thermal gradients, measurement errors can occur. Therefore, careful consideration of the FBG sensor head length becomes important.

Based on our analysis of the IGBT geometry, we found that for location 1 profiles, which contain a single localized thermal hotspot in the profile centre, the 1 mm FBG provided thermal readings closest to those predicted by FEA simulation. Longer 3 and 5 mm FBG sensors reported values that were $\approx 1.6^\circ\text{C}$ to 1.9°C and $\approx 5.2^\circ\text{C}$ to 6.0°C lower than those of the 1 mm FBG, respectively. This represents a relative deviation of up to 16% from the 1 mm sensor measurement in the case of the 5 mm FBG, which can constitute a prohibitive deviation margin where higher accuracy of hotspot measurement is required. In contrast, for location 2, which has two relatively closely located temperature peaks, the 3 mm FBG generally reports the temperature closest to the FEA predicted hotspot. The 1 mm sensor provides slightly lower readings, reflecting the fact that the midpoint of

location 2, where the sensor is located, exhibits a limited temperature drop. The 5 mm FBG measurements are ≈ 3.6 °C to 4.0 °C lower than those of the 3 mm FBG, demonstrating that a long FBG head in this orientation reports readings somewhat closer to those of shorter FBGs, as driven by the nature of the location 2 thermal profile.

These results indicate that the selection of the sensing head length to achieve effective localized hotspot measurement is crucial and fundamentally defined by the interplay between the actual thermal hotspot location and the related surrounding surface temperature distribution characteristics. In general, a shorter FBG head length can intrinsically provide a more credible measurement, assuming it can be located sufficiently close to the localized hotspot being monitored, which can be challenging in practical applications. In some locations (e.g. location 2 in this study), the application of a longer FBG sensing head can provide optimal results and would enable less stringent installation requirements in terms of positioning. However, very long head sizes that are comparable to the chip surface dimension are generally expected to result in the highest level of hotspot temperature reading deviation and inaccuracy.

6.5 FBG reflected spectrum distortion

In section 6.3 of the study, a significant deviation is reported in the 5 mm FBG measurement at location 1. This section aims to investigate the cause of this deviation when a long FBG sensor is exposed to a region with a large thermal gradient, resulting in significant non-uniformity in thermal excitation. The reflected wavelengths of individual sensors are measured and compared to analyze the effect of surface temperature variation on measurement as a function of head size in this application.

To assess uneven thermal excitation, the reflected spectra of the IGBT installed with 1 mm, 3 mm, and 5 mm FBGs were recorded in three different conditions. These include 1) at ambient temperature, 2) in a thermal chamber at a stable temperature of 50 °C, and 3) on the test rig with IGBT current heating the chip to 50 °C (defined using 1 mm FBG reading). The first two conditions have a homogeneous temperature across the entire chip geometry, with no thermal gradients present. However, the third condition exhibits large thermal gradients and localized temperature variation on the chip surface.

Fig. 6.16, 6.17, and 6.18 show the recorded spectra of the 1 mm, 3 mm, and 5 mm FBGs, respectively, in the three different excitation scenarios. The results obtained demonstrate the phenomenon of non-uniform thermal excitation in the long FBG head when a significant thermal gradient is present, leading to deviations in thermal

measurements.

The recorded spectra of the 1 mm FBG in the three different excitation scenarios show that the reflected spectrum shape remains similar across all three scenarios. Therefore, uneven thermal excitation resulting from IGBT current flow does not affect the 1 mm FBG head measurements negatively. Similar results are observed for the measured spectra of the 3 mm FBG, indicating that the reflected spectrum shape is maintained across all three scenarios.

However, the measured spectra of the 5 mm FBG exhibit a distortion in the reflected spectrum with the presence of non-uniform thermal excitation resulting from IGBT current flow. Although the spectrum shape at uniform thermal excitation (i.e., ambient and thermal chamber) is identical, non-uniform excitation results in an alteration of the spectrum and an overall reduction in reflected wavelength value. This effect causes the thermal measurement deviation observed in Section 6.3 tests. Thus, the measurement deviation observed in the 5 mm FBG is due to the non-uniform thermal excitation resulting from the large thermal gradient at location 1, combined with the long FBG head in this application. Moreover, the thermal sensing of the long FBG sensor of thermal gradient is not the average temperature due to the measurement deviation caused by the spectrum alteration.

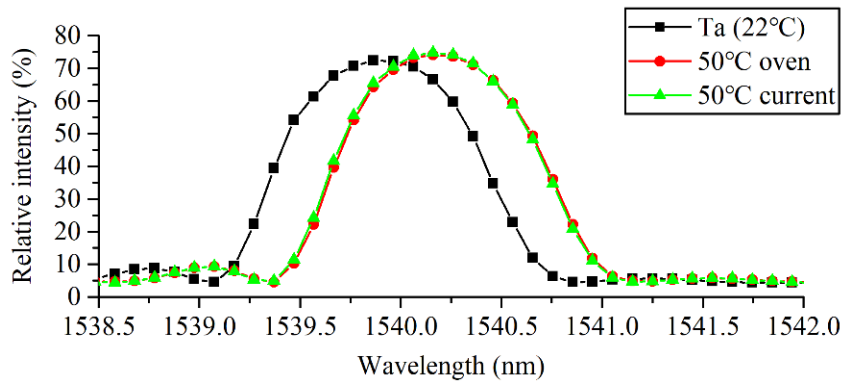


Fig. 6.16. Measured spectra of the 1 mm FBG sensor

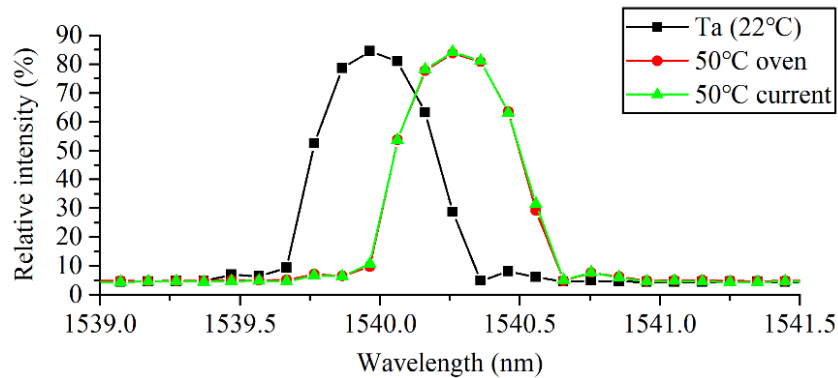


Fig. 6.17. Measured spectra of the 3 mm FBG sensor

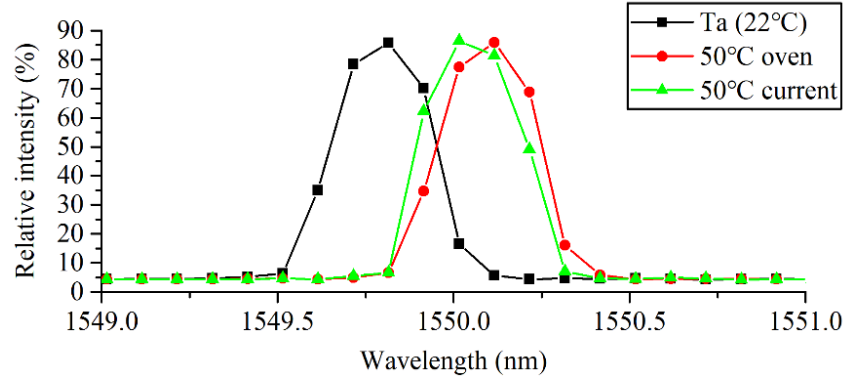


Fig. 6.18. Measured spectra of the 5 mm FBG sensor

6.6 Summary

This chapter evaluates the impact of the length of the FBG sensor head on the thermal sensing performance of an IGBT power module, using on-chip direct sensing with FBG technology. A specialized testing system and an IGBT FEA thermal model are utilized to investigate the thermal behaviour of different-sized FBG sensors within the IGBT power module's rated operating envelope. The experimental and model characterization of the IGBT indicates a non-uniform temperature distribution on the chip's surface, which creates a trade-off between FBG size selection and the surface temperature distribution characteristics of the hotspot location.

Short FBGs offer precise readings of localized IGBT surface hotspots, but they require accurate hotspot location determination and sensor placement. Longer FBGs can provide dependable thermal readings in locations with less severe thermal gradients, and provide advantages in terms of placement and ease of installation. However, very long FBGs experience changes in the reflected wavelength when subjected to non-uniform thermal excitation, making them less suitable for IGBT on-chip thermal sensing applications due to the large thermal gradients these devices may exhibit under practical loads.

This findings of this chapter enhance the understanding of the requirements for effective FBG sensing in power electronic devices and further demonstrate the potential of FBG sensors for practical on-chip implementation, which enables improved awareness of in-service thermal conditions beyond conventional sensing techniques.

Chapter 7: Comparison of V_{CE} and FBG based Junction Temperature Acquisition Technologies

Accurate evaluation of junction temperature is critical for ensuring the reliability and performance of IGBT power modules and it can also be a useful tool for condition monitoring. This chapter presents an analysis of different methods for junction temperature evaluation in IGBT power modules, focusing on voltage-based approaches (V_{CE} and ΔV_{CE}) and contact temperature measurement techniques using FBG sensors. V_{CE} is a typical temperature sensitive electrical parameter, which has been studied and applied for the junction temperature evaluation of the IGBT power module, but actual V_{CE} is very device dependent. The study investigates the strengths, limitations, and potential sources of error associated with each method. The results demonstrate that V_{CE} -based evaluation is susceptible to measurement errors caused by voltage noise and discrepancies in voltage drops across terminals and bond wires. The ΔV_{CE} -based evaluation shows promise in mitigating the influence from terminals and bond wires but introduces a new interference caused by temperature variations across different V_G values. In contrast, FBG sensors offer a reliable and accurate alternative for real-time temperature monitoring of IGBT power modules. The comparative analysis provides valuable insights for selecting the most suitable method based on application requirements. The findings contribute to the advancement of thermal management strategies of IGBT power modules in various power electronics applications.

7.1 $V_{CE} - T_j - I_C$ and $\Delta V_{CE} - T_j - I_C$ relationships calibration

Because the on-state voltage V_{CE} changes with junction temperature T_j and collector current I_C , the $V_{CE} - T_j - I_C$ relationship of each IGBT needs to be calibrated. In this set of experiments, to achieve this, the chip temperature was regulated using a digital thermal chamber. A current impulse with an amplitude of I_C was passed through the IGBT chip, and the corresponding V_{CE} was recorded. The duration of the current impulse was determined based on a FEA model to ensure that the temperature rise caused by conduction loss is insignificant. By repeating this process at different current levels and temperature levels, an accurate 3D $V_{CE} - T_j - I_C$ relationship of the IGBT can be established.

7.1.1 Simulation of temperature rise caused by current impulses

The objective of the simulation is to determine an appropriate duration for the current

impulse that ensures the junction temperature rise caused by conduction power loss remains within an acceptable range.

The FEA model of the IGBT power module is introduced in Chapter 3. The transient thermal impedance of each layer and the whole module were analysed based on a Cauer thermal circuit as introduced in Chapter 3.3. Based on the analysis of the transient thermal impedance, some geometries and materials' properties were optimized to make the FEA model fitting more accurate to the transient thermal parameters provided by the IGBT's commercial specifications. The FEA model of the IGBT power module shown in Fig. 3.13 is redrawn here as Fig. 7.1 for illustration purpose. The half module model is finely meshed for the chip and the bond wires components, while the remaining components are coarsely meshed with a high element growth rate assigned.

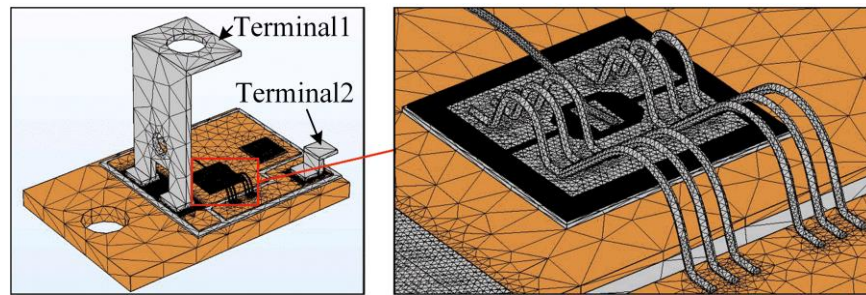


Fig. 7.1. The mesh detail of the IGBT half model

Appropriate thermal boundaries are assigned to the model as introduced in Chapter 3.5.2. The h value for the baseplate bottom surface is set to $3800 \text{ W}/(\text{m}^2 \cdot \text{K})$ to represent equivalent heat dissipation as with the heat sink, and to ensure consistent thermal distribution within the IGBT chip. The h values for other surfaces are set to $5 \text{ W}/(\text{m}^2 \cdot \text{K})$.

The simulation aims to estimate the maximum duration of the current impulse at rated current (50 A) to be employed during V_{CE} calibration. A zero-initial step current with an amplitude of 50 A is applied to terminal1, while terminal2 is grounded. The electrical conductivity of the IGBT chip is set to a constant value that produces a 2 V on-state voltage drop from the bottom surface (collector) to the upper surface (emitter) of the IGBT chip under a 50 A current. The resulting transient thermal response of the IGBT is presented in Fig. 7.2.

The predicted temperature exhibits a rise of approximately 0.5°C around $38 \mu\text{s}$ and 1°C around $77 \mu\text{s}$. Thus, to control the calibration error within 1°C , the V_{CE} should be measured within $77 \mu\text{s}$ of the current impulse.

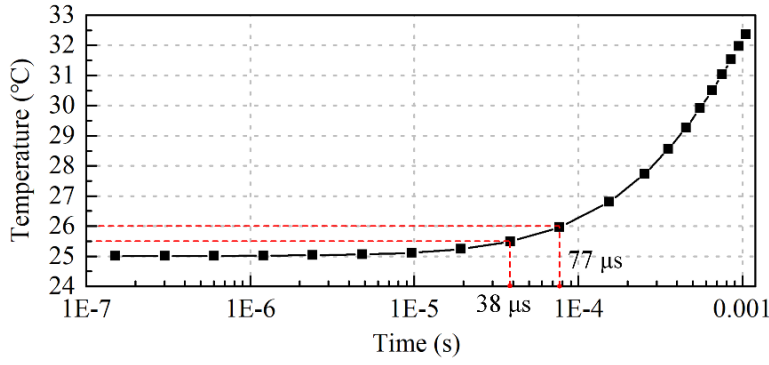


Fig. 7.2. Thermal response of the IGBT chip in 1 ms

7.1.2 $V_{CE} - T_j - I_C$ calibration test

A test rig was constructed as introduced in Chapter 4.4 to perform the calibration of the $V_{CE} - T_j - I_C$ relationship for each IGBT power module. The circuit diagram used for calibration is shown in Fig. 4.14 (redrawn here as Fig. 7.3). The alternate conduction of auxiliary IGBTs generated current impulses to the IGBT_DUT, while ensuring that the current flowing through the power supply and the load R_L was never abruptly interrupted. It was designed to prevent voltage impulses that could arise due to parasitic inductive components in the circuit and load. The control timing diagram of the three IGBTs is shown in Fig. 4.15. Since the gate voltage of the IGBT_DUT is a constant voltage, the IGBT_DUT keeps on during the calibration experiment and there is no switching power loss.

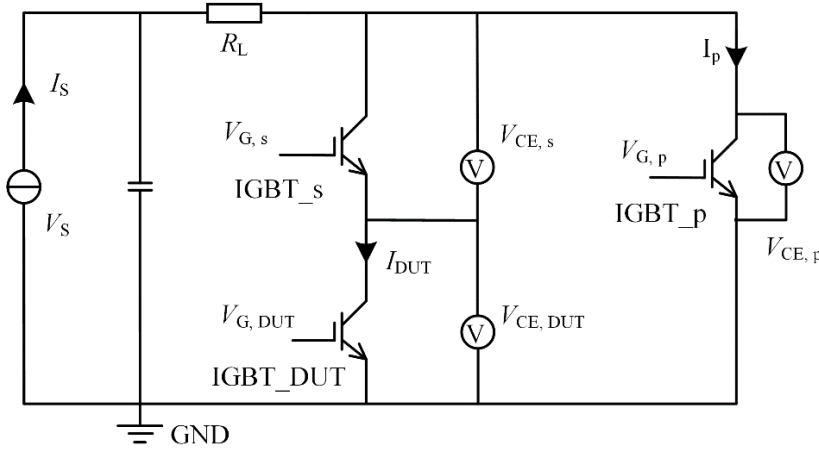


Fig. 7.3. Circuit diagram of the $V_{CE} - T_j - I_C$ relationship calibration test rig

In a specific case where the time duration of the current impulse was set to 50 μ s, an example of the recorded $V_{CE, DUT}$ and I_{DUT} under the conditions of 15 V_{G, DUT}, 40 A I_{DUT} , and 50 °C T_j is illustrated in Fig. 7.4. To determine the precise time required for the current to stabilize, the 43 μ s period bounded by the red dash block in Fig. 7.4 is fitted using the exponential function described by Equation 7.1.

$$I_{DUT} = 40.47 - 5.99 \cdot e^{-\frac{t}{1.43 \times 10^{-5}}} \quad (7.1)$$

The curve fitting results are presented in Fig. 7.5, showing an R -square value of 0.9987. The time constant (τ) is calculated to be 14.3 μs , which indicates that the I_{DUT} reaches a steady state within three times the time constant, which amounts to 42.9 μs .

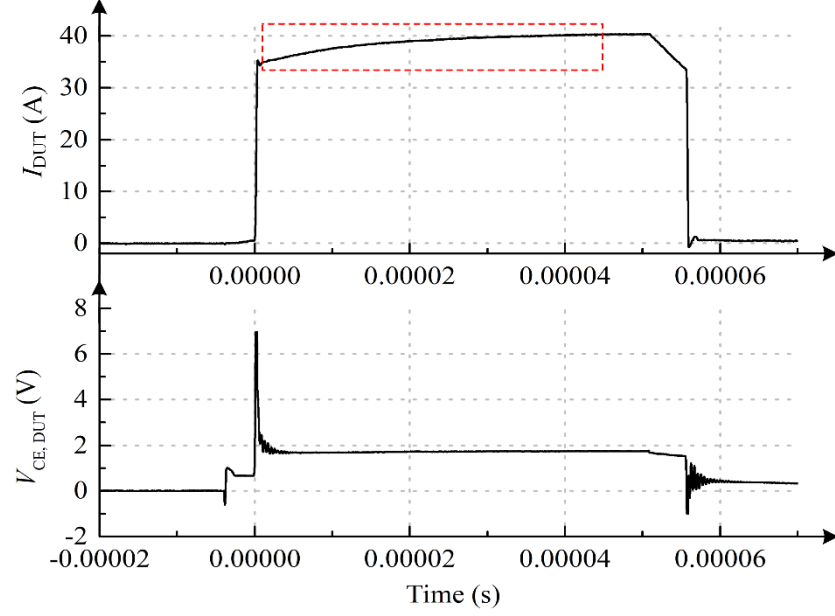


Fig. 7.4. An example of recorded $V_{CE,DUT}$ and I_{DUT} under a certain condition

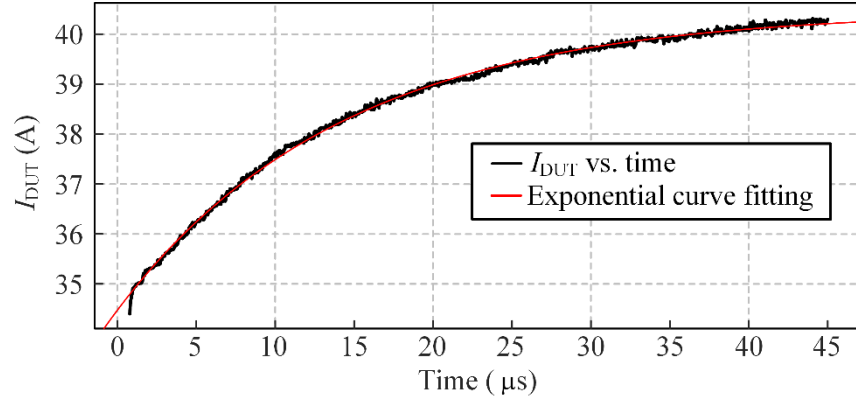


Fig. 7.5. Exponential curve fitting of the I_{DUT}

Building upon the discussion in Chapter 7.1.1, the $V_{CE,DUT}$ measurements obtained between 40 μs and 45 μs are selected and averaged to represent the measured $V_{CE,DUT}$ at each corresponding temperature and current condition. The time width of the current impulse is set to 50 μs .

The temperature rise caused by the current pulse is neglected, so that the junction temperature for this calibration point is regarded as 50 $^{\circ}\text{C}$. This assumption introduces an evaluation error of approximately -0.5 $^{\circ}\text{C}$. Furthermore, a slight error is observed in the current compared to the set value of 40 A for this calibration point. The average current

value during the 40 μ s to 45 μ s period is measured to be 40.17 A. The 0.17 A deviation in current results in a positive error of up to 4.6 mV in the V_{CE} , which corresponds to approximately +3 $^{\circ}$ C based on the current sensitivity and temperature sensitivity discussed in Chapter 7.1.3.

Three values of $V_{G,DUT}$ (12 V, 15 V and 18 V) were tested. Additionally, six temperature levels ranging from 25 $^{\circ}$ C to 150 $^{\circ}$ C with a step of 25 $^{\circ}$ C were examined, and nine current levels ranging from 5 A to 45 A with a step of 5 A were investigated.

7.1.3 V_{CE} - T_j - I_C relationship

The V_{CE} - T_j - I_C relationship under 15 V $V_{G,DUT}$ is presented in Fig. 7.6. The patterns observed in the relationships under 12 V and 18 V $V_{G,DUT}$ are almost identical. To provide a clearer visualization, Fig. 7.6 is redrawn as Fig. 7.7. It can be observed in Fig. 7.7 that V_{CE} increases with increasing current. However, the correlation between V_{CE} and temperature differs significantly at different current levels. When the current is below 15 A, V_{CE} shows a negative correlation with temperature, while for currents above 20 A, a positive correlation is observed. Interestingly, V_{CE} remains reasonably stable regardless of temperature variations within the range of 15 A to 20 A.

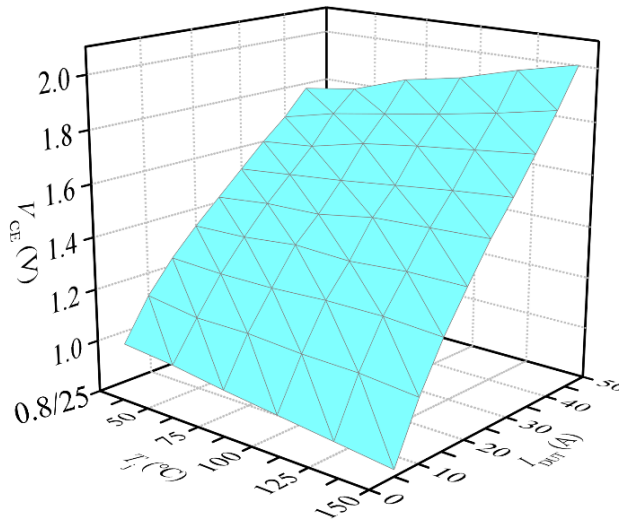


Fig. 7.6. 3-D V_{CE} - T_j - I_C relationship under 15 V $V_{G,DUT}$

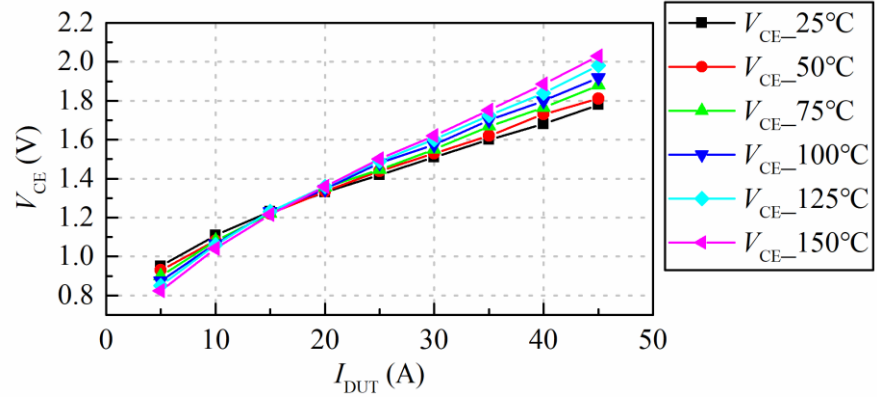


Fig. 7.7. $V_{CE} - T_j - I_C$ relationship curves under 15 V $V_{G,DUT}$

Due to the unclear correlation between V_{CE} and temperature within the current range of 15 A to 20 A, this portion of data is not suitable for constructing the correlation function and temperature evaluation. Consequently, this study omits the data below 25 A but focuses only on the data at four current levels (30 A, 35 A, 40 A, and 45 A) for constructing the $V_{CE} - T_j - I_C$ relationship and subsequent data analysis. Fig. 7.8 shows the voltage current relationship with the omitted data. Moreover, when using the temperature as x-axis, Fig. 7.8 can be redrawn as Fig. 7.9.

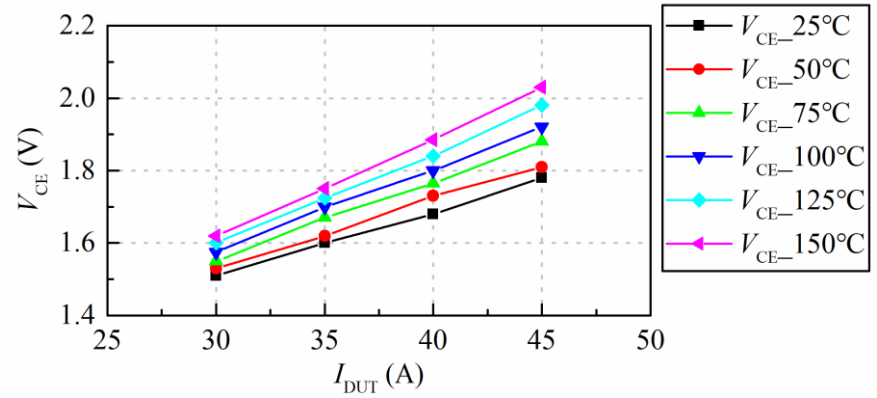


Fig. 7.8. $V_{CE} - I_C$ relationship curves in large current ranges

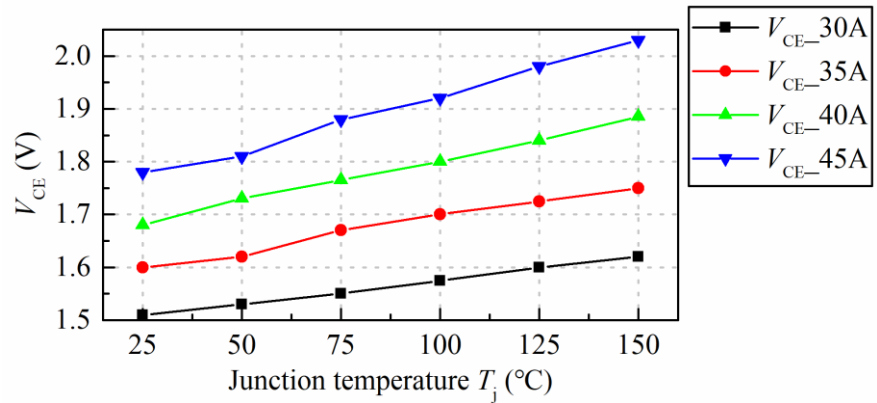


Fig. 7.9. $V_{CE} - T_j$ relationship curves in large current ranges

Fig. 7.8 illustrates the strong linear relationship between V_{CE} and collector current, with current sensitivities of 17.8 mV/A at 25 °C and 27.3 mV/A at 150 °C. The current sensitivities across temperatures ranging from 25 °C to 150 °C fall within the range of 17.8 mV/A to 27.3 mV/A. Additionally, Fig. 7.9 demonstrates a robust linear relationship between V_{CE} and junction temperature, with temperature sensitivities ranging from 0.9 to 2.1 mV/°C, corresponding to currents of 30 A and 45 A, respectively.

The $V_{CE} - T_j - I_C$ relationship within the 30 A to 45 A current range of can be effectively fitted using a polynomial function incorporating the first power of temperature and the second power of current. For example, the $V_{CE} - T_j - I_C$ relationship depicted in Fig. 7.8 and Fig. 7.9 can be described by Equation 7.2. The fitting yields a high R -square value of 0.9974, indicating that T_j can be expressed as a function of V_{CE} and I_C . This serves as the foundation for the V_{CE} -based junction temperature evaluation discussed in Chapter 7.2. Similarly, the $V_{CE} - T_j - I_C$ relationships can be fitted when the gate voltage V_G is 12 V and 18 V.

$$V_{CE} = 1.115 - 0.001437T_j + 0.01069I_C + 7.749 \times 10^{-5}T_j \cdot I_C + 6.667 \times 10^{-5}I_C^2 \quad (7.2)$$

7.1.4 $\Delta V_{CE} - T_j - I_C$ relationship

V_{CE} exhibits variations with respect to the gate voltage V_G . A method proposed by previous research is employed in this study to evaluate the junction temperature in online applications by utilizing the relationship between the difference in V_{CE} under different V_G conditions and the junction temperature.

In this study, three different gate voltages (12 V, 15 V, and 18 V) were tested. Consequently, under specific current and temperature conditions, ΔV_{CE1218} , the difference between the V_{CE} values obtained at 12 V V_G and 18 V V_G , for example, is calculated. These differences are denoted as ΔV_{CE1215} , ΔV_{CE1218} , and ΔV_{CE1518} , respectively. Fig. 7.10 illustrates the 3D map of the $\Delta V_{CE1218} - T_j - I_C$ relationship, which can be effectively fitted using Equation 7.3. The polynomial fitting for this relationship yields a high R -square value of 0.9935, enabling the expression of the junction temperature as a function of ΔV_{CE1218} and I_C . Similarly, ΔV_{CE1215} can also be expressed as functions of T_j and I_C , with a fitting R -square of 0.9802. However, it was observed that the fitting R -square value for ΔV_{CE1518} is only approximately 0.92. Consequently, ΔV_{CE1518} is excluded from further analysis.

$$\Delta V_{CE1218} = 0.2075 - 0.000943T_j - 0.0082I_C + 5.486 \times 10^{-5}T_j \cdot I_C + 0.0002I_C^2 \quad (7.3)$$

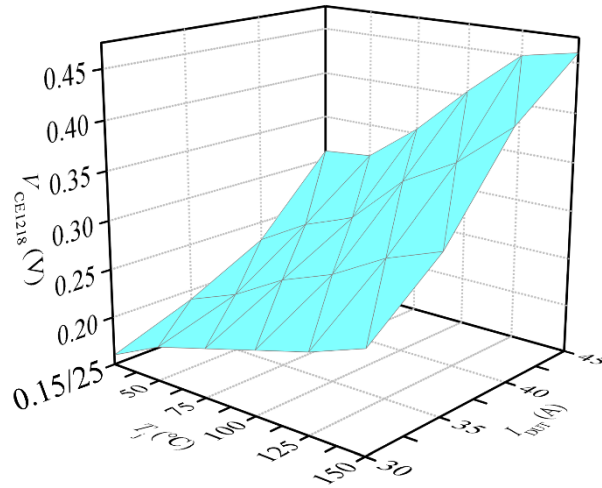


Fig. 7.10. $\Delta V_{CE1218} - T_j$ relationship curves in large current ranges

7.2 Comparison of junction temperatures acquired based on V_{CE} , FBG sensor, and thermal camera

Chapter 7.1 established three $V_{CE} - T_j - I_C$ relationships under different gate voltage conditions and three $\Delta V_{CE} - T_j - I_C$ relationships, enabling the evaluation of junction temperature based on V_{CE} , I_C , and V_G . In this section, the evaluation of the junction temperature based on V_{CE} and ΔV_{CE} are compared with the chip temperature measured using FBG sensors and a thermal camera.

7.2.1 Test rig

Fig. 7.11 shows the schematic circuit of the test rig designed to supply a rated DC current (50 A DC) for heating the commercial IGBT test module (Semikron SKM50GB12T4). The DC power source is rated at 5 kW / 50 A, and a resistance load of 0.67Ω is utilized. The IGBT power module used in the experiment was fitted with an FBG sensor. It was controlled by a DC voltage to maintain an on-state during the tests.

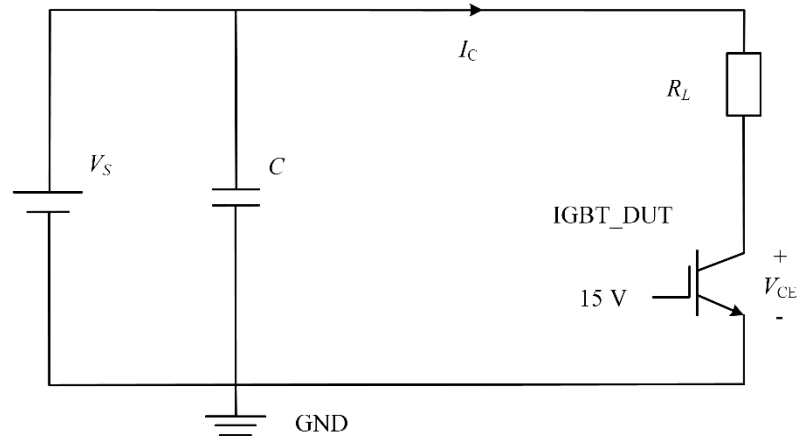


Fig. 7.11. Test rig electric circuit diagram.

A commercial interrogator unit (SmartScan04) interfaced with the FBG sensor installed on the IGBT power module, enabling the interrogation and recording of the reflected wavelength from the sensor. By utilizing the calibration characteristics of the FBG, the recorded wavelength can be translated into corresponding temperature values.

For thermal reference, a Fluke Ti10 thermal camera was employed to capture the thermal map of the IGBT chip. However, due to the low emissivity of the IGBT chip surface (with the silver solder layer), the temperature of the chip surface was unable to be directly measured using the thermal camera. To increase the surface emissivity and obtain accurate temperature readings, the IGBT surface was coated with MOTIP black paint as introduced in Chapter 4.3.

The collector-to-emitter voltage V_{CE} was directly measured using a high-bandwidth voltage probe with a measurement bandwidth of 25 MHz and DC voltage accuracy of $\pm 2\%$. The collector current I_C was measured using a current probe with a bandwidth of 100 MHz and sensitivity of 1 mA/div.

Since the V_{CE} -based temperature evaluation method was not suitable for currents between 10 A and 25 A, as discussed in Chapter 7.1.3, the experiment was conducted within the current range of 30 A to 45 A, with an increment of 5 A. The IGBT was kept at each current level for 30 minutes to ensure that the chip temperature reached thermal equilibrium. Subsequently, V_{CE} was measured using a differential voltage probe connecting with an oscilloscope, the reflected wavelength from the FBG sensor was recorded, and the chip's surface temperature distribution was captured using the thermal camera.

7.2.2 Junction temperature measured by the FBG sensor and thermal camera

During the tests conducted at four different current values, measurements from the FBG sensor and the thermal camera were recorded. The FBG sensor provides a thermal reading specifically for Area1, as depicted in Fig. 5.3. Since the measured point has a small area, the FBG sensor reading represents a single temperature value. In contrast, the thermal images captured by the thermal camera offer comprehensive thermal gradient information of the IGBT chip. Fig. 7.12 shows an example of the thermal image taken by the thermal camera when $I_C = 45.4$ A and $V_G = 15$ V.

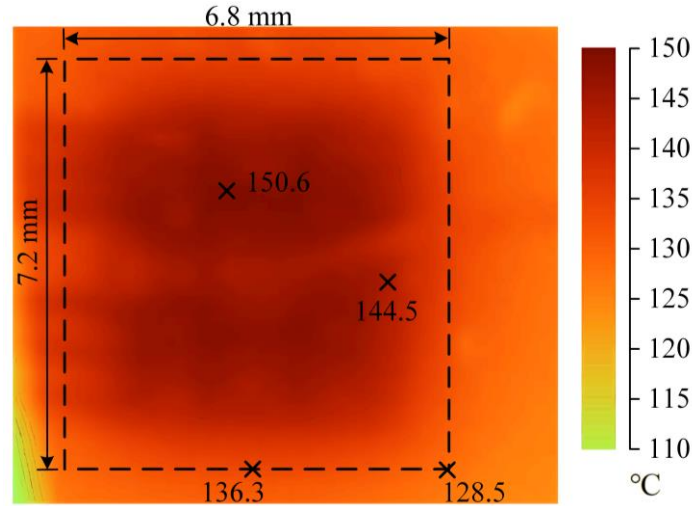


Fig. 7.12. Thermal image of the IGBT chip

The maximum temperature is 150.6 °C, which is the temperature of a point on the bond wires. The maximum temperature of the chip will be smaller than 150.6 °C but cannot be directly sensed since the bond wires obstruct the line of sight – this is a considerable detriment to chip surface temperature measurement using a thermal camera, as a clean line of sight is generally impossible to ensure across the entire chip surface in geometries and designs utilizing bond wires; this results in unreliable measurements in locations/areas on the chip surface that are obstructed (i.e. those obscured by bond wires). The thermal camera readings show 144.5 °C displayed for Area1 and a minimum temperature about 128.5 °C at the chip corner.

The values displayed for Area1 in the thermal images are used as reference values for comparison with FBG readings. The thermal readings obtained from the thermal camera and the FBG sensor are presented in Table 7.1.

Table 7.1. FBG Sensor and Camera Measured I_C and T_j

I_C	30.4 A	35.7A	40.6A	45.4A
FBG, $T_{j_V_{G_12V}}$	99.4	116.8	133.6	152.4
FBG, $T_{j_V_{G_15V}}$	97.6	113.8	129.0	143.9
FBG, $T_{j_V_{G_18V}}$	96.9	112.5	127.1	143.2
Camera, $T_{j_V_{G_12V}}$	100.0	117.5	134.3	153.3
Camera, $T_{j_V_{G_15V}}$	98.1	114.5	129.7	144.5
Camera, $T_{j_V_{G_18V}}$	97.3	113.0	127.5	143.7

The thermal camera readings demonstrate that lower gate voltages correspond to higher temperatures. This can be attributed to the fact that with a smaller driving voltage, the IGBT

experiences a higher on-voltage when the same current value flows through it, resulting in greater heat loss and therefore higher temperatures.

The thermal readings obtained from the FBG sensor closely align with those from the thermal camera. Some of the FBG sensor readings exhibit difference with camera readings, with the maximum measurement difference reaching -0.9 °C.

7.2.3 V_{CE} - T_j - I_C relationship based junction temperature evaluation

Section 7.1.3 outlines the calibrated V_{CE} - T_j - I_C relationships under different gate voltages. The V_{CE} - T_j - I_C relationship under 15 V gate voltage is expressed as Equation 7.2 as an example. Consequently, T_j can be calculated based on measured V_{CE} and I_C . The measured current values, voltage values, and the calculated junction temperatures are listed in Table 7.2. The $T_{j_V_{G_18V}}$ at 30.4 A is removed since the reading is considered inaccurate.

Table 7.2. Measured V_{CE} , I_C , and V_{CE} based Calculated T_j

I_C	30.4 A	35.7A	40.6A	45.4A
$V_{CE_V_{G_12V}}$	1.70 V	1.92 V	2.18 V	2.46 V
$V_{CE_V_{G_15V}}$	1.56 V	1.70 V	1.89 V	2.07 V
$V_{CE_V_{G_18V}}$	1.47 V	1.61 V	1.74 V	1.91 V
$T_{j_V_{G_12V}}$	71.9 °C	111.0 °C	149.4 °C	179.6 °C
$T_{j_V_{G_15V}}$	63.6 °C	89.1 °C	137.0 °C	159.7 °C
$T_{j_V_{G_18V}}$	27.4 °C	80.3 °C	111.5 °C	156.4 °C

The evaluated temperature values shown in Table 7.2 also exhibit that lower gate voltages correspond to higher temperatures – a same pattern compared to those shown in Table 7.1 measured by the thermal camera, which proves the feasibility of this V_{CE} based temperature evaluation method. However, significant errors between the temperature values in Table 7.1 and Table 7.2 implies the inaccuracy of the V_{CE} based temperature evaluation.

Due to the presence of inherent noise in the V_{CE} signals of the test rig with an amplitude of approximately 0.01 V, the voltage measurements are only accurate to be the nearest 0.01V. However, considering the V_{CE} temperature sensitivities ranging from 0.9 mV/°C to 2.1 mV/°C as discussed in Chapter 7.1.3, it implies that the 0.01 V noise corresponds to a temperature noise of 5 to 10 °C in the evaluated temperature. This evaluation error is inherent to this method. Moreover, it indicates that a 0.01 V change in V_{CE} will equate to a

change in temperature estimation of 5 to 10 °C. The high temperature sensitivities impose rigorous requirements on the accuracy and anti-interference capability of voltage measurements, which are practically challenging to achieve.

Furthermore, the measured V_{CE} primarily encompasses the voltage drop across three components: the IGBT, the six bond wires, and the two aluminum terminals. During the calibration conducted in the thermal chamber, the entire module maintained a homogeneous temperature. However, in the current heating test of the IGBT, the aluminum terminals had noticeably lower temperatures, while the bond wires had higher temperatures. The discrepancy in the voltage drops across the terminals and bond wires, compared to those observed during the calibration process, contributes to the substantial measurement errors. It has also been reported that the general error associated with this V_{CE} -based temperature evaluation method can be as high as 30 °C [8] [36].

In addition, although the 3D surface fitting equations, e.g. Equation 7.2, show high R -square of more than 0.99, this fitting link brings error in the temperature evaluation, too.

7.2.4 ΔV_{CE} - T_j - I_C relationship based junction temperature evaluation

Chapter 7.1.4 outlines the calibrated ΔV_{CE} - T_j - I_C relationships. The ΔV_{CE1218} - T_j - I_C relationship is expressed as Equation 7.3 as an example. Consequently, T_j can be calculated based on ΔV_{CE} and I_C .

The measured current values, voltage differences, and the calculated junction temperatures are listed in Table 7.3. By subtraction, the parts of the V_{CE} that the terminals and the bond wire take up can be eliminated. Therefore, ΔV_{CE1218} and ΔV_{CE1215} are the difference of the true IGBT chip on-state voltages.

Table 7.3. ΔV_{CE} based Calculated T_j

I_C	30.4 A	35.7A	40.6A	45.4A
ΔV_{CE1218}	0.23 V	0.31 V	0.44 V	0.55 V
ΔV_{CE1215}	0.14 V	0.22 V	0.29 V	0.39 V
$T_{j_}\Delta V_{CE1218}$	111.7	138.2	183.5	198.7
$T_{j_}\Delta V_{CE1215}$	88.3	157.1	176.9	225.1

However, the junction temperature values evaluated based on ΔV_{CE} still exhibit significant positive errors when compared to the measurements from the thermal camera.

This discrepancy arises because during the calibration process in the thermal chamber, the V_{CE} at different V_G values was measured at the same junction temperature; however, during the current heating test, the junction temperature varied across different V_G values. For example, as shown in Table 7.1, the actual junction temperatures at 45.4 A corresponding to V_G values of 12 V, 15 V, and 18 V are 153.3 °C, 144.5 °C, and 143.7 °C, respectively. Therefore, the difference in V_G is no longer the sole factor influencing V_{CE} , as the temperature difference has amplified the ΔV_{CE} . As a result, positive errors occur in the temperature evaluated based on the inflated ΔV_{CE} .

These positive errors caused by the temperature difference can be mitigated by optimizing the measurement process of V_{CE} at different V_G values during the current heating test. For instance, the V_G can be momentarily changed to 12 V for several microseconds, during which the V_{CE} measurement is conducted. This approach aims to minimize the interference resulting from variations in junction temperature.

7.3 Summary

In this study, a comparison of different methods for evaluating the junction temperature of IGBT power modules have been conducted. Specifically, the effectiveness of V_{CE} -based and ΔV_{CE} -based evaluation, were compared to temperature measurements obtained from a thermal camera and FBG sensors.

The findings highlight the inherent limitations and potential measurement errors associated with V_{CE} -based evaluation. While this method can provide reasonable estimation, its accuracy heavily relies on precise voltage measurements and accurate V_{CE} to temperature calibration function relationship. Moreover, the discrepancy in voltage drops across terminals and bond wires during the current heating test significantly contribute to measurement errors. The evaluation based on ΔV_{CE} shows promise in mitigating the influence from terminals and bond wires. However, it introduces a new interference caused by temperature variations across different V_G values. Shortening the change time of V_G during the V_{CE} measurement process may help minimize temperature fluctuations and alleviate this interference., however in practical application V_{CE} -based temperature evaluation is generally expected to exhibit a reasonable to high estimation error margin.

In contrast, FBG sensors offer reliable and accurate temperature localized temperature readings in an arbitrary surface location, making FBGs a potentially very valuable tool for real-time monitoring of IGBT power modules. FBG sensors offer a superior alternative to V_{CE} -based evaluation for accurate and reliable junction temperature monitoring of IGBT

power modules. Their immunity to electromagnetic interference, robustness, small size, and long lifetime makes them suitable for industrial applications. Their integration with control systems can enable proactive maintenance, enhance system performance, and ensure the longevity of power conversion devices. They offer improved in-situ sensing compared to thermal camera application as well, as they are not limited by clear line of sight requirements and surface emissivity issues, and offer response rates much higher than those that can be attained using thermal cameras.

Chapter 8: Conclusion and Future Work

In this chapter the main outcomes from the research are summarised. Future work identified during the course of the research is also discussed along with potential future research avenues.

8.1 Conclusion

The thesis presents a study on the application of FBG sensors for accurate and real-time junction temperature measurement in IGBT power modules. The research addresses three main aspects: (1) investigating technologies for bonding FBG sensors to the IGBT chip surface inside the power module, (2) studying the impact of FBG head length on temperature sensing accuracy, and (3) assessing FBG sensors' performance compared to other methods for in-situ junction temperature measurement.

The research contributes significantly to the field of thermal sensing in power electronics devices, with several key findings:

An accurate FEA model of the IGBT power module is developed, providing an understanding of the thermal distribution and electro-thermal behavior within the module under different operating conditions. By simulating both transient and steady-state scenarios, the model aids in identifying feasible positions for the installation of FBG sensors. This FEA model is a valuable tool for future thermal behavior analysis and optimization studies in power electronics devices.

Innovative installation approaches for FBG sensors on the IGBT chip surface are studied to enable direct on-chip thermal sensing. The research explores the use of different interface materials, including thermal paste and glues with varying properties, to bond the FBG sensors securely and stably. By minimizing mechanical stress and ensuring reliable fixation, these approaches contribute to improved accuracy and reliability in temperature measurements. The findings of this research provide guidance on optimal sensor placement and interface material selection for enhanced thermal sensing performance.

The research evaluates the impact of thermal gradients and stress on FBG sensor-based temperature measurements. By conducting thermal simulations and experimental characterizations, the study identifies limitations associated with FBG sensors with longer head lengths under intense thermal gradients: FBG sensors with longer head lengths were found to be susceptible to distortion in the reflected spectrum under intense thermal gradients. These findings are crucial for selecting appropriate FBG sensor configurations and locations,

ensuring accurate and reliable temperature measurements in practical applications.

A comparative analysis of different temperature evaluation methods is conducted, focusing on voltage-based approaches (V_{CE} and ΔV_{CE}) and FBG sensor-based measurements. The FBG sensors are proven to be able to measure the temperature of the installation point accurately, validated by a thermal camera. In contrast, V_{CE} and ΔV_{CE} based temperature evaluation both require excessive requirements for voltage measurement accuracy, and both show relatively large errors in the thermal reading. The FBG sensors are validated as a reliable and accurate alternative for real-time temperature monitoring of IGBT power modules, offering significant advantages over V_{CE} -based approaches.

The FBG sensor based IGBT power module junction temperature measurement technology has two disadvantages: it increases the cost of the devices due to the inclusion of a fiber optic sensor for each IGBT chip and an interrogator for each practical application. Secondly, it requires the embedding of FBG sensors during the manufacturing process.

The findings pave the way for future advancements in thermal sensing technology, with opportunities to seamlessly integrate FBG sensor technology with control systems, and implement real-time thermal management strategies. The research provides valuable insights for researchers and practitioners, optimizing FBG sensor-based temperature measurement techniques of IGBT power modules across diverse industrial applications.

This thesis contributes to the broader field of power electronics and supports progress in thermal management strategies. Successful applications of FBG sensors in IGBT power modules underscore the potential for real-time temperature monitoring, which in turn enhances device reliability and efficiency.

8.2 Future work

There are several valuable avenues for future research that can significantly enhance the understanding and applicability of FBG sensors for junction temperature measurement in power modules, particularly in IGBTs. This section outlines the potential future work that holds immense value for the broader field of power electronics.

An important area of future investigation involves conducting vibration tests on different FBG sensor installation cases with various interface materials. Vibration testing is critical as power electronic devices, such as IGBT power modules, are often subjected to mechanical stresses and vibrations in real-world applications. The objective of this research would be to evaluate the performance and reliability of FBG sensors under dynamic conditions and assess

the impact of vibrations on temperature measurements. By subjecting the FBG sensor installation cases to controlled vibration environments, the response and stability of the FBG sensor can be analysed. The research should focus on quantifying any shifts or drifts in the FBG sensor's reflected spectrum due to vibrations, which may affect the accuracy of temperature measurements. This investigation is crucial for validating the suitability of FBG sensors for long-term on-chip thermal sensing in practical applications and ensuring the sensors' resilience to mechanical stress and vibrations.

Expanding the application of FBG sensors to measure the junction temperature of press-pack IGBTs and wide bandgap devices represents another valuable direction for future research. Press-pack IGBTs and wide bandgap devices, such as silicon carbide (SiC) and gallium nitride (GaN) devices, are gaining prominence in high-power and high-frequency applications due to their superior performance characteristics. Developing methodologies and experimental setups to measure the junction temperature of these devices using FBG sensors will provide valuable insights into their thermal behaviour under various operating conditions. The research should involve designing suitable FBG sensor configurations and installation techniques tailored to the specific characteristics and form factors of press-pack IGBTs and wide bandgap devices. Additionally, careful consideration should be given to the thermal conductivity and mechanical properties of materials used for interfacing FBG sensors to these devices.

One valuable research direction is the development of a multi-point FBG sensor array for spatial temperature mapping of power modules. Instead of using a single FBG sensor for temperature measurement, a network of FBG sensors can be strategically placed across the power module to capture temperature variations at multiple points. This approach will provide a more comprehensive view of the thermal distribution and hotspot identification within the module. The research should focus on optimizing the sensor array configuration, determining the optimal number of FBG sensors, and developing data acquisition and analysis techniques to process the spatial temperature data. Spatial temperature mapping can offer valuable insights into the thermal behaviour of power modules and aid in the design of more efficient cooling strategies.

Integrating FBG sensors with Artificial Intelligence (AI)-based thermal management systems is an innovative research direction. AI algorithms can process real-time temperature data from FBG sensors and dynamically adjust the cooling mechanisms to optimize thermal performance. The AI-based thermal management system can autonomously control cooling fans, heat sinks, or liquid cooling systems based on the temperature feedback from FBG

sensors. The research should involve developing AI algorithms tailored to the specific thermal characteristics of power modules and implementing a closed-loop control system that continuously adjusts the cooling parameters. This approach can result in highly efficient and adaptive thermal management solutions, ensuring optimal performance and reliability of power electronics devices.

Another promising research direction is to explore the use of FBG sensors for fault detection and prognostics in power modules. FBG sensors can detect temperature anomalies and fluctuations that may indicate potential faults or degradation in the IGBT or other power electronic components. The research should focus on developing fault detection algorithms based on the temperature data from FBG sensors. By monitoring temperature trends and deviations, the system can identify early signs of component degradation or impending failures. This proactive approach can lead to predictive maintenance strategies, preventing catastrophic failures and enhancing the reliability and lifespan of power modules.

References

- [1] S. Fankhauser, S. M. Smith, M. Allen, *et al.* "The meaning of net zero and how to get it right", *Nature Climate Change*, vol. 12, pp. 15-21, 2022.
- [2] Y. Liu, Y. Zhang, P. Wu and J. Li, "Development review and market research of IGBT devices for PV inverter and Wind power converter," 2020 17th *China International Forum on Solid State Lighting & 2020 International Forum on Wide Bandgap Semiconductors China (SSLChina: IFWS)*, Shenzhen, China, 2020, pp. 30-33.
- [3] A. Q. Huang, "Power Semiconductor Devices for Smart Grid and Renewable Energy Systems," in *Proceedings of the IEEE*, vol. 105, no. 11, pp. 2019-2047, Nov. 2017.
- [4] T. Ueta, M. Nagao and K. Hamada, "Application of Electrical Circuit Simulations in Hybrid Vehicle Development," in *IEEE Transactions on Electron Devices*, vol. 60, no. 2, pp. 544-550, Feb. 2013
- [5] H. Oh, B. Han, P. McCluskey, C. Han and B. D. Youn, "Physics-of-Failure, Condition Monitoring, and Prognostics of Insulated Gate Bipolar Transistor Modules: A Review," in *IEEE Transactions on Power Electronics*, vol. 30, no. 5, pp. 2413-2426, May 2015.
- [6] C. Qian et al., "Thermal Management on IGBT Power Electronic Devices and Modules," in *IEEE Access*, vol. 6, pp. 12868-12884, 2018.
- [7] H. Ye, M. H. Lin, and C. Basaran, "Failure modes and FEA analysis of power electronic packaging," *Finite Elements Anal. Des.*, vol. 38, pp. 601-612, May 2002.
- [8] M. H. M. Sathik, J. Pou, S. Prasanth, V. Muthu, R. Simanjorang and A. K. Gupta, "Comparison of IGBT junction temperature measurement and estimation methods-a review," *2017 Asian Conference on Energy, Power and Transportation Electrification (ACEPT)*, Singapore, 2017, pp. 1-8.
- [9] S. Yang, D. Xiang, A. Bryant, P. Mawby, L. Ran and P. Tavner, "Condition Monitoring for Device Reliability in Power Electronic Converters: A Review," in *IEEE Transactions on Power Electronics*, vol. 25, no. 11, pp. 2734-2752, Nov. 2010.
- [10] J. Chen, E. Deng, L. Xie, X. Ying and Y. Huang, "Investigations on Averaging Mechanisms of Virtual Junction Temperature Determined by $V_{CE}(T)$ Method for IGBTs," in *IEEE Transactions on Electron Devices*, vol. 67, no. 3, pp. 1106-1112, March 2020.
- [11] H. Cao, P. Ning, X. Chai, et al. "Online monitoring of IGBT junction temperature based on V_{CE} measurement," *Journal of Power Electron.* Vol. 21, pp. 451-463, Nov. 2021.
- [12] F. Forest, A. Rashed, J.-J. Huselstein, T. Martiré, and P. Enrici, "Fast power cycling protocols implemented in an automated test bench dedicated to IGBT module ageing," *Microelectronics Reliability*, vol. 55, pp. 81-92, Jan. 2015.
- [13] M. Ciappa and W. Fichtner, "Lifetime prediction of IGBT modules for traction applications," *2000 IEEE International Reliability Physics Symposium Proceedings*, San Jose, CA, USA, 2000, pp. 210-216.
- [14] P. Türkes and J. Sigg, "Electro-thermal simulation of power electronic systems," *Microelectron. J.*, vol. 29, no. 11, pp. 785-790, 1998.

- [15] R. Azar *et al.*, “Advanced electrothermal Spice modelling of large power IGBTs,” *IEE Proc.-Circuits, Devices Syst.*, vol. 151, no. 3, pp. 249-253, Jun. 2004.
- [16] G. Trigkidis, A. Bousbaine, and R. Thorn, “Thermal modelling of IGBT devices,” in *Proc. 41st Int. Univ. Power Eng. Conf. (PEC)*, vol. 2, Sep. 2006, pp. 584-588.
- [17] J. Moussodji, T. Kociniewski, and Z. Khatir, “Distributed electro-thermal model of IGBT chip—Application to top-metal ageing effects in short circuit conditions,” *Microelectron. Rel.*, vol. 53, pp. 1725-1729, Sep. 2013.
- [18] C. Hong, Y. Zhang, M. Zhang, et al, "Application of FBG sensors for geotechnical health monitoring, a review of sensor design, implementation methods and packaging techniques," *Sensors and Actuators A: Physical*, vol. 244, pp. 184-197, 2016.
- [19] J. P. Bazzo, T. Lukasiewicz, M. Vogt, et al., “Performance evaluation of an IGBT module by thermal analysis using Fibre Bragg Grating,” *Fourth European Workshop on Optical Fibre Sensors*, 2010.
- [20] J. J.-L. Zhang, H. You, J. He, X.-J. Xin, and F. Tian, “A fibre Bragg grating sensing system for monitoring IGBT temperature distribution and thermal conduction state of upper surface silicone,” *Proc. SPIE*, vol. 10846, p. 1084616, Dec. 2018.
- [21] A. Mohammed, *et al.* “Distributed Thermal Monitoring of Wind Turbine Power Electronic Modules Using FBG Sensing Technology”. *IEEE Sensors Journal*, vol. 20, no. 17, pp. 9886-9894, Sept 2020.
- [22] S. Chen, S. Ji, L. Pan, C. Liu and L. Zhu, "An ON-State Voltage Calculation Scheme of MMC Submodule IGBT," in *IEEE Transactions on Power Electronics*, vol. 34, no. 8, pp. 7996-8007, Aug. 2019.
- [23] J. Chen, E. Deng, Y. Zhang and Y. Huang, "Junction-to-Case Thermal Resistance Measurement and Analysis of Press-Pack IGBTs Under Double-Side Cooling Condition," in *IEEE Transactions on Power Electronics*, vol. 37, no. 7, pp. 8543-8553, July 2022
- [24] Chan-Su Yun, P. Malberti, M. Ciappa and W. Fichtner, "Thermal component model for electrothermal analysis of IGBT module systems," in *IEEE Transactions on Advanced Packaging*, vol. 24, no. 3, pp. 401-406, Aug. 2001.
- [25] B. Gao et al., "A Temperature Gradient-Based Potential Defects Identification Method for IGBT Module," in *IEEE Transactions on Power Electronics*, vol. 32, no. 3, pp. 2227-2242, March 2017.
- [26] X. Liu, E. Deng, H. Wang, C. Herrmann, T. Basler and J. Lutz, "Influence of Lateral Temperature Gradients on the Failure Modes at Power Cycling," in *IEEE Transactions on Components, Packaging and Manufacturing Technology*, vol. 11, no. 3, pp. 407-414, March 2021.
- [27] K. Zhang, C. Leduc and F. Iannuzzo, "Comparison of Junction Temperature Measurement Using the TSEP Method and Optical Fiber Method in IGBT Power Modules without Silicone Gel Removal," *PCIM Europe 2023; International Exhibition and Conference for Power Electronics, Intelligent Motion, Renewable Energy and Energy Management*, Nuremberg, Germany, 2023, pp. 1-8.
- [28] A. Rashed, F. Forest, J. J. Huselstein, T. Martiré and P. Enrici, "On-line [T_j , V_{ce}] monitoring of IGBTs stressed by fast power cycling tests," *2013 15th European Conference on Power Electronics and Applications (EPE)*, Lille, France, 2013, pp. 1-9.

- [29] Chan-Su Yun, P. Regli, J. Waldmeyer and W. Fichtner, "Static and dynamic thermal characteristics of IGBT power modules," 11th *International Symposium on Power Semiconductor Devices and ICs. ISPSD'99 Proceedings*, Toronto, ON, Canada, 1999, pp. 37-40.
- [30] A. D. Rajapakse, A. M. Gole and P. L. Wilson, "Electromagnetic transients simulation models for accurate representation of switching losses and thermal performance in power electronic systems," in *IEEE Transactions on Power Delivery*, vol. 20, no. 1, pp. 319-327, Jan. 2005.
- [31] S. Castagno, R. D. Curry and E. Loree, "Analysis and Comparison of a Fast Turn-On Series IGBT Stack and High-Voltage-Rated Commercial IGBTs," in *IEEE Transactions on Plasma Science*, vol. 34, no. 5, pp. 1692-1696, Oct. 2006
- [32] H. -J. Schulze, F. -J. Niedernostheide, F. Pfirsch and R. Baburske, "Limiting Factors of the Safe Operating Area for Power Devices," in *IEEE Transactions on Electron Devices*, vol. 60, no. 2, pp. 551-562, Feb. 2013.
- [33] C. Luedecke, G. Engelmann and R. W. De Doncker, "Optimized IGBT Turn-On Switching Performance using the Full Device Safe Operating Area," *PCIM Europe 2019; International Exhibition and Conference for Power Electronics, Intelligent Motion, Renewable Energy and Energy Management*, Nuremberg, Germany, 2019, pp. 1-8.
- [34] B. Wang, J. Cai, X. Du and L. Zhou, "Review of power semiconductor device reliability for power converters," in *CPSS Transactions on Power Electronics and Applications*, vol. 2, no. 2, pp. 101-117, 2017.
- [35] P. Ghimire, K. B. Pedersen, I. Trintis, and S. Munk-Nielsen, "Online chip temperature monitoring using 8 ce-load current and IR thermography," in *Proc. Energy Conversion Congress and Exposition (ECCE-2015)*, pp. 6602- 6609, Sep. 2015.
- [36] L. Dupont and Y. Avenas, "Evaluation of thermo-sensitive electrical parameters based on the forward voltage for on-line chip temperature measurements of IGBT devices," in *Energy Conversion Congress and Exposition (ECCE-2014)*, pp. 4028-4035, Sep. 2014.
- [37] Z. Xu, F. Wang and P. Ning, "Junction temperature measurement of IGBTs using short circuit current," *2012 IEEE Energy Conversion Congress and Exposition (ECCE)*, Raleigh, NC, USA, 2012, pp. 91-96
- [38] Z. Xu, F. Xu, and F. Wang, "Junction Temperature Measurement of IGBTs Using Short-Circuit Current as a Temperature-Sensitive Electrical Parameter for Converter Prototype Evaluation," *IEEE Transactions on Industrial Electronics*, vol. 62, pp. 3419-3429, Jun. 2015.
- [39] H. Luo, Y. Chen, P. Sun, W. Li, and X. He, "Junction Temperature Extraction Approach with Turn-off Delay Time for High-Voltage High-Power IGBT Modules," *IEEE Transactions on Power Electronics*, vol. 31, pp. 5122-5132, Jul. 2016.
- [40] C. H. van der Broeck, A. Gospodinov and R. W. De Doncker, "IGBT Junction Temperature Estimation via Gate Voltage Plateau Sensing," in *IEEE Transactions on Industry Applications*, vol. 54, no. 5, pp. 4752-4763, Sept.-Oct. 2018.
- [41] P. Sun et al., "Online junction temperature extraction with turn-off delay time for high power IGBTs," *2014 IEEE Energy Conversion Congress and Exposition*, Pittsburgh, PA, USA, 2014, pp. 4016-4021.

- [42] L. Li, P. Ning, X. Wen, Y. Li, Q. Ge, D. Zhang, et al., "A turn-off delay time measurement and junction temperature estimation method for IGBT," in *Applied Power Electronics Conference and Exposition (APEC-2017)*, pp. 2290-2296, Mar. 2017.
- [43] L. Dupont, Y. Avenas, and P.-O. Jeannin, "Comparison of junction temperature evaluations in a power IGBT module using an IR camera and three thermosensitive electrical parameters," *IEEE Transactions on Industry Applications*, vol. 49, pp. 1599-1608, Jul/Aug. 2013.
- [44] Z. Wang, W. Qiao, B. Tian, and L. Qu, "An effective heat propagation path-based online adaptive thermal model for IGBT modules," in *Proc. 29th Annu. IEEE Appl. Power Electron. Conf. Expo. (APEC)*, Mar. 2014, pp. 513-518.
- [45] M. Riccio *et al.*, "3D electro-thermal simulations of wide area power devices operating in avalanche condition," *Microelectron. Rel.*, vol. 52, pp. 2385-2390, Oct. 2012.
- [46] A. Dehbi, W. Wondrak, E. B. Rudnyi, U. Killat, and P. van Duijsen, "Efficient electrothermal simulation of power electronics for hybrid electric vehicle," in *Proc. Int. Conf. Thermal, Mech. Multi-Phys. Simulation Experim. Microelectron. Micro-Syst. (EuroSimE)*, 2008, pp. 1-7.
- [47] M. Riccio, M. Carli, L. Rossi, A. Irace, G. Breglio, and P. Spirito, "Compact electro-thermal modeling and simulation of large area multicellular trench-IGBT," in *Proc. 27th Int. Conf. Microelectron. (MIEL)*, May 2010, pp. 379-382.
- [48] J. Hunte, A. Mohammed and S. Djurović, "Response Time Characterisation of a Fibre Bragg Grating Humidity Sensor for Power Conversion Device Applications," 2020 9th *Mediterranean Conference on Embedded Computing (MECO)*, Budva, Montenegro, 2020, pp. 1-5.
- [49] Z. Wang, B. Tian, W. Qiao and L. Qu, "Real-Time Ageing Monitoring for IGBT Modules Using Case Temperature," in *IEEE Transactions on Industrial Electronics*, vol. 63, no. 2, pp. 1168-1178, Feb. 2016.
- [50] W. Brekel, T. Duetemeyer, G. Puk, and O. Schilling, "Time resolved in situ Tvj measurements of 6.5 kV IGBTs during inverter operation," in *Proceedings PCIM Europe*, pp. 808-813, 2009.
- [51] Z. Khatir, S. Carubelli, and F. Lecoq, "Real-time computation of thermal constraints in multichip power electronic devices," *IEEE Transactions on Components and Packaging Technologies*, vol. 27, pp. 337-344, Jun. 2004.
- [52] M. Fernández, X. Perpiñà, M. Vellvehi, O. Aviñó-Salvadó, S. Llorente and X. Jordà, "Power Losses and Current Distribution Studies by Infrared Thermal Imaging in Soft- and Hard-Switched IGBTs Under Resonant Load," in *IEEE Transactions on Power Electronics*, vol. 35, no. 5, pp. 5221-5237, May 2020.
- [53] D. Arora, J. Prakash, H. Singh, and A. Wason, "Reflectivity and Braggs wavelength in FBG," *International Journal of Engineering*, vol. 5, pp. 341-9, 2011.
- [54] H. Ren et al., "Quasi-Distributed Temperature Detection of Press-Pack IGBT Power Module Using FBG Sensing," in *IEEE Journal of Emerging and Selected Topics in Power Electronics*, vol. 10, no. 5, pp. 4981-4992, Oct. 2022.
- [55] T. Komiyama, Y. Chonan, J. Onuki, M. Koizumi, and T. Shigemura, "High-temperature thick Al wire bonding technology for high-power modules," *Japanese J. Appl. Phys. Part 1: Reg. Papers*, vol. 41,

pp. 5030-5033, Aug. 2002.

- [56] J. G. Bai, Z. Z. Zhang, J. N. Calata and G. -q. Lu, "Characterisation of Low-Temperature Sintered Nanoscale Silver Paste for Attaching Semiconductor Devices," *2005 Conference on High Density Microsystem Design and Packaging and Component Failure Analysis*, Shanghai, China, 2005, pp. 1-5.
- [57] Z. Liang, P. Ning, F. Wang and L. Marilino, "A Phase-Leg Power Module Packaged with Optimized Planar Interconnections and Integrated Double-Sided Cooling," in *IEEE Journal of Emerging and Selected Topics in Power Electronics*, vol. 2, no. 3, pp. 443-450, Sept. 2014
- [58] S. Eicher et al., "4.5kV press pack IGBT designed for ruggedness and reliability," *2004 IEEE Industry Applications Conference*, 2004. 39th IAS Annual Meeting, Seattle, WA, USA, 2004.
- [59] J. Feng, Y. Mei, X. Li and G. -Q. Lu, "Characterisations of a Proposed 3300-V Press-Pack IGBT Module Using Nanosilver Paste for High-Voltage Applications," in *IEEE Journal of Emerging and Selected Topics in Power Electronics*, vol. 6, no. 4, pp. 2245-2253, Dec. 2018.
- [60] E. Deng, Z. Zhao, P. Zhang, X. Luo, J. Li and Y. Huang, "Study on the Method to Measure Thermal Contact Resistance Within Press Pack IGBTs," in *IEEE Transactions on Power Electronics*, vol. 34, no. 2, pp. 1509-1517, Feb. 2019.
- [61] E. Deng, Z. Zhao, Q. Xin, J. Zhang, Y. Huang, "Analysis on the difference of the characteristic between high power IGBT modules and press pack IGBTs", *Microelectronics Reliability*, vol. 78, pp. 25-37, 2017.
- [62] M. Held, P. Jacob, G. Nicoletti, P. Scacco, and M. H. Pösch, "Fast power cycling test of IGBT modules in traction application," in *Proc. Int. Conf. Power Electron. Drive Syst.*, 1997, pp. 425-430.
- [63] J. Onuki, M. Koizumi, and M. Suwa, "Reliability of thick Al wire bonds in IGBT modules for traction motor drives," *IEEE Trans. Adv. Packag.*, vol. 23, no. 1, pp. 108-112, Feb. 2000.
- [64] M. Ciappa, "Selected failure mechanisms of modern power modules," *Microelectron. Rel.*, vol. 42, no. 4-5, pp. 653-667, 2002
- [65] P. Ratchev, B. Vandeveld, I. De Wolf, I. Center, and B. Leuven, "Reliability and failure analysis of Sn-Ag-Cu solder interconnections for PSGA packages on Ni/Au surface finish," *IEEE Trans. Device Mater. Rel.*, vol. 4, no. 1, pp. 5-10, Mar. 2004.
- [66] J. Lau, *Solder Joint Reliability: Theory and Applications*, 1st ed. Norwell, MA: Kluwer, 1991.
- [67] W. Koziarz and D. Gilmour, "Anomalous thermal conductivity in regions of non-uniform die attach integrity," in *Proc. IEEE Int. Rel. Phys. Symp.*, 1995, pp. 107-111.
- [68] D. Katsis and J. van Wyk, "Void-induced thermal impedance in power semiconductor modules: Some transient temperature effects," *IEEE Trans. Ind. Appl.*, vol. 39, no. 5, pp. 1239-1246, Oct. 2003.
- [69] Katsis and van Wyk, "A thermal, mechanical, and electrical study of voiding in the solder die-attach of power MOSFETs," *IEEE Trans. Compon. Packag. Technol.*, vol. 29, no. 1, pp. 127-136, Mar. 2006
- [70] M. Ciappa, "Reliability of high-power IGBT modules for traction applications," in *Proc. IEEE Int. Rel. Phys. Symp.*, 2007, pp. 480-485.
- [71] N. Baker, F. Iannuzzo, S. Munk-Nielsen, L. Dupont and Y. Avenas, "Experimental Evaluation of IGBT

Junction Temperature Measurement via a Modified- V_{CE} (ΔV_{CE_AVGE}) Method with Series Resistance Removal," *9th International Conference on Integrated Power Electronics Systems*, Nuremberg, Germany, 2016, pp. 1-6.

- [72] M. A. Eleffendi and C. M. Johnson, "Application of kalman filter to estimate junction temperature in IGBT power modules," *IEEE Transactions on Power Electronics*, vol. 31, pp. 1576-1587, Feb. 2016.
- [73] Y.-S. Kim and S.-K. Sul, "On-line estimation of IGBT junction temperature using on-state voltage drop," in *Proc. Industry Applications Conference, Thirty-Third IAS Annual Meeting*, pp. 853-859, Oct. 1988.
- [74] J. Moussodji, T. Kociniewski, and Z. Khatir, "Top-metal ageing effects on electro-thermal distributions in an IGBT chip under short circuit conditions," in *Proc. 15th Eur. Conf. IEEE Power Electron. Appl. (EPE)*, Sep. 2013, pp. 1-9.
- [75] S. Yin, T. Wang, K.-J. Tseng, J. Zhao, and X. Hu, "Electro-thermal modeling of SiC power devices for circuit simulation," in *Proc. 39th Annu. Conf. IEEE Ind. Electron. Soc. (IECON)*, Nov. 2013, pp. 718-723.
- [76] M. Alnajjar and D. Gerling, "Electrothermal model of IGBT threelevel neutral-point-clamped rectifier for synchronous reluctance generator in wind power application," in *Proc. Int. Conf. Renew. Energy Res. Appl. (ICRERA)*, 2015, pp. 167-172.
- [77] C. Batard, N. Ginot, and J. Antonios, "Lumped dynamic electrothermal model of IGBT module of inverters," *IEEE Trans. Compon., Packag., Manuf. Technol.*, vol. 5, no. 3, pp. 355-364, Mar. 2015.
- [78] F. D. Napoli *et al.*, "On-line junction temperature monitoring of switching devices with dynamic compact thermal models extracted with model order reduction," *Energies*, vol. 10, p. 189, Feb. 2017.
- [79] T. Kojima, Y. Yamada, M. Ciappa, M. Chiavarini, and W. Fichtner, "A novel electro-thermal simulation approach of power IGBT modules for automotive traction applications," in *Proc. 16th Int. Symp. Power Semiconductor Devices ICs (ISPSD)*, 2004, pp. 289-292.
- [80] T. Kojima *et al.*, "Novel electro-thermal coupling simulation technique for dynamic analysis of HV (hybrid vehicle) inverter," in *Proc. 37th IEEE Power Electron. Specialists Conf. (PESC)*, Jun. 2006, pp. 1-5.
- [81] T. Kojima, Y. Yamada, Y. Nishibe, and K. Torii, "Novel RC compact thermal model of HV inverter module for electro-thermal coupling simulation," in *Proc. IEEE Power Convers. Conf.-Nagoya (PCC)*, Apr. 2007, pp. 1025-1029.
- [82] Z. Luo, H. Ahn, and M. A. E. Nokali, "A thermal model for insulated gate bipolar transistor module," *IEEE Trans. Power Electron.*, vol. 19, no. 4, pp. 902-907, Jul. 2004.
- [83] A. Castellazzi, M. Ciappa, W. Fichtner, G. Lourdel, and M. Mermet-Guyennet, "Compact modelling and analysis of powersharing unbalances in IGBT-modules used in traction applications," *Microelectron. Rel.*, vol. 46, pp. 1754-1759, Nov. 2006.
- [84] A. Castellazzi, M. Ciappa, W. Fichtner, J. Urresti-Ibañez, and M. Mermet-Guyennet, "Integrated compact modelling of a planargate non-punch-through 3.3 kV-1200 A IGBT module for insightful analysis and realistic interpretation of the failure mechanisms," in *Proc ISPSD*, vol. 133, May 2007, pp. 133-136.

- [85] A. Castellazzi, M. Ciappa, W. Fichtner, E. Batista, J. Dienot, and M. Mermet-Guyennet, "Electro-thermal model of a high-voltage IGBT module for realistic simulation of power converters," in *Proc. ESSDERC*, 2007, pp. 155-158.
- [86] A. Castellazzi, M. Ciappa, W. Fichtner, G. Lourdelb, and M. Mermet-Guyennetb, "Comprehensive electro-thermal compact model," in *Proc. POWERENG*, Apr. 2007, pp. 405-410.
- [87] A. Castellazzi, E. Batista, M. Ciappa, J.-M. Dienot, M. Mermet-Guyennet, and W. Fichtner, "Full electro-thermal model of a 6.5 kV field-stop IGBT module," in *Proc. IEEE Power Electron. Specialists Conf. (PESC)*, Jun. 2008, pp. 392-397.
- [88] A. Ammous *et al.*, "Electrothermal modeling of IGBTs: Application to short-circuit conditions," *IEEE Trans. Power Electron.*, vol. 15, no. 4, pp. 778-790, Jul. 2000.
- [89] C.-S. Yun, P. Malberti, M. Ciappa, and W. Fichtner, "Thermal component model for electrothermal analysis of IGBT module systems," *IEEE Trans. Adv. Packag.*, vol. 24, no. 3, pp. 401-406, Aug. 2001.
- [90] S. Carubelli and Z. Khatir, "Experimental validation of a thermal modelling method dedicated to multichip power modules in operating conditions," *Microelectron. J.*, vol. 34, no. 12, pp. 1143-1151, Dec. 2003.
- [91] M. Ciappa, W. Fichtner, T. Kojima, Y. Yamada, and Y. Nishibe, "Extraction of accurate thermal compact models for fast electro-thermal simulation of IGBT modules in hybrid electric vehicles," *Microelectron. Rel.*, vol. 45, pp. 1694-1699, Sep. 2005.
- [92] A. Lakhsasi, Y. Hamri, and A. Skorek, "Partially coupled electro-thermal analysis for accurate prediction of switching devices," in *Proc. Can. Conf. Elect. Comput. Eng.*, vol. 1, May 2001, pp. 375-380.
- [93] U. Drofenik, D. Cottet, A. Müsing, J.-M. Meyer, and J. W. Kolar, "Modelling the thermal coupling between internal power semiconductor dies of a water-cooled 3300 V/1200 A HiPak IGBT module," in *Proc. Conf. Power Electron., Intell. Motion, Power Quality (PCIM)*, Nuremberg, Germany, May 2007, pp. 22-24.
- [94] V. d'Alessandro *et al.*, "Analysis of the UIS behaviour of power devices by means of SPICE-based electrothermal simulations," *Microelectron. Rel.*, vol. 53, pp. 1713-1718, Sep. 2013.
- [95] R. Wu, F. Iannuzzo, H. Wang, and F. Blaabjerg, "Fast and accurate Icepak-PSpice co-simulation of IGBTs under short-circuit with an advanced PSpice model," in *Proc. 7th IET Int. Conf. Power Electron., Mach. Drives (PEMD)*, 2014, pp. 1-5.
- [96] G. Greco, G. Vinci, G. Bazzano, A. Raciti, and D. Cristaldi, "Layered electro-thermal model of high-end integrated power electronics modules with IGBTs," in *Proc. 40th Annu. Conf. IEEE Ind. Electron. Soc. (IECON)*, Nov. 2014, pp. 1575-1580.
- [97] S.-Z. Xu, Y.-F. Peng, and S.-Y. Li, "Application thermal research of forced-air cooling system in high-power NPC three-level inverter based on power module block," *Case Stud. Thermal Eng.*, vol. 8, pp. 387-397, Sep. 2016.
- [98] J. Zarebski and K. Gorecki, "The electrothermal large-signal model of power MOS transistors for SPICE," *IEEE transactions on power electronics*, vol. 25, pp. 1265-1274, May 2010.

- [99] L. M. Hillkirk, "Dynamic surface temperature measurements in SiC epitaxial power diodes performed under single-pulse self-heating conditions," *Solidstate Electronics*, vol. 48, pp. 2181-2189, Dec. 2004.
- [100] W. Brekel, T. Duetemeyer, G. Puk, and O. Schilling, "Time resolved in situ Tvj measurements of 6.5 kV IGBTs during inverter operation," in *Proceedings PCIM Europe*, pp. 808-813, 2009.
- [101] A. D. Kersey, M. A. Davis, H. J. Patrick, M. LeBlanc, K. P. Koo, C. G. Askins, *et al.*, "Fibre grating sensors," *Journal of Lightwave Technology*, vol. 15, pp. 1442-1463, Aug 1997.
- [102] Y. J. Rao, "In-fibre Bragg grating sensors," *Measurement Science and Technology*, vol. 8, pp. 355-375, Apr 1997.
- [103] A. Othonos and K. Kalli, *Fibre Bragg gratings: fundamentals and applications in telecommunications and sensing*: Artech House, 1999.
- [104] A. Kersey, T. Berkoff, and W. Morey, "High-resolution fibre-grating based strain sensor with interferometric wavelength-shift detection," *Electronics Letters*, vol. 28, pp. 236-238, 1992.
- [105] A. Othonos, K. Kalli, D. Pureur, and A. Mugnier, "Fibre bragg gratings," in *Wavelength Filters in Fibre Optics*, ed: Springer, 2006, pp. 189-269.
- [106] C. Doyle, "Fibre Bragg Grating Sensors-An Introduction to Bragg gratings and interrogation techniques," *Smart Fibres Ltd*, pp. 1-5, 2003.
- [107] SmartFibres. (2018). *Our Technology*. Available: <https://www.smartfibres.com/technology>.
- [108] A. Mohammed and S. Djurović, "FBG Thermal Sensing Ring Scheme for Stator Winding Condition Monitoring in PMSMs," in *IEEE Transactions on Transportation Electrification*, vol. 5, no. 4, pp. 1370-1382, Dec. 2019.
- [109] A. Mohammed, J. I. Melecio and S. Djurović, "Open-Circuit Fault Detection in Stranded PMSM Windings Using Embedded FBG Thermal Sensors," in *IEEE Sensors Journal*, vol. 19, no. 9, pp. 3358-3367, 1 May1, 2019.
- [110] J. P. Bazzo, T. Lukaszewicz, M. Vogt, *et al.*, "Thermal characteristics analysis of an IGBT using a Fibre Bragg Grating," *Opt. Laser Eng.*, vol. 50, no. 2, pp. 99-103, 2012.
- [111] R. Zehringer, A. Stuck, T. Lang, "Material requirements for high voltage, high power IGBT devices," *Solid-State Electronics*, vol. 42, no. 12, pp. 2139-2151, 1998.
- [112] V. K. Khanna, "The Insulated Gate Bipolar Transistor IGBT Theory and Design", Canada, 2003, pp: 490-491.
- [113] H. Li, Y. Hu, S. Liu, Y. Li, X. Liao and Z. Liu, "An Improved Thermal Network Model of the IGBT Module for Wind Power Converters Considering the Effects of Base-Plate Solder Fatigue," in *IEEE Transactions on Device and Materials Reliability*, vol. 16, no. 4, pp. 570-575, Dec. 2016.
- [114] A. Volke, M. Hornkamp, "IGBT Modules Technologies, Driver and Application", Munich, Germany, 2011, pp: 173 - 176.
- [115] A. Zeanh *et al.*, "Thermomechanical Modelling and Reliability Study of an IGBT Module for an Aeronautical Application," *International Conference on Thermal, Mechanical and Multi-Physics Simulation and Experiments in Microelectronics and Micro-Systems*, Breisgau, 2008, pp. 1-7.

- [116] A. S. Bahman, K. Ma and F. Blaabjerg, "A Lumped Thermal Model Including Thermal Coupling and Thermal Boundary Conditions for High-Power IGBT Modules," in *IEEE Transactions on Power Electronics*, vol. 33, no. 3, pp. 2518-2530, March 2018.
- [117] R. Wu, H. Wang, K. Pedersen, *et al.*, "A Temperature-Dependent Thermal Model of IGBT Modules Suitable for Circuit-Level Simulations," *IEEE Transactions on Industry Applications*, vol. 52, no. 4, pp. 3306-3314, July-Aug. 2016.
- [118] Material Home. Online: http://www.efunda.com/materials/materials_home/materials.cfm (accessed on 18 January 2018)
- [119] N. An, M. Du, Z. Hu, K. Wei, "A High-Precision Adaptive Thermal Network Model for Monitoring of Temperature Variations in Insulated Gate Bipolar Transistor (IGBT) Modules", *Energies*, vol. 11, no. 3, Mar. 2018.
- [120] T. K. Gachovska, B. Tian, J. L. Hudgins, W. Qiao and J. F. Donlon, "A Real-Time Thermal Model for Monitoring of Power Semiconductor Devices," in *IEEE Transactions on Industry Applications*, vol. 51, no. 4, pp. 3361-3367, July-Aug. 2015.
- [121] B. Vermeersch and G. De Mey, "A Fixed-Angle Heat Spreading Model for Dynamic Thermal Characterization of Rear-Cooled Substrates," *Twenty-Third Annual IEEE Semiconductor Thermal Measurement and Management Symposium*, San Jose, CA, 2007, pp. 95-101.
- [122] Z. Wang and W. Qiao, "A Physics-Based Improved Cauer-Type Thermal Equivalent Circuit for IGBT Modules," in *IEEE Transactions on Power Electronics*, vol. 31, no. 10, pp. 6781-6786, Oct. 2016
- [123] L. Xie, X. Yuan and W. Wang, "Thermal Modeling of Fan-Cooled Plate–Fin Heatsink Considering Air Temperature Rise for Virtual Prototyping of Power Electronics," in *IEEE Transactions on Components, Packaging and Manufacturing Technology*, vol. 10, no. 11, pp. 1829-1839, Nov. 2020.
- [124] FIBERCORE. (2018). *Polyimide coated SM Fiber*. Available: https://www.newport.com/medias/sys_master/images/images/hf4/haa/8797241901086/Polyimide-Coated-SM-Fiber.pdf
- [125] ArGrating. (2018). *Optical fiber makes sense for future*. Available: <http://www.atgrating.com/en/>
- [126] <https://www.fluke.com/en-us/product/thermal-cameras/ti10>
- [127] Z. Liu, Y. Hu, X. Li, W. Song, S. Goyal, M. Micoulaut, M. Bauchy, "Glass relaxation and hysteresis of the glass transition by molecular dynamics simulations, ", *Phys. Rev. B*. 98, 104205, 2018.
- [128] B. Keita, D. Barker, and Y. Yang, "Determination of Glass Transition Temperature (T_g) of Adhesive-Based Optical Fiber Components by In-Situ Bragg Grating Strain Sensing." *ASME International Mechanical Engineering Congress and Exposition*. Vol. 36487. 2002.

Appendix A. MSP430 PWM Signal Program

In the main test rig shown by Fig. 4.8 in Chapter 4.3, two IGBT power modules were connected in parallel. T1 acted as the FBG instrumented chip under test while T2 was designated as the freewheeling circuit. The IGBTs were alternately turned on and off to decrease the voltage pulse caused by the circuit's inductive components when either IGBT was turned off. The IGBT control signal was generated by a Texas instruments MSP430 F5529 microcontroller. The program of the microcontroller for 100 Hz PWM is enclosed as following.

```
#include <msp430.h>

int main(void)
{
    WDTCTL = WDTPW | WDTHOLD;    // stop watchdog timer
    int i = 0;
    P1DIR |= BIT4;
    P1DIR |= BIT3;
    P1OUT &= ~BIT3;
    P1OUT &= ~BIT4;

    for(i=0;i<25000;i++);

    while(1)
    {

        P1OUT |= BIT4;
        P1OUT &= ~BIT3;
        for(i=0;i<1050;i++);

        P1OUT |= BIT3;
        P1OUT &= ~BIT4;
        for(i=0;i<750;i++);

    }

    return 0;
}
```